Axial, scalar, and tensor charges of the nucleon from 2+1+1-flavor Lattice QCD

Tanmoy Bhattacharya, Vincenzo Cirigliano, Saul D. Cohen, Rajan Gupta, Huey-Wen Lin, and Boram Yoon (Precision Neutron Decay Matrix Elements (PNDME) Collaboration)

Phys. Rev. D **94**, 054508 — Published 19 September 2016

DOI: 10.1103/PhysRevD.94.054508

LA-UR-16-20522
INT-PUB-16-008

Axial, Scalar and Tensor Charges of the Nucleon from 2+1+1-flavor Lattice QCD

Tanmoy Bhattacharya,[1,*] Vincenzo Cirigliano,[1,†] Saul D. Cohen,[2,‡]
Rajan Gupta,[1,§] Huey-Wen Lin,[3,¶] and Boram Yoon[1,**]

(Precision Neutron Decay Matrix Elements (PNDME) Collaboration)

[1] *Los Alamos National Laboratory, Theoretical Division T-2, Los Alamos, New Mexico 87545*
[2] *Institute for Nuclear Theory, University of Washington, Seattle, Washington 98195*
[3] *Physics Department, University of California, Berkeley, California 94720*

We present results for the isovector axial, scalar and tensor charges g_A^{u-d}, g_S^{u-d} and g_T^{u-d} of the nucleon needed to probe the Standard Model and novel physics. The axial charge is a fundamental parameter describing the weak interactions of nucleons. The scalar and tensor charges probe novel interactions at the TeV scale in neutron and nuclear β-decays, and the flavor-diagonal tensor charges g_T^u, g_T^d and g_T^s are needed to quantify the contribution of the quark electric dipole moment (EDM) to the neutron EDM. The lattice-QCD calculations were done using nine ensembles of gauge configurations generated by the MILC Collaboration using the HISQ action with 2+1+1 dynamical flavors. These ensembles span three lattice spacings $a \approx 0.06, 0.09$ and $0.12\,\text{fm}$ and light-quark masses corresponding to the pion masses $M_\pi \approx 135, 225$ and $315\,\text{MeV}$. High-statistics estimates on five ensembles using the all-mode-averaging method allow us to quantify all systematic uncertainties and perform a simultaneous extrapolation in the lattice spacing, lattice volume and light-quark masses for the connected contributions. Our final estimates, in the $\overline{\text{MS}}$ scheme at $2\,\text{GeV}$, of the isovector charges are $g_A^{u-d} = 1.195(33)(20)$, $g_S^{u-d} = 0.97(12)(6)$ and $g_T^{u-d} = 0.987(51)(20)$. The first error includes statistical and all systematic uncertainties except that due to the extrapolation Ansatz, which is given by the second error estimate. Combining our estimate for g_S^{u-d} with the difference of light quarks masses $(m_d - m_u)^{\text{QCD}} = 2.67(35)$ MeV given by the Flavor Lattice Average Group (FLAG), we obtain $(M_N - M_P)^{\text{QCD}} = 2.59(49)$ MeV. Estimates of the connected part of the flavor-diagonal tensor charges of the proton are $g_T^u = 0.792(42)$ and $g_T^d = -0.194(14)$. Combining our new estimates with precision low-energy experiments, we present updated constraints on novel scalar and tensor interactions, $\epsilon_{S,T}$, at the TeV scale.

PACS numbers: 11.15.Ha, 12.38.Gc
Keywords: nucleon charges, lattice QCD, excited-state contamination, neutron EDM

I. INTRODUCTION

The nucleon axial charge g_A^{u-d} is an important parameter that encapsulates the strength of weak interactions of nucleons. It enters in many analyses of nucleon structure and of the Standard Model (SM) and Beyond-the-SM (BSM) physics. For example, the rate of proton-proton fusion, which is the first step in the thermonuclear reaction chains that power low-mass hydrogen-burning stars like the Sun, is sensitive to it. It impacts the extraction of V_{ud} and tests of the unitarity of the CKM matrix, and the analysis of neutrinoless double-beta decay. At present, the ratio of the axial to the vector charge, g_A/g_V, is best determined from the experimental measurement of neutron beta decay using polarized ultracold neutrons by the UCNA Collaboration, 1.2756(30) [1], and by PERKEO II, 1.2761^{+14}_{-17} [2]. Note that, in the SM, $g_V = 1$ up to second order corrections in iso-spin breaking [3, 4] as a result of the conservation of the vector current. Using V_{ud} determined from superallowed nuclear beta decay or pion decay in combination with the average neutron lifetime measurement also gives a consistent value for g_A^{u-d} [5, 6]. Given the important role g_A^{u-d} plays in parametrizing the structure and weak interactions of nucleons, and probing signatures of new physics, it is important to calculate it directly with $O(1\%)$ accuracy using lattice QCD and eventually confront the theoretical prediction with experimental measurements.

The isovector scalar and tensor charges of the nucleon, combined with the helicity-flip parameters b and b_ν in the neutron decay distribution, probe novel scalar and tensor interactions at the TeV scale [7]. To optimally bound such scalar and tensor interactions using planned measurements of these b and b_ν parameters at the 10^{-3} precision level [8–10], requires the matrix elements of the local scalar and tensor quark bilinear operators within the nucleon state to be calculated with a precision of 10–15% [7]. Future higher-precision measurements of b and b_ν would require correspondingly higher-precision calculations of the matrix elements to place even more stringent bounds on TeV-scale couplings. In a recent work [11], we showed that lattice-QCD calculations have reached a level of control over all sources of systematic errors needed to yield the tensor charge with the required precision. The data for the scalar 3-point func-

* tanmoy@lanl.gov
† cirigliano@lanl.gov
‡ saul.cohen@gmail.com
§ rajan@lanl.gov
¶ hwlin@pa.msu.edu
** boram@lanl.gov

tions is about a factor of five more noisy. In this paper we show that by using the all-mode-averaging (AMA) error-reduction technique [12, 13] on the same set of ensembles used in Ref. [11], we can increase the statistics significantly and extract the scalar charge with $O(15\%)$ uncertainty. These higher-statistics results also improve upon our previous estimates of the tensor charges.

In addition to probing novel scalar and tensor interactions at the TeV scale, precise estimates of the matrix elements of the flavor-diagonal tensor operators are needed to quantify the contributions of the u, d, s, c quark electric dipole moments (EDM) to the neutron electric dipole moment (nEDM) [11, 14]. Most extensions of the Standard Model designed to explain nature at the TeV scale have new sources of CP violation, and the nEDM is a very sensitive probe of these. Thus, planned experiments aiming to reduce the current bound on the nEDM of 2.9×10^{-26} e cm [15] to around 10^{-28} e cm will put stringent constraints on many BSM theories, provided the matrix elements of novel CP-violating interactions, of which the quark EDM is one, are calculated with the required precision.

The tensor charges are also given by the zeroth moment of the transversity distributions that are measured in many experiments including Drell-Yan and Semi-Inclusive Deep Inelastic Scattering (SIDIS). Transversity distributions describe the net transverse polarization of quarks in a transversely polarized nucleon, and there exists an active program at Jefferson Lab (JLab) to measure them [16]. The extraction of the transversity distributions from the data taken over a limited range of Q^2 and Bjorken x is, however, not straightforward and requires additional phenomenological modeling. As discussed in Sec. VIII, lattice-QCD estimates of g_T^{u-d} are the most accurate at present. Future experiments will significantly improve the extraction of the transversity distributions. Thus, accurate calculations of the tensor charges using lattice QCD will continue to help elucidate the structure of the nucleon in terms of quarks and gluons and provide a benchmark against which phenomenological estimates utilizing measurements at JLab and other experimental facilities worldwide can be compared.

The methodology for calculating the isovector charges in an isospin symmetric theory, that is, measuring the contribution to the matrix elements of the insertion of the zero-momentum bilinear quark operators in one of the three valence quarks in the nucleon, is well developed [17–19]. Calculation of the flavor-diagonal charges is similar except that it gets additional contributions from contractions of the operator as a vacuum quark loop that interacts with the nucleon propagator through the exchange of gluons. Our estimates of disconnected contributions to $g_T^{u,d,s}$ were given in Ref. [11], where we showed that these contributions are small, $O(0.01)$, and in most cases consistent with zero within errors.[1] For the disconnected contribution of the strange quark, also needed for the neutron EDM analysis, we were able to extrapolate the data to the continuum limit and find $g_T^s = 0.008(9)$ [11, 20]. We do not have new results for these disconnected contributions. In this paper, we report on improvements in the estimate of the isovector charges g_A^{u-d}, g_S^{u-d} and g_T^{u-d} and in the connected parts of the flavor-diagonal charges $g_{A,S,T}^u$ and $g_{A,S,T}^d$, and the isoscalar combination g_T^{u+d} through a high-statistics study using the AMA method on five ensembles.

Overall, we analyze nine ensembles of $2+1+1$-flavors of highly improved staggered quarks (HISQ) [21] generated by the MILC Collaboration [22]. The high-statistics study using the AMA method [12, 13] allows us to demonstrate control over various sources of systematic errors and obtain reliable error estimates. Using these data, we perform a combined extrapolation to infinite volume, the continuum limit and the physical light-quark masses and obtain $g_A^{u-d} = 1.195(33)(20)$, $g_S^{u-d} = 0.97(12)(6)$ and $g_T^{u-d} = 0.987(51)(20)$. The first error includes statistical and all systematic uncertainties except that due to the extrapolation Ansatz, which is given by the second error estimate. Throughout the paper, we present results for the charges of the proton, which by convention are called nucleon charges in the literature. From these, results for the neutron are obtained by $u \leftrightarrow d$ interchange. A preliminary version of these results was presented in Ref. [23].

This paper is organized as follows. In Sec. II, we describe the parameters of the gauge ensembles analyzed and the lattice methodology. The fits used to isolate excited-state contamination are described in Sec. III. The renormalization of the operators is discussed in Sec. IV. Our final results for the isovector charges and the connected parts of the flavor-diagonal charges are presented in Sec. V. Results from additional simulations to validate our analysis of excited-state contamination are presented in Sec. VI, and the estimation of errors is revisited in Sec. VII. A comparison with previous works is given in Sec. VIII. In Sec. IX, we provide constraints on novel scalar and tensor interactions at the TeV scale using our new estimates of the charges and precision beta decay experiments and compare them to those from the LHC. Our final conclusions are presented in Sec. X.

II. LATTICE METHODOLOGY

The nine ensembles used in the analysis cover a range of lattice spacings ($0.06 \lesssim a \lesssim 0.12$ fm), pion masses ($135 \lesssim M_\pi \lesssim 320$ MeV) and lattice volumes ($3.3 \lesssim M_\pi L \lesssim 5.5$) and were generated using 2+1+1-flavors of highly improved staggered quarks (HISQ) [21]

[1] The five ensembles analyzed were $a12m310$, $a12m220$, $a09m310$, $a09m220$ and $a06m310$. Analysis of the physical mass ensemble $a09m130$ is ongoing.

Ensemble ID	a (fm)	$M_\pi^{\rm sea}$ (MeV)	$M_\pi^{\rm val}$ (MeV)	$L^3 \times T$	$M_\pi^{\rm val} L$	$t_{\rm sep}/a$	$N_{\rm conf}$	$N_{\rm meas}^{\rm HP}$	$N_{\rm meas}^{\rm AMA}$
a12m310 △	0.1207(11)	305.3(4)	310.2(2.8)	$24^3 \times 64$	4.55	{8, 9, 10, 11, 12} {8, 10, 12}	1013	8104	64832
a12m220S ◁	0.1202(12)	218.1(4)	225.0(2.3)	$24^3 \times 64$	3.29	{8, 10, 12}	1000	24000	
a12m220 ▷	0.1184(10)	216.9(2)	227.9(1.9)	$32^3 \times 64$	4.38	{8, 10, 12}	958	7664	
a12m220L ▽	0.1189(09)	217.0(2)	227.6(1.7)	$40^3 \times 64$	5.49	{10} {8, 10, 12, 14}	1010	8080	68680
a09m310 ✧	0.0888(08)	312.7(6)	313.0(2.8)	$32^3 \times 96$	4.51	{10, 12, 14}	881	7048	
a09m220 ☆	0.0872(07)	220.3(2)	225.9(1.8)	$48^3 \times 96$	4.79	{10, 12, 14}	890	7120	
a09m130 ✩	0.0871(06)	128.2(1)	138.1(1.0)	$64^3 \times 96$	3.90	{10, 12, 14}	883	7064	84768
a06m310 □	0.0582(04)	319.3(5)	319.6(2.2)	$48^3 \times 144$	4.52	{16, 20, 22, 24}	1000	8000	64000
a06m220 ◇	0.0578(04)	229.2(4)	235.2(1.7)	$64^3 \times 144$	4.41	{16, 20, 22, 24}	650	2600	41600

TABLE I. Parameters, including the Goldstone pion mass $M_\pi^{\rm sea}$, of the 2+1+1-flavor HISQ lattices generated by the MILC Collaboration and analyzed in this study are quoted from Ref. [22]. The lattice scale is determined using r_1 [22]. Symbols used in the plots are defined along with the ensemble ID. All fits are made versus $M_\pi^{\rm val}$ and finite-size effects are analyzed in terms of $M_\pi^{\rm val} L$. Estimates of $M_\pi^{\rm val}$, the clover-on-HISQ pion mass, are the same as given in Ref. [11] and the error is governed mainly by the uncertainty in the lattice scale. For each ensemble, we also give the values of the source-sink separation $t_{\rm sep}$ simulated, the number of configurations analyzed, and the number of measurements made using the HP and AMA methods. The HP calculation on the $a12m220L$ ensemble has been done with a single $t_{\rm sep} = 10$ while the LP analysis has been done with $t_{\rm sep} = \{8, 10, 12, 14\}$.

by the MILC Collaboration [22]. These are the same ensembles as used in Ref. [11], where we presented an analysis of the tensor charge. Their parameters are summarized in Table I.

The correlation functions needed to calculate the matrix elements are constructed using Wilson-clover fermions on these HISQ ensembles. This mixed-action, clover-on-HISQ approach, leads to a non-unitary formulation that at small, but *a priori* unknown, quark masses suffers from the problem of exceptional configurations. In Ref. [11], we described the tests performed to show the absence of any such exceptional configurations in our statistical samples. The mixed-action approach also introduces additional corrections to the leading chiral and continuum extrapolation Ansatz. In Sec. V, we analyze the observed dependence of the charges on M_π over the range $135 \lesssim M_\pi \lesssim 320$ MeV with and without the chiral logarithm corrections in the fit Ansatz. It turns out that with our current data, the observed dependence on the lattice spacing a and the quark masses is accounted for by the lowest-order correction terms.

The parameters used in the analysis of 2- and 3-point functions with clover fermions are given in Table II. The Sheikholeslami-Wohlert coefficient [24] used in the clover action is fixed to its tree-level value with tadpole improvement, $c_{\rm sw} = 1/u_0^3$, where u_0 is the fourth root of the plaquette expectation value calculated on the hypercubic (HYP) smeared [25] HISQ lattices.

The masses of light clover quarks were tuned so that the clover-on-HISQ pion masses, $M_\pi^{\rm val}$, match the HISQ-on-HISQ Goldstone ones, $M_\pi^{\rm sea}$. Both estimates are given in Table I. All fits in M_π^2 to study the chiral behavior are made using the clover-on-HISQ $M_\pi^{\rm val}$ since the correlation functions, and thus the chiral behavior of the charges, have a greater sensitivity to it. Henceforth, for brevity, we drop the superscript and denote the clover-on-HISQ pion mass as M_π. Performing fits using the HISQ-on-HISQ values, $M_\pi^{\rm sea}$, did not change the estimates significantly.

Most of the details of the methodology, the calculation strategy and the analysis are the same as described in Ref. [11]. The new feature in the current work is the use of the AMA method [12, 13] to recalculate all quantities on the five ensembles that had the largest uncertainty: $a12m310$, $a12m220L$, $a09m130$, $a06m310$ and $a06m220$. These new estimates have significantly smaller statistical errors, and this improvement allows us to better understand and quantify the excited-state contamination. Using these more precise estimates improves our final combined extrapolation in the lattice volume, $M_\pi L \to \infty$, lattice spacing, $a \to 0$, and the light-quark mass, $M_{\pi^0} \to 135$ MeV.

A. Correlation Functions

The interpolating operator χ used to create/annihilate the nucleon state is

$$\chi(x) = \epsilon^{abc} \left[q_1^{aT}(x) C \gamma_5 \frac{(1 \pm \gamma_4)}{2} q_2^b(x) \right] q_1^c(x) \qquad (1)$$

with color indices $\{a, b, c\}$, charge conjugation matrix $C = \gamma_0\gamma_2$, and q_1 and q_2 denote the two different flavors of light quarks. At zero momentum, this operator couples only to the spin-$\frac{1}{2}$ state. The non-relativistic projection $(1 \pm \gamma_4)/2$ is inserted to improve the signal, with the plus and minus sign applied to the forward and backward propagation in Euclidean time, respectively [27].

The 2-point and 3-point nucleon correlation functions

at zero momentum are defined as

$$\mathbf{C}^{\rm 2pt}_{\alpha\beta}(t) = \sum_{\mathbf{x}} \langle 0|\chi_\alpha(t,\mathbf{x})\overline{\chi}_\beta(0,\mathbf{0})|0\rangle\,, \tag{2}$$

$$\mathbf{C}^{\rm 3pt}_{\Gamma;\alpha\beta}(t,\tau) = \sum_{\mathbf{x},\mathbf{x}'} \langle 0|\chi_\alpha(t,\mathbf{x})\mathcal{O}_\Gamma(\tau,\mathbf{x}')\overline{\chi}_\beta(0,\mathbf{0})|0\rangle\,, \tag{3}$$

where α and β are spinor indices. The source is placed at timeslice 0, t is the sink timeslice, and τ is an intermediate timeslice at which the local quark bilinear operator $\mathcal{O}^q_\Gamma(x) = \bar{q}(x)\Gamma q(x)$ is inserted. The Dirac matrix Γ is 1, γ_4, $\gamma_i\gamma_5$ and $\gamma_i\gamma_j$ for scalar (S), vector (V), axial (A) and tensor (T) operators, respectively. In this work, subscripts i and j on gamma matrices run over $\{1,2,3\}$, with $i<j$.

The nucleon charges g^q_Γ are obtained from the matrix element

$$\langle N(p,s)|\mathcal{O}^q_\Gamma|N(p,s)\rangle = g^q_\Gamma \bar{u}_s(p)\Gamma u_s(p) \tag{4}$$

with spinors satisfying

$$\sum_s u_s(\mathbf{p})\bar{u}_s(\mathbf{p}) = \not{p} + m_N\,. \tag{5}$$

To extract the charges, we first construct the projected 2- and 3-point correlation functions

$$C^{\rm 2pt}(t) = \langle {\rm Tr}[\mathcal{P}_{\rm 2pt}\mathbf{C}^{\rm 2pt}(t)]\rangle \tag{6}$$

$$C^{\rm 3pt}_\Gamma(t,\tau) = \langle {\rm Tr}[\mathcal{P}_{\rm 3pt}\mathbf{C}^{\rm 3pt}_\Gamma(t,\tau)]\rangle\,. \tag{7}$$

The operator $\mathcal{P}_{\rm 2pt} = (1+\gamma_4)/2$ is used to project on to the positive parity contribution for the nucleon propagating in the forward direction. For the connected 3-point contributions, $\mathcal{P}_{\rm 3pt} = \mathcal{P}_{\rm 2pt}(1+i\gamma_5\gamma_3)$ is used. Note that the $C^{\rm 3pt}_\Gamma(t,\tau)$ defined in Eq. (7) becomes zero if Γ anticommutes with γ_4, so only $\Gamma = 1$, γ_4, $\gamma_i\gamma_5$ and $\gamma_i\gamma_j$ elements of the Clifford algebra survive. The fits used to extract the charges from the 2- and 3-point functions defined in Eqs. (6) and (7) are discussed in Sec. III.

ID	m_l	$c_{\rm SW}$	Smearing Parameters
a12m310	−0.0695	1.05094	{5.5, 70}
a12m220S	−0.075	1.05091	{5.5, 70}
a12m220	−0.075	1.05091	{5.5, 70}
a12m220L	−0.075	1.05091	{5.5, 70}
a09m310	−0.05138	1.04243	{5.5, 70}
a09m220	−0.0554	1.04239	{5.5, 70}
a09m130	−0.058	1.04239	{5.5, 70}
a06m310	−0.0398	1.03493	{6.5, 70}
a06m220	−0.04222	1.03493	{5.5, 70}

TABLE II. The parameters used in the calculation of clover propagators. The hopping parameter κ in the clover action is given by $2\kappa_l = 1/(m_l+4)$. The Gaussian smearing parameters are defined by $\{\sigma, N_{\rm GS}\}$, both in Chroma convention [26]. The parameter $N_{\rm GS}$ is the number of applications of the Laplacian operator and the width of the smearing is controlled by σ. m_l is tuned to achieve $M_\pi^{\rm val} \approx M_\pi^{\rm sea}$.

B. The AMA Method

The high-statistics calculation using the all-mode-averaging (AMA) technique [12, 13] was carried out on five ensembles. To implement the AMA method, we choose four different source timeslices separated by $T/4$ on each configuration. Starting from each of these timeslices we calculate the 2- and 3-point correlators by choosing $N_{\rm LP} = 16$ source locations from which low-precision (LP) evaluation of the quark propagator is carried out. The resulting LP estimates for 2- and 3-point functions from these $4\times 16 = 64$ sources may be biased due to incomplete inversion of the Dirac matrix. To remove this bias, we place an additional high-precision (HP) source on each of the four timeslices from which we calculate both LP and HP correlation functions. Thus, in our implementation of the AMA method, $64+4$ LP and 4 HP calculations are done on each configuration. These 4 HP calculations are the same as used in the full HP study presented in Ref. [11] and, therefore, needed no additional calculations. In total, the new simulations generated $4\times 16 + 4 = 68$ LP 2- and 3-point correlation functions per configuration.

Using four HP and $64+4$ LP correlators on each configuration, the bias corrected 2- and 3- point functions are given by

$$C^{\rm imp} = \frac{1}{N_{\rm LP}}\sum_{i=1}^{N_{\rm LP}} C_{\rm LP}(\mathbf{x}^{\rm LP}_i) + \frac{1}{N_{\rm HP}}\sum_{i=1}^{N_{\rm HP}}\left[C_{\rm HP}(\mathbf{x}^{\rm HP}_i) - C_{\rm LP}(\mathbf{x}^{\rm HP}_i)\right]\,, \tag{8}$$

where $C_{\rm LP}$ and $C_{\rm HP}$ are the 2- and 3-point correlation functions calculated in LP and HP, respectively, and $\mathbf{x}^{\rm LP}_i$ and $\mathbf{x}^{\rm HP}_i$ are the two kinds of source positions.

The basic idea of AMA is that, in the low-precision evaluation, the LP average, first term in Eq. (8), may be biased. The bias is corrected by the second low-statistics term without significantly increasing the overall statistical errors. To determine the LP stopping criteria, we compared LP and AMA results using 50 configurations from the $a12m310$ ensemble with $r_{\rm LP} \equiv |{\rm residue}|_{\rm LP}/|{\rm source}| = 10^{-2}, 5\times10^{-3}, 10^{-3}$ and 10^{-4}. All four LP estimates agreed with the AMA estimate within 1σ. To reduce computational cost and yet be conservative, we selected $r_{\rm LP} = 10^{-3}$ for all calculations presented in this work.

In our current implementation, 17 LP measurements cost the same as one HP when using the multigrid algorithm for inverting the Dirac matrix [28]. Adding 64+4 LP measurements doubled the cost compared to 4 HP measurements, whereas the increase in statistics is by a factor of 16 in the AMA analysis with bias correction. Note that only four of the existing eight HP source positions were used for bias correction as these were found to be sufficient. Also, on the $a06m220$ ensemble, only four HP measurements were made on each configuration.

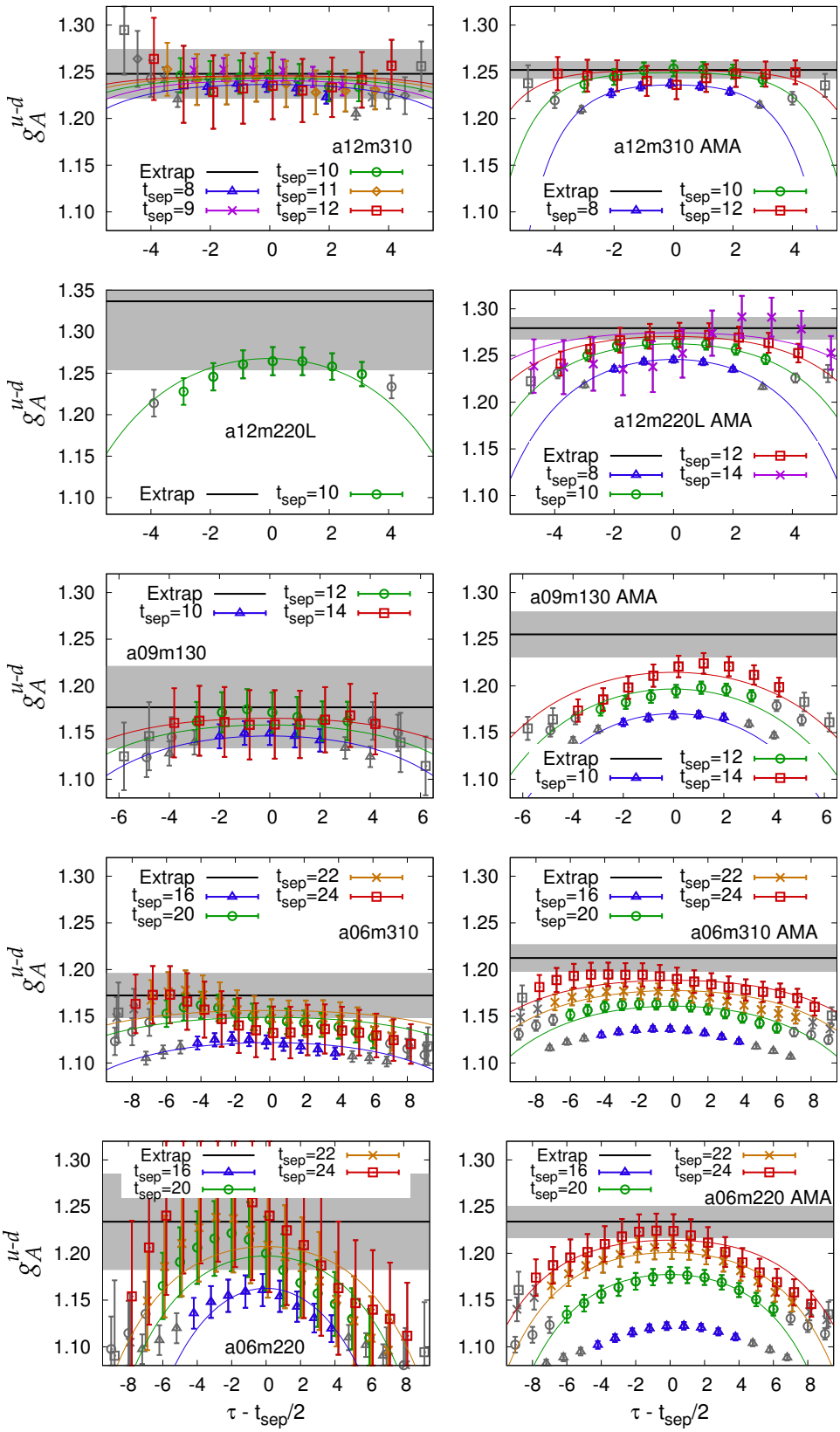

FIG. 1. Comparison of the unrenormalized g_A^{u-d} data obtained using all HP measurements (left) with the AMA method (right). The parameters for these five ensembles are given in Table I. The increase in statistics with the AMA method significantly improves the resolution of the data at the various source-sink separations, $t_{\rm sep}$. In each case, the solid line within the grey error band is the $t_{\rm sep} \to \infty$ result given by the 2-state fit using Eqs. (9) and (10) and the colored lines are its value for different $t_{\rm sep}$ plotted in the same color as the data. On the $a12m220L$ ensemble, the HP data was generated only with $t_{\rm sep} = 10$.

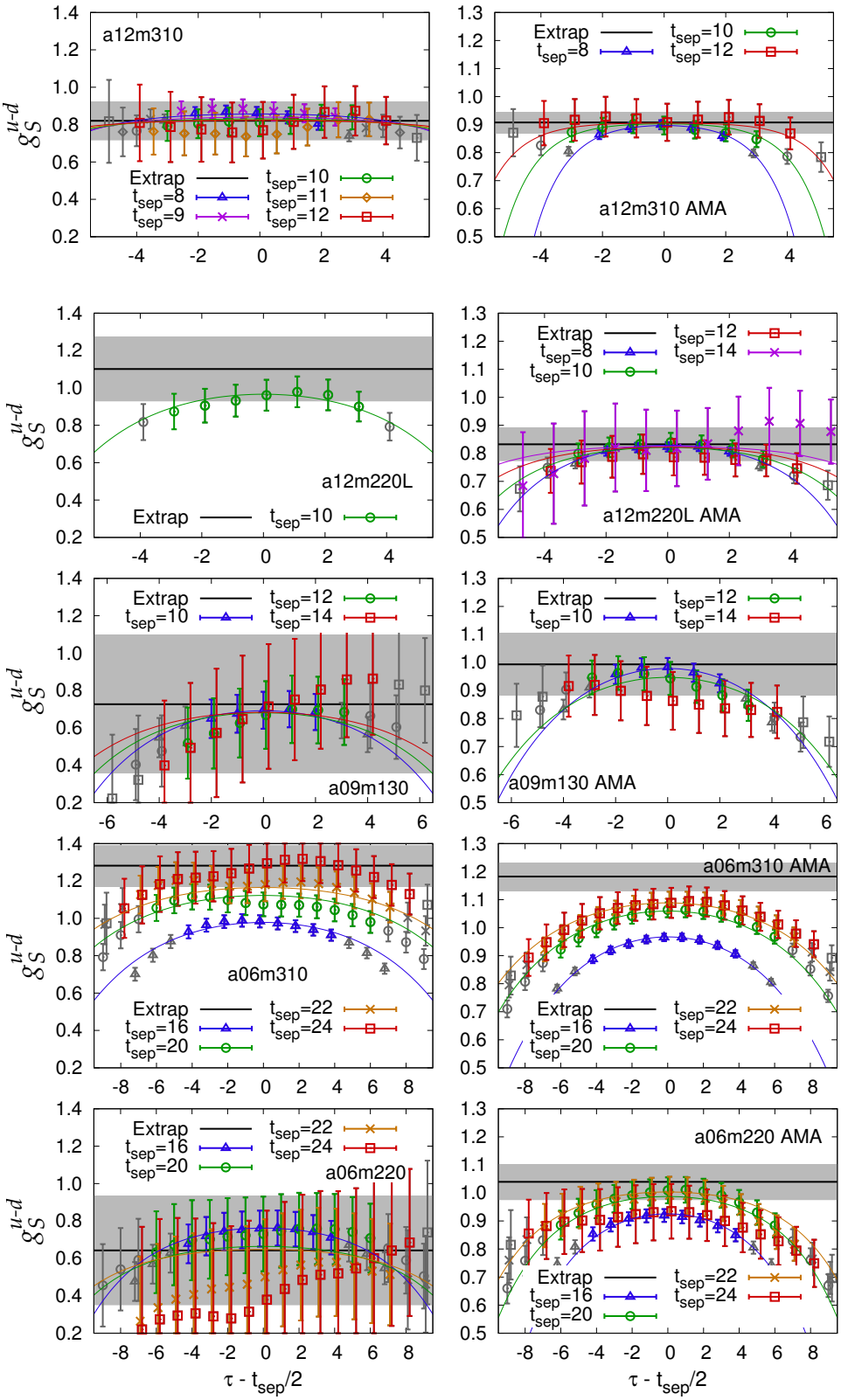

FIG. 2. Comparison of the unrenormalized g_S^{u-d} data obtained using all HP measurements (left) with the AMA method (right). The rest is the same as in Fig. 1.

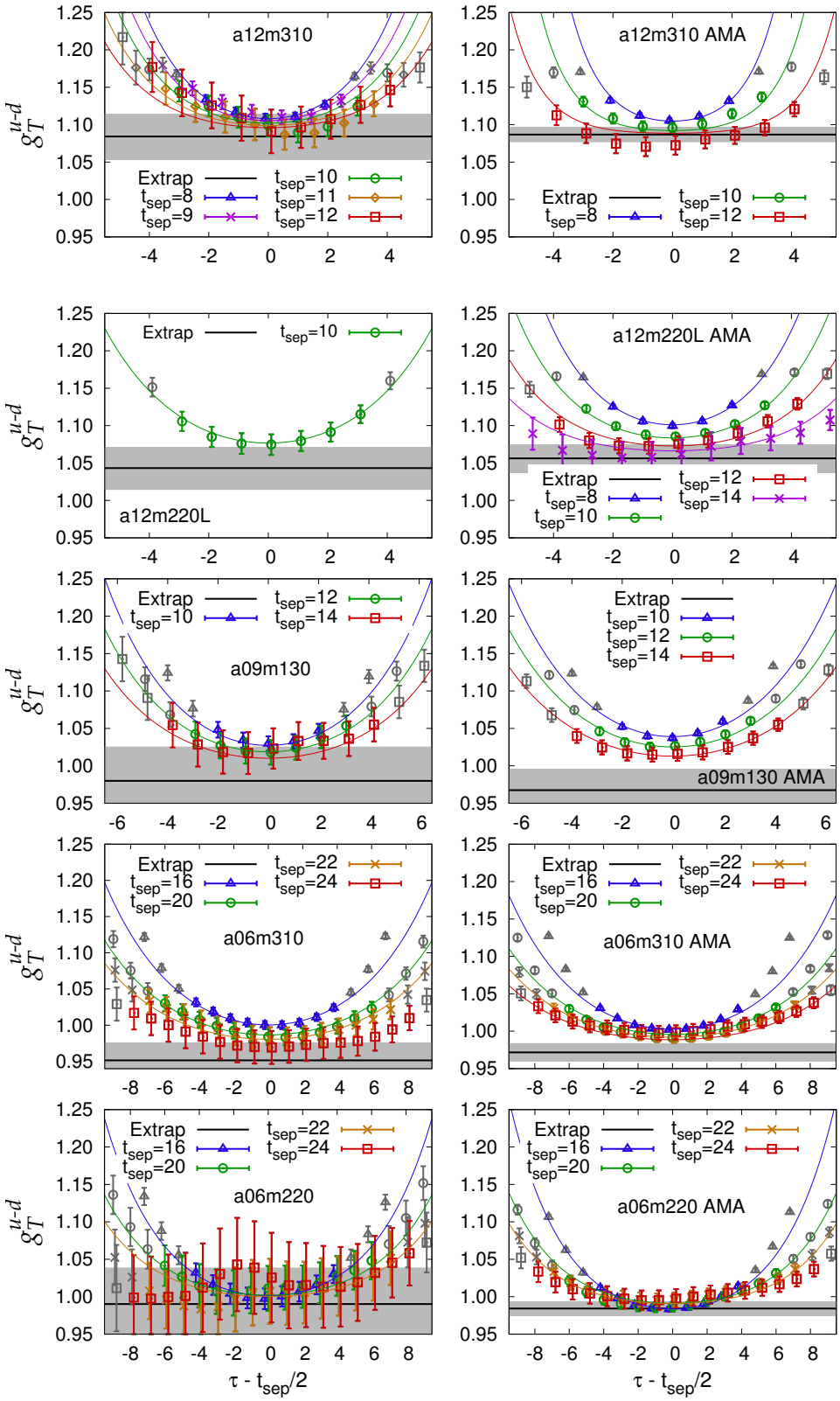

FIG. 3. Comparison of the unrenormalized g_T^{u-d} data obtained using all HP measurements (left) with the AMA method (right). The rest is the same as in Fig. 1.

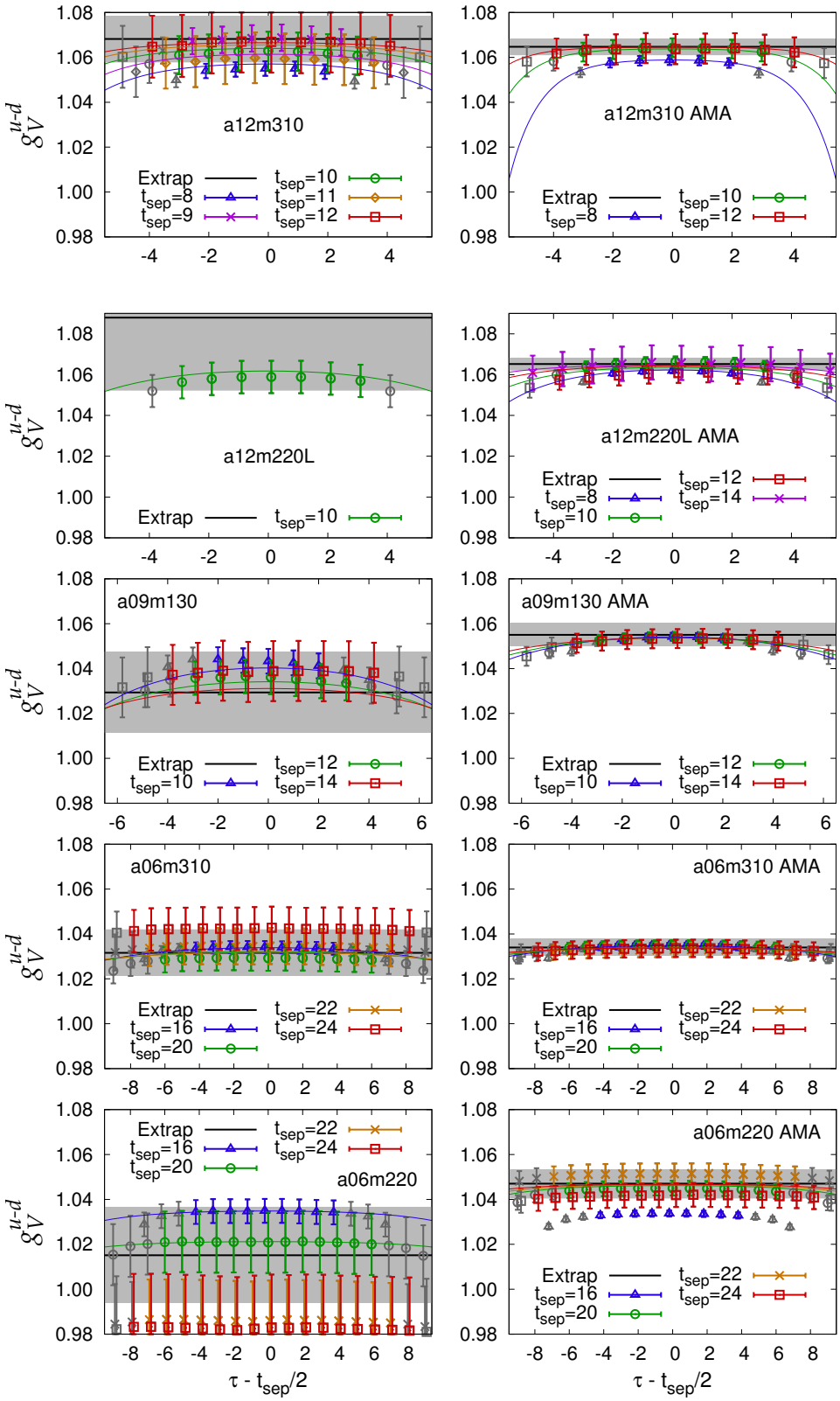

FIG. 4. Comparison of the unrenormalized g_V^{u-d} data obtained using all HP measurements (left) with the AMA method (right). The rest is the same as in Fig. 1.

To test how the errors change with the bias correction, we compare the results for the charges on the five ensembles analyzed using both HP and AMA methods. We compared both HP versus AMA and AMA versus LP estimates. A comparison of the HP versus the AMA data for the masses and amplitudes extracted from the nucleon 2-point function is shown in Tables III and IV. Comparison of the isovector charges g_A^{u-d}, g_S^{u-d}, g_T^{u-d} and g_V^{u-d} is shown in Figs. 1, 2, 3 and 4, respectively. The increase in statistics with the AMA method (see Table I) significantly improves the precision of the data at the various source-sink separations, $t_{\rm sep}$, we have used in the analysis of the 3-point functions. In each panel of the four figures, the grey error band and the solid line within it gives the $t_{\rm sep} \to \infty$ value obtained from the 2-state fit using Eqs. (9) and (10). The two estimates are, in most cases, consistent and in the rest the difference is less than 2σ. The AMA data at each $t_{\rm sep}$ has much smaller errors, consequently, the $t_{\rm sep} \to \infty$ estimates from the 2-state fit to the AMA data are more precise.

Comparing the AMA with the LP data, we find that in each case the difference is a tiny fraction of the statistical error in the AMA calculation; that is, the bias correction term is negligible. This is shown in Tables III and IV for the 2-point data and in Tables VI, VII and VIII for the matrix elements extracted from the 3-point data. Thus, our conclusion is that using the multigrid solver [28, 29] with a low-accuracy stopping criterion $r_{\rm LP} \equiv |\text{residue}|_{\rm LP}/|\text{source}| \approx 10^{-3}$, is as good as the HP inversion with $r_{\rm HP} = 10^{-8}$–10^{-12} for the calculation of the nucleon charges at the level of statistical precision achieved in this work.

Our final errors are obtained using a single elimination Jackknife analysis over the configurations; that is, we first construct the average defined in Eq. (8) on each configuration. Because of this "binning" of the data, we do not need to correct the Jackknife estimate of the error for correlations between the 64 LP measurements per configuration. It is, however, useful to determine the number of source positions one can place on each configuration beyond which the additional computational cost offsets the gain in statistics. The following tests indicate that the correlations between estimates from various sources are reasonably small with up to $O(100)$ sources per configuration on lattices with $M_\pi L \gtrsim 4$ and $M_\pi T \gtrsim 8$.

- Comparing the errors in the estimates for masses and amplitudes given in Tables III and IV, we find that the AMA errors are a factor of 2–4 smaller than those in the all HP analysis. (In the limit of no correlations, the scaling factor should be $\sqrt{64/8} = 2.83$.) A similar improvement is seen in the matrix elements as shown in Tables VI, VII and VIII. In most cases, the improvement is observed to become better with decreasing quark mass and lattice spacing.

- Figure 5 illustrates that the errors decrease by a factor of about 3.7 when the number of LP sources are increased from 4 to 64 on the $a06m220$ lattices. The gain is similar in both the 2- and 3-point functions.

- On the *a06m310* ensemble, we compared estimates of the 2- and 3-point correlation functions using 64 and 128 LP sources during the study of the disconnected diagram contribution reported in Ref. [11]. We found that the errors are reduced by only a factor of 1.2. A similar comparison of 2- and 3-point functions obtained using 64 and 128 LP sources in the $a06m310$ AMA2 study discussed in Sec. VI shows that errors reduce by only a factor of 1.15. Thus, both tests indicate that the gain in statistics becomes small when more the 64 LP sources per configuration are used on lattices with $M_\pi L \sim 4$.

A second technique used to reduce correlations in the AMA calculations is to choose the 64 LP source points randomly within and between configurations. On each configuration, the four source timeslices are chosen randomly to be $r + \alpha T/4$ with r a random integer $\in \{1, T/4\}$ and $\alpha \in \{0, 1, 2, 3\}$. On the $a06m220$ ensemble, each of these four timeslices is then divided into 16 boxes of size $L/2 \times L/2 \times L/4$ and a random source point is chosen within each of these boxes. On the rest of the ensembles, the 16 source points on each of the 4 timeslices are chosen randomly. In the HP calculation, the 8 source points were taken to be the same on all the configurations. A statistical analysis comparing the HP and AMA data shows that choosing the source points randomly reduces the final errors. For example, the standard error in the mean constructed by choosing a single source point per configuration is smaller for the LP data with randomly selected source point versus the HP data in which the source point was fixed to be the same on all the configurations.

To reduce computational cost, we have used the coherent sequential source method [30]. Four sequential sources on the four sink timeslices were calculated and held in computer memory. These were added and a single inversion performed to construct the coherent sequential propagator. Details of the method are given in Ref. [31], where we also showed that this method does not increase the bias or the errors.

To estimate errors, we performed both correlated and uncorrelated fits to the nucleon 2- and 3-point functions data. The final statistical errors were calculated using a single elimination jackknife method with uncorrelated fits to both the 2- and 3-point functions since correlated fits were not stable for the 3-point functions in all cases. In all cases in which the correlated fits to the 3-point functions were stable under changes in the fit ranges and had $\chi^2 \leq 1$, the correlated and uncorrelated fits gave overlapping estimates.

Having high-statistics data with the AMA method significantly improves the analysis. For example, the plateaus in the effective-mass plots extend to larger Euclidian time as discussed in Sec. III. This allowed fits to

ID	Type	Fit Range	aM_0	aM_1	$\mathcal{A}_0^2 \times 10^{11}$	$\mathcal{A}_1^2 \times 10^{11}$	$\mathcal{A}_1^2/\mathcal{A}_0^2$
a12m310	HP	2–15	0.6669(53)	1.36(11)	6.57(27)	6.28(61)	0.96(7)
a12m310	AMA	3–15	0.6722(22)	1.64(16)	6.95(12)	9.5(3.4)	1.36(47)
a12m220S	HP	2–15	0.6233(55)	1.42(13)	6.58(26)	6.94(93)	1.05(11)
a12m220	HP	2–15	0.6232(49)	1.45(15)	6.58(24)	6.8(1.1)	1.03(14)
a12m220L	HP	2–15	0.6046(71)	1.16(12)	5.68(37)	5.63(51)	0.99(6)
a12m220L	LP	3–15	0.6118(26)	1.18(7)	5.99(15)	4.64(50)	0.78(7)
a09m310	HP	4–20	0.4943(62)	0.87(9)	13.6(1.1)	14.4(1.7)	1.05(8)
a09m220	HP	4–20	0.4535(58)	0.86(8)	11.8(9)	15.2(2.1)	1.29(11)
a09m130	HP	3–20	0.4186(76)	0.83(6)	9.74(89)	17.2(1.0)	1.76(10)
a09m130	AMA	5–20	0.4150(45)	0.73(5)	8.70(59)	11.7(8)	1.34(6)
a06m310	HP	5–30	0.3219(37)	0.58(2)	0.53(4)	1.26(6)	2.35(12)
a06m310	AMA	7–30	0.3277(18)	0.59(2)	0.59(2)	1.10(8)	1.86(8)
a06m220	HP	5–30	0.3166(66)	0.64(5)	13.0(1.5)	38.5(5.4)	2.96(20)
a06m220	AMA	7–30	0.3068(17)	0.63(2)	11.3(3)	38.5(3.0)	3.41(18)

TABLE III. Estimates of the masses M_0 and M_1 and the amplitudes $\mathcal{A}_0$ and $\mathcal{A}_1$ extracted from the fits to the 2-point correlation functions using the 2-state Ansatz given in Eqs. (9) and (10). We give the results of fits to both the HP and the AMA data for the five ensembles $a12m310$, $a12m220L$, $a09m130$, $a06m310$ and $a06m220$. The Gaussian smearing parameters, $\{\sigma, N_{\rm GS}\}$, used in the calculation of the 2- and 3-point connected correlation functions are given in Table II. The fit range used is listed as case 1 in Table V.

ID	Type	Fit Range	aM_0	aM_1	$\mathcal{A}_0^2 \times 10^{11}$	$\mathcal{A}_1^2 \times 10^{11}$	$\mathcal{A}_1^2/\mathcal{A}_0^2$
a12m310	HP	3–15	0.6641(76)	1.20(17)	6.38(46)	4.5(9)	0.70(11)
a12m310	AMA	3–15	0.6722(22)	1.64(16)	6.95(12)	9.5(3.4)	1.36(47)
a12m220S	HP	3–15	0.6202(94)	1.20(27)	6.37(54)	4.3(1.5)	0.67(18)
a12m220	HP	3–15	0.6216(73)	1.27(30)	6.47(42)	4.5(2.2)	0.69(30)
a12m220L	HP	3–15	0.597(14)	0.96(17)	5.16(87)	4.19(33)	0.81(14)
a12m220L	LP	4–15	0.6109(35)	1.11(13)	5.92(22)	3.78(98)	0.64(15)
a09m310	HP	5–20	0.4933(78)	0.84(12)	13.4(1.5)	13.0(2.9)	0.97(15)
a09m220	HP	5–20	0.4529(68)	0.84(12)	11.7(1.1)	14.1(3.8)	1.21(24)
a09m130	HP	4–20	0.413(12)	0.75(10)	8.9(1.6)	14.0(1.4)	1.56(18)
a09m130	AMA	6–20	0.4137(60)	0.71(7)	8.50(85)	10.8(1.5)	1.27(9)
a06m310	HP	6–30	0.3190(47)	0.54(3)	0.50(5)	1.08(6)	2.17(16)
a06m310	AMA	8–30	0.3268(23)	0.56(3)	0.58(3)	0.95(10)	1.66(11)
a06m220	HP	6–30	0.3149(84)	0.61(8)	12.5(2.0)	32.3(7.3)	2.59(28)
a06m220	AMA	8–30	0.3069(18)	0.63(3)	11.3(4)	39.2(5.0)	3.47(35)

TABLE IV. Same as Table III except that the fit range used is listed as case 3 in Table V.

the 2-point AMA data to be made using a later starting timeslice, $t_{\rm min}$, thus reducing contributions from excited states in the extraction of the masses and amplitudes as shown in Figs. 6 and 7. Similarly, the improvement in the estimates of the matrix elements from the 3-point functions is shown in Figs. 1, 2, 3 and 4.

To summarize, we find that the AMA method with $O(100)$ randomly selected source positions on each configuration is a very cost-effective way to increase the statistics significantly and consequently improve the quality of the fits used to extract the estimates for the charges on each ensemble. Having these estimates with small errors improves the quality of the final fits made to obtain results in the continuum limit and at the physical light-quark mass as discussed in Sec. V.

III. EXCITED-STATE CONTAMINATION

Nucleon charges are given by the matrix elements of the bilinear quark operators between ground-state nucleons. The lattice operator χ given in Eq. (1), however, couples to the nucleon, its excitations and multiparticle states with the same quantum numbers. We incorporate three strategies to reduce excited-state contamination:

- The overlap between the nucleon operator and the excited states is reduced by using tuned smeared sources when calculating the quark propagators. We construct gauge-invariant Gaussian smeared sources by applying the three-dimensional Laplacian operator ∇^2 a fixed number of times $N_{\rm GS}$, $(1 - \sigma^2\nabla^2/(4N_{\rm GS}))^{N_{\rm GS}}$. The smearing parameters $\{\sigma, N_{\rm GS}\}$ for each ensemble are given in Table II and are the same as in Ref. [11] in order to avoid

Fit	$t_{\rm min}$ (2pt HP)	$t_{\rm min}$ (2pt AMA)	$\tau_{\rm skip}$ (3pt)
Case 1	$\{2,4,5\}$	$\{3,5,7\}$	$\{2,3,4\}$
Case 2	$\{2,4,5\}$	$\{3,5,7\}$	$\{3,4,6\}$
Case 3	$\{3,5,6\}$	$\{4,6,8\}$	$\{2,3,4\}$
Case 4	$\{3,5,6\}$	$\{4,6,8\}$	$\{3,4,6\}$

TABLE V. The fit parameters $t_{\rm min}$ and $\tau_{\rm skip}$ defining the four cases used to analyze the 2- and 3-point functions data. The parameter $t_{\rm min}$ is the starting value of time used in the 2-point fit and $\tau_{\rm skip}$ is the number of point skipped adjacent to the source and sink in the fit to the 3-point data. The triplets of numbers correspond to the three lattice spacings $a = \{0.12, 0.09, 0.06\}$ fm, respectively. The three exceptions to these fit ranges are specified in Tables III and IV. The ending timeslices in the 2-point fits, were chosen to be $t_{\rm max} = \{15, 20, 30\}$ in all cases.

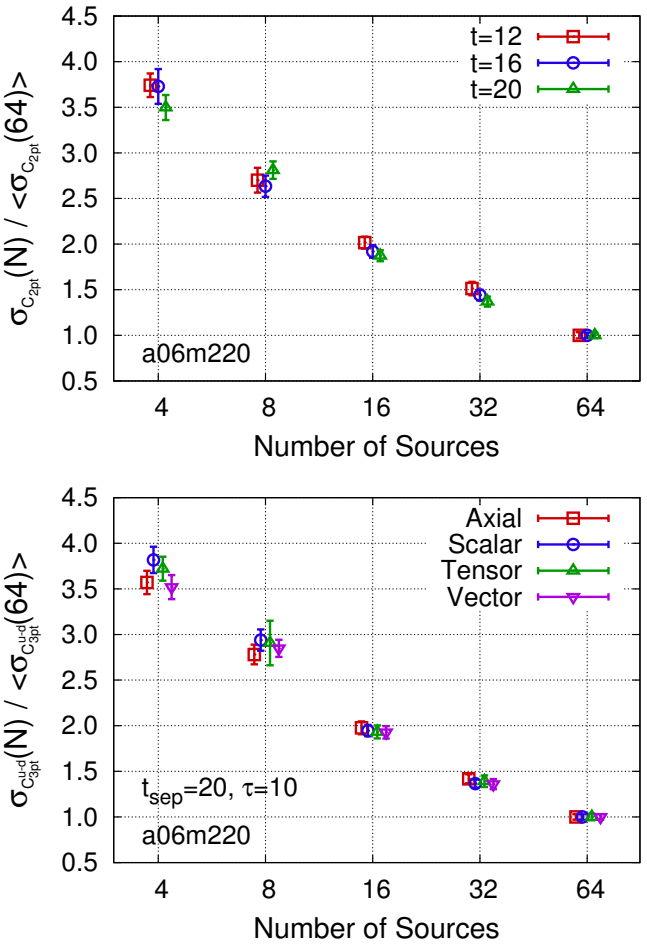

FIG. 5. Illustration of the decrease in the errors in the 2- and 3-point functions calculated on the $a06m220$ lattices with the number N of LP measurements made per configuration. (Top) The 2-point nucleon correlation function at time separations 12, 16, 20. (Bottom) The data for the four charges at the midpoint $\tau = 10$ of the $t_{\rm sep} = 20$ calculation. The errors are normalized using the $N = 64$ estimates and decrease by a factor of about 3.7 between $N = 4$ and 64 measurements compared to the expected factor of 4 for uncorrelated data.

repeating the expensive HP calculation needed for the AMA analysis. Also, the same smearing is used at the source and sink points to construct the smeared-smeared 2- and 3-point correlation functions.

- We calculate the 3-point correlation functions for a number of values of the source-sink separation $t_{\rm sep}$ given in Table I. We fit the data at all $t_{\rm sep}$ simultaneously using the 2-state Ansatz given in Eq. (10) to estimate the $t_{\rm sep} \to \infty$ value.
- We include one excited state in the analysis of the 2-point and 3-point functions as given in Eqs. (9) and (10). We find that this Ansatz has enough free parameters to fit the data and the additional five parameters needed to include a second excited state would be very poorly determined.

The 2-state Ansatz used to fit the 2- and 3-point functions is,

$$C^{\rm 2pt}(t_f, t_i) = |\mathcal{A}_0|^2 e^{-M_0(t_f-t_i)} + |\mathcal{A}_1|^2 e^{-M_1(t_f-t_i)}, \quad (9)$$

$$\begin{aligned} C^{\rm 3pt}_\Gamma(t_f, \tau, t_i) = & \\ & |\mathcal{A}_0|^2 \langle 0|\mathcal{O}_\Gamma|0\rangle e^{-M_0(t_f-t_i)} + \\ & |\mathcal{A}_1|^2 \langle 1|\mathcal{O}_\Gamma|1\rangle e^{-M_1(t_f-t_i)} + \\ & \mathcal{A}_0\mathcal{A}_1^* \langle 0|\mathcal{O}_\Gamma|1\rangle e^{-M_0(\tau-t_i)} e^{-M_1(t_f-\tau)} + \\ & \mathcal{A}_0^*\mathcal{A}_1 \langle 1|\mathcal{O}_\Gamma|0\rangle e^{-M_1(\tau-t_i)} e^{-M_0(t_f-\tau)}, \end{aligned} \quad (10)$$

where τ is the time at which the operator is inserted and $t_f - t_i = t_{\rm sep}$ in the 3-point function calculation. The states $|0\rangle$ and $|1\rangle$ represent the ground and "first excited" nucleon states, respectively. To extract the charges g_A^{u-d}, g_S^{u-d} and g_T^{u-d}, we only need to examine the real part of the correlation functions with the operator insertion at zero momentum, in which case $\mathcal{A}_0$ and $\mathcal{A}_1$ are real and the matrix element $\langle 0|\mathcal{O}_\Gamma|1\rangle = \langle 1|\mathcal{O}_\Gamma|0\rangle$. Thus, we need to extract seven parameters from fits to the 2- and 3-point functions. The four parameters, M_0, M_1, $\mathcal{A}_0$ and $\mathcal{A}_1$ are estimated first from the 2-point data and are then used as inputs in the extraction of matrix elements from fits to the 3-point data. Fits to both 2- and 3-point data are done within the same Jackknife process to take into account correlations.

Five of the seven parameters, M_0, M_1 and the three matrix elements $\langle 0|\mathcal{O}_\Gamma|0\rangle$, $\langle 0|\mathcal{O}_\Gamma|1\rangle$ and $\langle 1|\mathcal{O}_\Gamma|1\rangle$ are physical once the discretization errors and higher excited-state contaminations have been removed from them. The amplitudes $\mathcal{A}_0$ and $\mathcal{A}_1$ depend on the choice of the interpolating nucleon operator and the smearing parameters used to generate the smeared sources. It is clear from Eqs. (9) and (10) that the ratio of the amplitudes, $\mathcal{A}_1/\mathcal{A}_0$, is the quantity to minimize in order to reduce excited-state contamination since it determines the relative strength of the overlap of the nucleon operator with the first excited-state. Estimates of $\langle 0|\mathcal{O}_\Gamma|1\rangle$, $\langle 1|\mathcal{O}_\Gamma|1\rangle$,

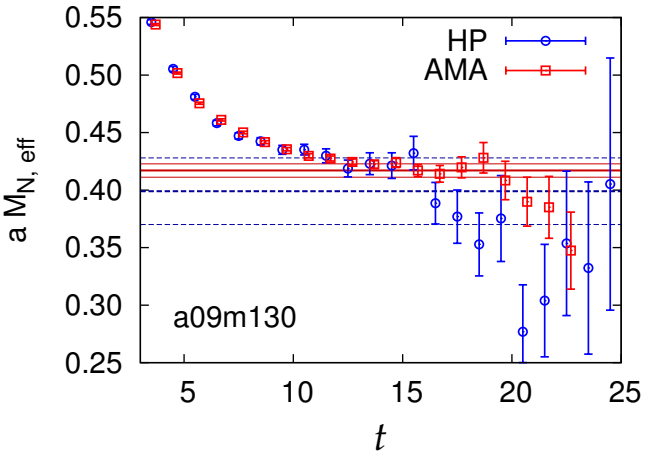

FIG. 6. Effective-mass plot for the nucleon on the $a09m130$ ensemble. The solid line and the error band is the estimate of M_0 from the fits to the AMA (red) data. The dashed blue line and the error band give the HP (blue) estimate. The fit ranges used correspond to Case 3 defined in Table V. Results for all the 9 ensembles are given in Table IV.

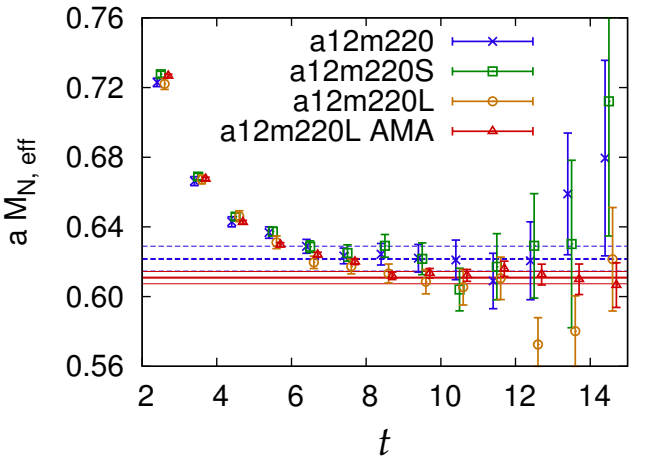

FIG. 7. Effective-mass plots for the nucleon on the $a12m220S$, $a12m220$, $a12m220L$ and $a12m220L$ with AMA ensembles. The two bands with errors are the results for M_0 from the 2-state fit for the $a12m220$ (blue dashed) and $a12m220L$ with AMA (red solid) ensembles. These two estimates differ by a combined 1σ. The estimates of the masses and the amplitudes for all four calculations are summarized in Table IV. The fit ranges used correspond to Case 3 defined in Table V.

the mass gap $M_1 - M_0$, and the ratio $\mathcal{A}_1/\mathcal{A}_0$ can be used, post facto, to bound the size of the excited-state contamination for a given source-sink separation $t_{\rm sep}$.

Results of the 2-state fits to the 2-point functions needed to extract M_0, M_1, $\mathcal{A}_0$ and $\mathcal{A}_1$ are consistent within errors for two sets of starting timeslices $t_{\rm min}$ as shown in Tables III and IV. The χ^2/d.o.f. of the correlated fits are also similar for the two fit ranges. These fit ranges are specified in Table V.

Higher statistics with the AMA method allow us to fit the data with larger $t_{\rm min}$. The HP and AMA estimates for M_0 and $\mathcal{A}_0$ with different fit range are consistent for all the ensembles and are independent of $t_{\rm min}$. This is expected since these ground-state estimates are sensitive only to the data at large t and that is the same in both choices of the fit ranges. We also note that the scaling of the errors is consistent with the naïve expectation, $\sqrt{N_{HP}/N_{LP}}$.

We illustrate the improvement with the AMA method compared to just the HP analysis in Fig. 6 using the $a09m130$ data fit with $t_{\rm min} = 6$. The plateau in the effective-mass $M_{\rm eff}(t+0.5) = -\log\{C^{\rm 2pt}(t+1)/C^{\rm 2pt}(t)\}$, where $C^{\rm 2pt}(t)$ is the 2-point nucleon correlation function at time separation t, extends about four timeslices further with the AMA data. In the limit $t \to \infty$, $M_{\rm eff}(t)$ converges to the ground-state mass M_0. A comparison of the error estimates in both the data points and in the result of the fit shows that the extraction of the masses and the amplitudes improves very significantly with the AMA method.

The data in Tables III and IV show a 2σ difference in the extraction of M_0 from the four ensembles $a12m220S$, $a12m220$, $a12m220L$ (HP) and $a12m220L$ with AMA[2]. The effective-mass data for the four calculations is shown in Fig. 7. The errors in the $a12m220S$, $a12m220$ data are large and the data show a noisy plateau over the range $7 \le t \le 10$. As a result, the 2-state fit is sensitive to the choice of $t_{\rm min}$. The higher statistics and larger volume $a12m220L$ AMA data show a plateau over the interval $9 \le t \le 15$ and the fit is stable under changes in $t_{\rm min}$. Because of this difference in the quality of the data, it is difficult to assess if the $t \to \infty$ estimates have been obtained in the $a12m220S$ and $a12m220$ data. As a result, we are not able to determine what fraction of the difference in M_0 is due to finite-volume effects and how much is due to statistics.

The quantities that are harder to extract and are sensitive to the choice of $t_{\rm min}$ are M_1 and $\mathcal{A}_1$. In most cases, results of fits with larger $t_{\rm min}$ (Case 3 versus Case 1 in Table V) yield smaller values for M_1 and $\mathcal{A}_1$. This is expected since, within a 2-state fit Ansatz, these parameters effectively capture the contributions of all the higher states and fitting with larger $t_{\rm min}$ uses data with relatively less higher-states contamination. In practice, one has to compromise between using data with smaller errors at smaller $t_{\rm min}$ and picking a large $t_{\rm min}$ to reduce higher excited-state contamination. We have picked the second set with the larger $t_{\rm min}$ for presenting our final

[2] We checked for bias in the $a12m220L$ data using the $t_{\rm sep} = 10$ HP data and found it to be negligible as in the other four AMA studies. Assuming that this is true at other values of $t_{\rm sep}$, we include the $a12m220L$ LP data as part of the AMA discussion.

results. Note that the error estimates are slightly larger with this choice.

As discussed above, we need to minimize the ratio of the amplitudes, $\mathcal{A}_1/\mathcal{A}_0$, to reduce the overlap of the nucleon operator with the first excited-state by tuning the smearing parameters. (In general, all the $\mathcal{A}_n/\mathcal{A}_0$ when up to n excited states are included in the fit Ansatz). Our additional tests on the $a06$ ensembles discussed in Sec. VI show that increasing the smearing size σ over the range simulated reduces $\mathcal{A}_1/\mathcal{A}_0$ and the excited-state contamination, most notably in the axial and scalar charges. On the other hand, beyond a certain size σ, the statistical errors based on a given number of gauge configurations start to increase. Also, when calculating the form factors, one expects the optimal σ to decrease with increasing momentum. Thus, one has to compromise between obtaining a good statistical signal and reducing excited-state contamination in both the charges and the form factors, when all these quantities are being calculated with a single choice of the smearing parameters.

The data in Tables III and IV show an increase in the ratio $\mathcal{A}_1/\mathcal{A}_0$ as the lattice spacing is decreased. This suggests that the smearing parameter σ (see Table II) should have been scaled with the lattice spacing a. The dependence of the ratio on the two choices of $t_{\rm min}$ used in the fits (estimates in Table III versus Table IV) and between the HP and AMA estimates for each choice is much smaller. Based on these trends and additional tests discussed in Sec. VI, a better choice for the smearing parameters when calculating the matrix elements at zero-momentum transfer is estimated to be $\{5, 70\}$, $\{7, 120\}$ and $\{9, 200\}$ for the $a = 0.12,\ 0.09$ and 0.06 fm ensembles, respectively. In physical units, a rule-of-thumb estimate for tuning the smearing size is $\sigma a \approx 0.55$ fm.

To extract the three matrix elements $\langle 0|\mathcal{O}_\Gamma|0\rangle$, $\langle 1|\mathcal{O}_\Gamma|0\rangle$ and $\langle 1|\mathcal{O}_\Gamma|1\rangle$, for each operator $\mathcal{O}_\Gamma = \mathcal{O}_{A,S,T,V}$, from the 3-point functions, we make one overall fit using the data at all values of the operator insertion time τ and the various source-sink separations $t_{\rm sep}$ using Eq (10). From such fits we extract the $t_{\rm sep} \to \infty$ estimates under the assumption that the contribution of all higher states is isolated by the 2-state Ansatz given in Eqs. (9) and (10).

In Figs. 8, 9 and 10, we show the data for the unrenormalized isovector charges g_A^{u-d}, g_S^{u-d} and g_T^{u-d} for the seven ensembles at different values of a and M_π used in the final analysis. The other two ensembles, $a12m220S$ and $a12m220$ at $a = 0.114$ fm and $M_\pi = 227$ MeV, allow us to study the finite-volume effect. The data at central values of $\tau \approx t_{\rm sep}/2$ show significant, about 15%, dependence of g_A^{u-d} on $t_{\rm sep}$ between 1 and 1.5 fm for the $a = 0.09$ and 0.06 fm ensembles. In g_T^{u-d}, this effect is less than 5%. The size of the effect in g_S^{u-d} is not clear due to the much larger errors. Based on these data and additional tests discussed in Sec. VI, the two key observations are: (i) the 2-state Ansatz given in Eqs. (9) and (10) fits the data at multiple values of $t_{\rm sep}$ and gives a reliable estimate of the $t_{\rm sep} \to \infty$ value, and (ii) the behavior of the unrenormalized data versus τ and $t_{\rm sep}$ are less sensitive to the value of M_π for fixed a compared to versus a for fixed M_π. The behavior of the renormalized charges is discussed in Sec. V.

The estimates of the matrix elements obtained from the fits to the 3-point correlation functions for the unrenormalized charges are given in Tables VI, VII and VIII for the nine ensembles. Again, for the case of the five ensembles analyzed using the AMA method, we give the HP and the AMA estimates. For each of the two choices of fit ranges for the 2-point functions, listed in Tables III and IV, we determined the three matrix elements for two different choices of the number of time-slices, $\tau_{\rm skip}$, skipped on either end of the 3-point correlation functions. These two choices are $\tau_{\rm skip} = \{2, 3, 4\}$ and $\{3, 4, 6\}$ for the three lattice spacings $a = \{0.12, 0.09, 0.06\}$ fm, respectively. The four cases of fit parameters used in the analysis are summarized in Table V.

The results for $\langle 0|\mathcal{O}_\Gamma|0\rangle$ for all four cases (two fit ranges for the 2-point functions and two choices of $\tau_{\rm skip}$ for the 3-point functions) are consistant as shown in Tables VI, VII and VIII. Estimates of $\langle 0|\mathcal{O}_\Gamma|1\rangle$ and $\langle 1|\mathcal{O}_\Gamma|1\rangle$ are also similar between Case 1 and Case 3, especially for the data with the AMA method. We choose Case 3 for our final estimates as it has (i) the larger $t_{\rm min}$ corresponding to a larger suppression of excited-states in the 2-point fits; and (ii) the smaller value for $\tau_{\rm skip}$ whereby more points at each $t_{\rm sep}$ are included in the 3-point fits to give a better determination of $\langle 0|\mathcal{O}_\Gamma|1\rangle$. Lastly, note that the estimates from the HP data presented here are consistent but slightly different from those published in Ref. [11] because of the different choices of the fit ranges.

The consistency between the four estimates of the matrix elements allows us to draw the following qualitative conclusions regarding excited-state contamination in g_A^{u-d}, g_S^{u-d} and g_T^{u-d}.

- Estimates of $\langle 1|\mathcal{O}_\Gamma|1\rangle$ given in Tables VI, VII and VIII are poorly determined. Within the 2-state approximation, the effect of a nonzero $\langle 1|\mathcal{O}_\Gamma|1\rangle$ is to change the data at all τ, for fixed $t_{\rm sep}$, by a constant amount. For g_A^{u-d}, $\langle 1|\mathcal{O}_\Gamma|1\rangle$ is large on the $a = 0.09$ and 0.06 fm ensembles and has the same sign as $\langle 0|\mathcal{O}_\Gamma|1\rangle$. The two contributions, therefore, add to give a large excited-state contribution. For g_T^{u-d}, the data in Fig. 10 show less than 5% dependence on $t_{\rm sep}$ in the central regions (values of operator insertion time τ at which the contribution of a nonzero $\langle 0|\mathcal{O}_\Gamma|1\rangle$ is the smallest) and the contribution of $\langle 1|\mathcal{O}_\Gamma|1\rangle$ is small. For g_S^{u-d}, the data in Fig. 9 show a significant excited-state effect only for the $a = 0.06$ fm ensembles that is largely accounted for by the contribution of the $\langle 0|\mathcal{O}_S|1\rangle$ term.

- Estimates of $\langle 0|\mathcal{O}_S|1\rangle$ vary between -0.05 and -0.41 for g_S^{u-d}. This matrix element gives the negative curvature observed in Fig. 9, and the ground-state estimate of g_S^{u-d} converges from below.

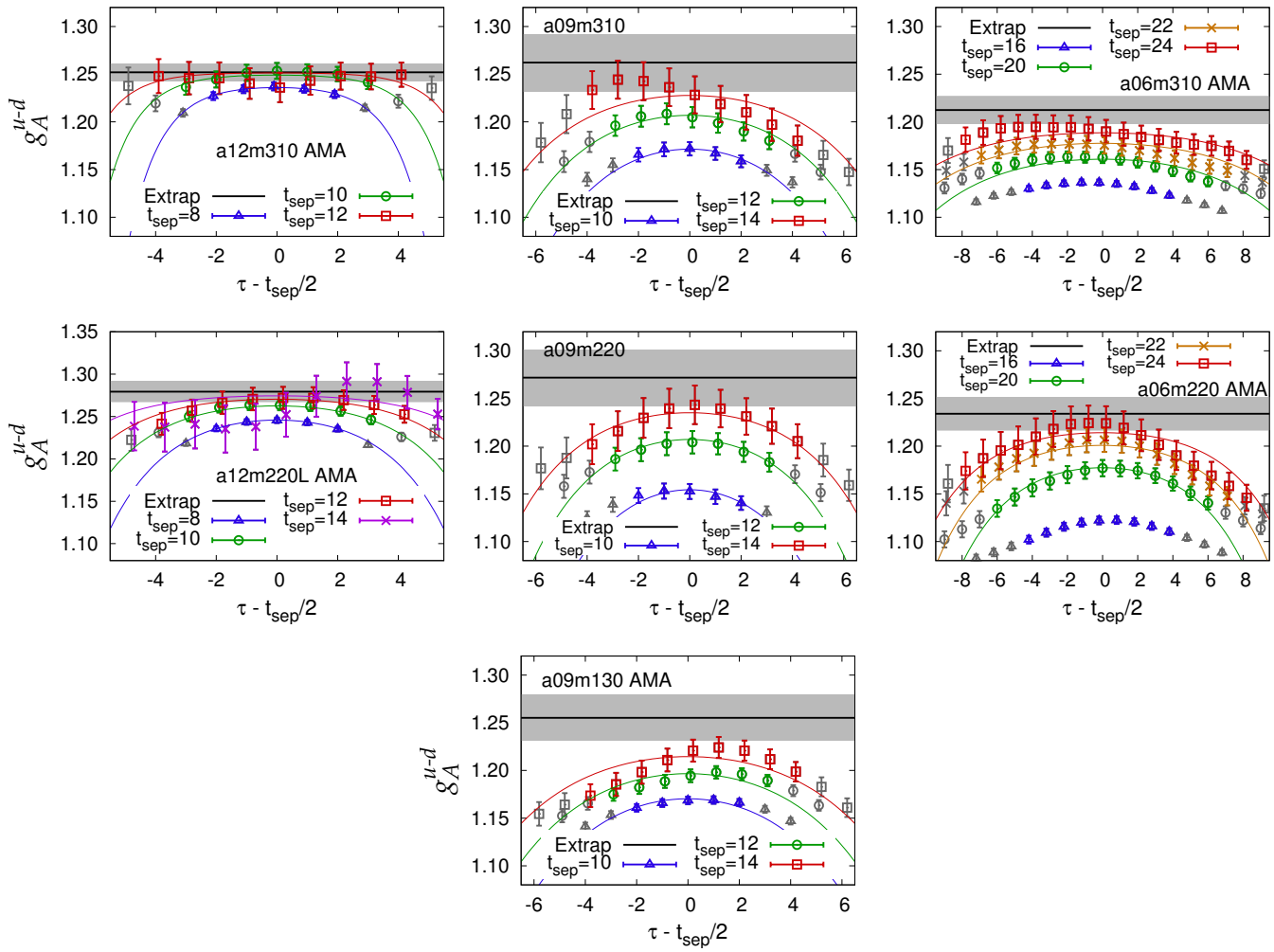

FIG. 8. The 2-state fit to the unrenormalized axial charge g_A^{u-d} data for the seven ensembles at different values of the lattice spacing and pion mass. The grey error band and the solid line within it is the $t_{\rm sep} \to \infty$ estimate obtained using the 2-state fit. The result of the fit for each individual $t_{\rm sep}$ is shown by a solid line with the same color as the data points. Note that the data with $t_{\rm sep} = 16$ in the two $a06$ ensembles are not used in the fit.

- Data for g_S^{u-d} show excited-state contamination on the two $a = 0.06$ fm ensembles $a06m310$ and $a06m220$. The 2-state fit gives reliable $t_{\rm sep} \to \infty$ estimates as shown in Fig. 9. In Sec. VI, we present data from additional simulations on the $a06m310$ and $a06m220$ ensembles and discuss the limitations of the 2-state fit when the errors are large and the data at different $t_{\rm sep}$ overlap as a result.

- Estimates of $\langle 0|\mathcal{O}_T|1\rangle$ vary between 0.1 and 0.26 for g_T^{u-d} and give rise to the positive curvature evident in Fig. 10. The ground-state estimate of g_T^{u-d} converges from above.

- There is evidence for excited-state contamination in g_T^{u-d} on the $a12m310$, $a12m220L$ and $a09m130$ ensembles with AMA as shown in Fig. 10. This 5% effect can be accounted for by the larger value of $\langle 1|\mathcal{O}_\Gamma|1\rangle$ that has the same sign as the $\langle 0|\mathcal{O}_\Gamma|1\rangle$ contribution as shown in Table VIII. In all three cases, the 2-state Ansatz fits the data at multiple values of $t_{\rm sep}$ covering the range 1.0–1.4 fm, and gives stable $t_{\rm sep} \to \infty$ estimates under changes in $\tau_{\rm skip}$ and $t_{\rm sep}$.

- In all cases, the data with the largest $t_{\rm sep}$ are noisy and do not contribute significantly to the fit. Much higher-statistics are needed for fits to be sensitive to data with $t_{\rm sep} \gtrsim 1.5$ fm.

Our conclusion is that the 2-state fit reduces the uncertainty due to the excited-state contamination in g_A^{u-d}, g_S^{u-d} and g_T^{u-d} to within a few percent (size of the statistical errors) with the smearing parameters and values of $t_{\rm sep}$ we have used. Also, the data in Tables VI, VII and VIII indicate that the variation in the determination of $\mathcal{A}_1/\mathcal{A}_0$ and $M_1 - M_0$ with different choices of the fit ranges does not have a significant effect on the final

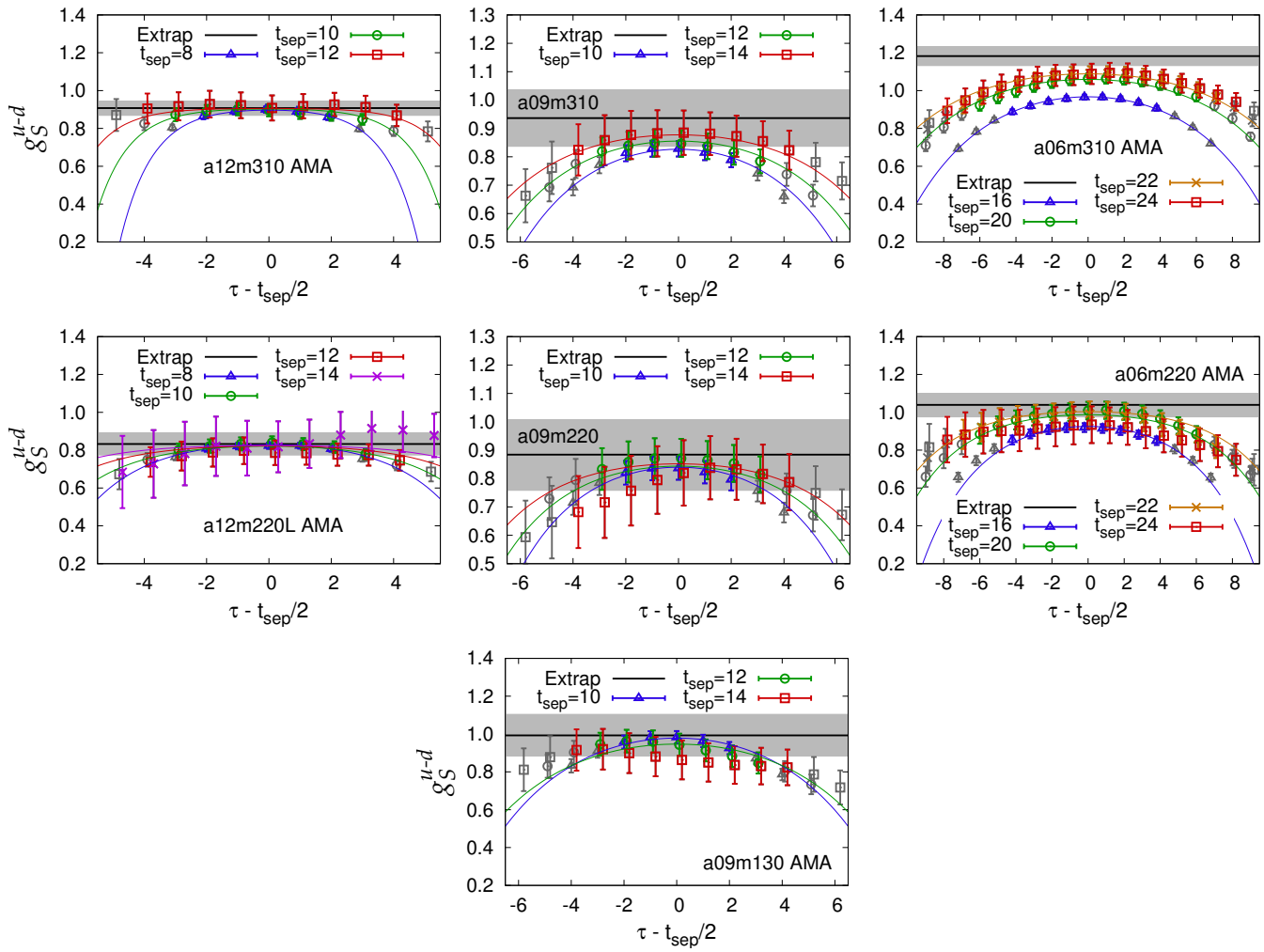

FIG. 9. The 2-state fit results for the unrenormalized scalar charge g_S^{u-d} data. The rest is the same as in Fig. 8.

$t_{\rm sep} \to \infty$ estimates of the charges obtained from the 2-state fits.

IV. RENORMALIZATION OF OPERATORS

The calculation of the renormalization constants Z_A, Z_V, Z_S and Z_T of the quark bilinear operators in the RI-sMOM scheme [32, 33] has been done on six ensembles: *a12m310, a12m220, a09m310, a09m220, a06m310* and *a06m220*. The method and the details of this calculation have been given in Ref. [11] and here we briefly describe new aspects of the calculations and state the results.

To derive Z_A, Z_S, Z_S and Z_V in the continuum $\overline{\rm MS}$ scheme at $\mu = 2\,$GeV, starting with the lattice results obtained in the RI-sMOM scheme, we proceed as follows. The RI-sMOM estimate obtained at a given lattice squared four-momentum q^2 is first converted to the $\overline{\rm MS}$ scheme at the same scale (horizontal matching) using two-loop perturbative relations expressed in terms of the coupling constant $\alpha_{\overline{\rm MS}}(q^2)$ [34]. This estimate at $\mu = q^2$, is then run in the continuum in the $\overline{\rm MS}$ scheme to 2 GeV using the 3-loop anomalous dimension relations for the scalar and tensor bilinears [5, 35]. The result is a set of data points as a function of q^2 that are shown in Figs. 11 and 12. The mass-independent renormalization factors are extracted from these as discussed below.

In calculations at sufficiently small values of the lattice spacing a, one expects a window, $\eta\Lambda_{\rm QCD} \ll q \ll \xi\pi/a$, in which the data for the Z's, shown in Figs. 11 and 12, are independent of q; that is, the data should show a plateau versus q. The lower cutoff $\eta\Lambda_{\rm QCD}$ is dictated by nonperturbative effects and the upper cutoff $\xi\pi/a$ by discretization effects. Here η and ξ are, *a priori*, unknown dimensionless numbers of $O(1)$ that depend on the lattice action and the link smearing procedure. The main systematics contributing to the lack of such a window and the resulting uncertainty in the extraction of the renormalization constants are (i) breaking of the Euclidean $O(4)$ rotational symmetry to the hypercubic group, because of which different combinations of q_μ with the same q^2 give different results in the RI-sMOM scheme; (ii)

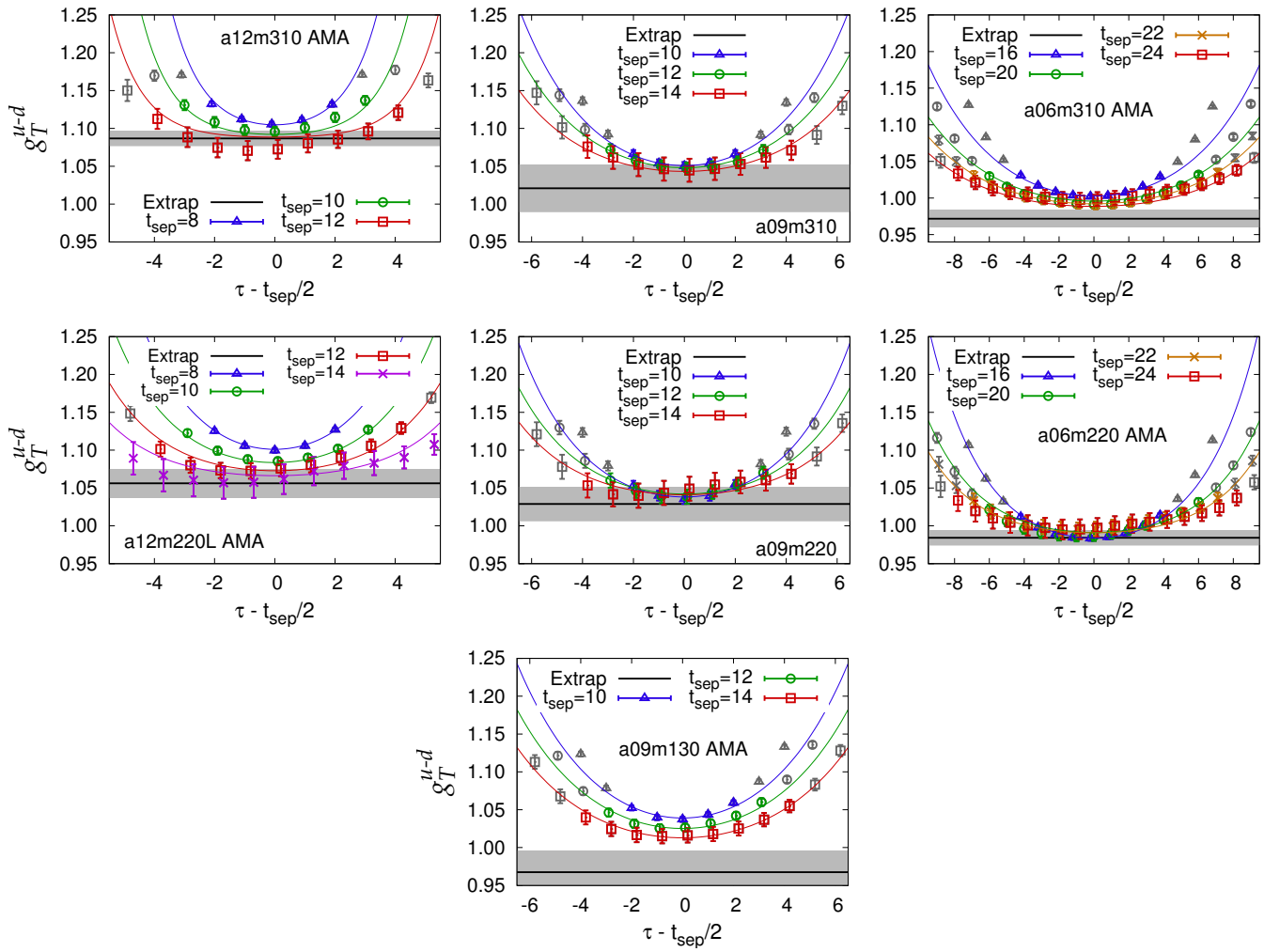

FIG. 10. The 2-state fit results for the unrenormalized tensor charge g_T^{u-d} data. The rest is the same as in Fig. 8.

nonperturbative effects at small q^2; (iii) discretization errors at large q^2 other than the $O(4)$ breaking effects listed above; and (iv) truncation errors in the perturbative matching to the $\overline{\rm MS}$ scheme and running to 2 GeV. These systematics are discussed below.

To assess the truncation errors, we compare the conversion factor using 2-loop matching and 3-loop running versus 1-loop matching and 2-loop running. The 2-loop series for the matching of Z_T is poorly behaved. For example, the 2-loop series for Z_T when using horizontal matching between the RI-sMOM and $\overline{\rm MS}$ scheme is $1 + 0.0052 + 0.0159$ at $q^2 = 4$ GeV^2 and is $1 + 0.0037 + 0.0078$ at $q^2 = 25$ GeV^2. In obtaining these estimates we used the 4-flavor $\alpha_s(\overline{\rm MS}, 2\text{ GeV}) = 0.3051$ and $\alpha_s(\overline{\rm MS}, 5\text{ GeV}) = 0.2138$. On the other hand, the 2-loop series for Z_S at $q^2 = 4$ GeV^2, $1 - 0.0157 - 0.0039$, is much better behaved. The poor convergence of the 2-loop matching factor suggests a systematic uncertainty of $O(2\%)$ for Z_T. Our final error estimates given in Table X are larger than this. The series for the factor describing the running in the continuum is better behaved and the difference between the 2- and 3-loop estimate between the values of q^2 used in the analysis and 4 GeV^2 is less than 20% of the quoted errors and starts to become significant only for $q^2 < 1$ GeV^2 where α_s is large. Consequently, we use data with $q^2 > 4$ GeV^2 when obtaining our final estimates given in Tables IX and XII.

The lattice data in the RI-sMOM scheme have significant $O(4)$ breaking effects. The size of the spread in Z_A, Z_S, Z_T and Z_V and in the ratios Z_A/Z_V, Z_S/Z_V, and Z_T/Z_V is illustrated in Fig. 13 using the $a06m220$ ensemble by plotting all the data using green circles. From this full data set, we pick the points with the smallest value of $\sum_\mu (p_1)_\mu^4/((p_1)^2)^2 + \sum_\mu (p_2)_\mu^4/((p_2)^2)^2$, where $(p_1)_\mu$ and $(p_2)_\mu$ are the momenta in the two external fermion legs, $q_\mu = (p_1)_\mu - (p_2)_\mu$ and $(p_i)^2 = \sum_\mu (p_i)_\mu^2$. These points, shown as red diamonds, are expected to have smaller $O(4)$ breaking effects. Of these red points, the data between 9.2–11.2 GeV^2 used to extract the Z's using method B discussed below are shown as black diamonds.

The data for the ratios Z_A/Z_V, Z_S/Z_V, and Z_T/Z_V

		$\langle 0\|\mathcal{O}_A\|0\rangle$				Case 1		Case 3	
ID	Type	Case 1	Case 2	Case 3	Case 4	$\langle 0\|\mathcal{O}_A\|1\rangle$	$\langle 1\|\mathcal{O}_A\|1\rangle$	$\langle 0\|\mathcal{O}_A\|1\rangle$	$\langle 1\|\mathcal{O}_A\|1\rangle$
a12m310	HP	1.249(22)	1.246(26)	1.248(26)	1.243(33)	−0.019(42)	−2.4(62)	−0.016(46)	0.4(2.8)
a12m310	AMA	1.252(9)	1.251(11)	1.252(9)	1.251(11)	−0.060(24)	−22(28)	−0.060(24)	−22(28)
a12m310	LP	1.252(9)	1.251(11)	1.252(9)	1.251(11)	−0.060(24)	−22(28)	−0.060(24)	−22(28)
a12m220S	HP	1.275(32)	1.287(39)	1.283(39)	1.295(48)	−0.187(64)	−7.(18)	−0.199(69)	0.6(6.2)
a12m220	HP	1.271(27)	1.265(33)	1.273(30)	1.263(39)	−0.068(58)	−16.0(2.5)	−0.063(63)	−5.(15)
a12m220L	HP	1.285(22)	1.291(25)	1.337(83)	1.346(89)	−0.125(47)		−0.145(60)	
a12m220L	LP	1.276(10)	1.275(14)	1.279(12)	1.276(16)	−0.084(22)	−0.8(18)	−0.087(25)	−0.0(1.7)
a09m310	HP	1.255(21)	1.255(25)	1.262(30)	1.262(30)	−0.118(35)	−0.7(18)	−0.123(38)	−0.3(1.9)
a09m220	HP	1.267(22)	1.277(25)	1.272(30)	1.283(33)	−0.135(34)	−2.0(25)	−0.138(37)	−1.7(2.9)
a09m130	HP	1.172(39)	1.164(46)	1.177(44)	1.163(55)	−0.029(44)	0.4(13)	−0.028(49)	0.84(77)
a09m130	AMA	1.247(16)	1.258(19)	1.255(24)	1.266(27)	−0.096(19)	0.64(35)	−0.102(24)	0.72(38)
a09m130	LP	1.247(16)	1.257(19)	1.255(24)	1.265(26)	−0.094(19)	0.60(36)	−0.100(23)	0.69(38)
a06m310	HP	1.167(22)	1.156(26)	1.172(24)	1.157(29)	−0.020(22)	0.03(70)	−0.019(24)	0.45(50)
a06m310	AMA	1.209(14)	1.209(15)	1.212(14)	1.212(16)	−0.058(16)	−2.3(16)	−0.060(17)	−1.2(1.4)
a06m310	LP	1.210(13)	1.210(15)	1.213(14)	1.213(16)	−0.058(16)	−2.4(17)	−0.061(17)	−1.3(1.4)
a06m220	HP	1.227(50)	1.238(57)	1.234(51)	1.244(60)	−0.182(61)	−0.2(3.1)	−0.186(62)	0.6(2.3)
a06m220	AMA	1.234(17)	1.241(19)	1.234(17)	1.241(19)	−0.122(18)	−6.0(3.2)	−0.121(18)	−6.3(3.9)
a06m220	LP	1.234(17)	1.241(18)	1.234(17)	1.241(18)	−0.117(18)	−7.0(3.4)	−0.116(18)	−7.5(3.9)

TABLE VI. Estimates of the matrix element $\langle 0|\mathcal{O}_A|0\rangle$ for the isovector axial operators for four cases of the fit ranges defined in Table V. We also give estimates of the matrix elements $\langle 0|\mathcal{O}_A|1\rangle$ and $\langle 1|\mathcal{O}_A|1\rangle$ for Case 1 and Case 3. For the four ensembles, $a12m310$, $a09m130$, $a06m310$ and $a06m22$, we give both the AMA and LP estimates. We find that the bias correction term is negligible in all cases.

		$\langle 0\|\mathcal{O}_S\|0\rangle$				Case 1		Case 3	
ID	Type	Case 1	Case 2	Case 3	Case 4	$\langle 0\|\mathcal{O}_S\|1\rangle$	$\langle 1\|\mathcal{O}_S\|1\rangle$	$\langle 0\|\mathcal{O}_S\|1\rangle$	$\langle 1\|\mathcal{O}_S\|1\rangle$
a12m310	HP	0.83(9)	0.79(10)	0.82(10)	0.77(12)	−0.06(11)	10(23)	−0.05(12)	6(11)
a12m310	AMA	0.91(4)	0.91(4)	0.91(4)	0.91(4)	−0.29(5)	6(56)	−0.29(5)	6(56)
a12m310	LP	0.91(4)	0.91(4)	0.91(4)	0.91(4)	−0.29(5)	6(56)	−0.29(5)	6(56)
a12m220S	HP	1.01(27)	1.03(30)	1.03(32)	1.07(37)	−0.16(22)	−40(13)	−0.17(26)	−11(38)
a12m220	HP	0.69(16)	0.64(18)	0.67(18)	0.61(20)	−0.07(16)	80(14)	−0.06(18)	35(77)
a12m220L	HP	1.01(10)	1.00(10)	1.10(17)	1.08(17)	−0.34(15)		−0.39(18)	
a12m220L	LP	0.83(5)	0.83(7)	0.83(6)	0.83(7)	−0.18(6)	4.9(6.2)	−0.20(7)	4.1(4.8)
a09m310	HP	0.92(9)	0.93(10)	0.94(10)	0.94(11)	−0.33(9)	1.1(2.5)	−0.34(10)	1.2(2.1)
a09m220	HP	0.88(12)	0.86(13)	0.88(13)	0.87(14)	−0.28(10)	2.7(4.2)	−0.28(11)	2.7(3.8)
a09m130	HP	0.70(32)	0.72(36)	0.73(37)	0.75(42)	−0.27(17)	3.4(9.6)	−0.29(19)	2.5(5.5)
a09m130	AMA	0.98(10)	0.97(11)	0.99(11)	0.97(12)	−0.37(6)	4.0(1.6)	−0.40(9)	3.8(1.5)
a09m130	LP	0.99(10)	0.97(11)	1.00(11)	0.98(11)	−0.36(6)	3.9(1.6)	−0.39(8)	3.6(1.4)
a06m310	HP	1.24(10)	1.22(11)	1.28(11)	1.24(12)	−0.26(6)	−3.4(2.1)	−0.28(7)	−1.8(1.6)
a06m310	AMA	1.16(4)	1.17(5)	1.18(5)	1.19(5)	−0.38(3)	−1.1(1.1)	−0.40(4)	−0.5(1.0)
a06m310	LP	1.16(4)	1.17(5)	1.18(5)	1.19(5)	−0.38(3)	−1.1(1.1)	−0.40(4)	−0.5(1.0)
a06m220	HP	0.65(28)	0.60(29)	0.64(29)	0.59(31)	−0.21(14)	11(17)	−0.21(15)	8.(13)
a06m220	AMA	1.04(6)	1.05(7)	1.04(6)	1.05(7)	−0.30(4)	−0.6(2.5)	−0.30(4)	−0.7(2.6)
a06m220	LP	1.04(6)	1.05(7)	1.04(6)	1.05(7)	−0.30(3)	−1.1(2.5)	−0.30(3)	−1.2(2.6)

TABLE VII. Estimates of the matrix elements for the isovector scalar operator. The rest is the same as in Table VI.

show much smaller $O(4)$ breaking, presumably because some of the systematics cancel. Our final estimates of the renormalized charges are, therefore, obtained using these ratios as discussed below. Overall, a better understanding and control over the artifacts due to $O(4)$ symmetry breaking in the RI-sMOM scheme is needed as the contribution of the uncertainty in the renormalization constants to the errors in the charges is now larger than the statistical errors and the excited-state contamination.

After conversion to the $\overline{\text{MS}}$ scheme at 2 GeV, the selected data points that minimize $\sum_\mu (p_1)_\mu^4/((p_1)^2)^2 + \sum_\mu (p_2)_\mu^4/((p_2)^2)^2$ for each q^2 are plotted in Fig. 11 for the six ensembles as a function of q^2. The data for Z_Γ and Z_Γ/Z_V show nonperturbative effects at low $|q|$ values followed by an approximate plateau for Z_A, Z_T, and Z_V, whereas the data for Z_S continue to show a large q dependence.

From these data in the $\overline{\text{MS}}$ scheme at 2 GeV, we extract the estimates in two ways [11]:

		$\langle 0\|\mathcal{O}_T\|0\rangle$				Case 1		Case 3	
ID	Type	Case 1	Case 2	Case 3	Case 4	$\langle 0\|\mathcal{O}_T\|1\rangle$	$\langle 1\|\mathcal{O}_T\|1\rangle$	$\langle 0\|\mathcal{O}_T\|1\rangle$	$\langle 1\|\mathcal{O}_T\|1\rangle$
a12m310	HP	1.096(21)	1.092(24)	1.084(31)	1.081(33)	0.187(32)	−2.5(4.9)	0.200(35)	−0.5(2.4)
a12m310	AMA	1.087(10)	1.082(10)	1.087(10)	1.082(10)	0.243(20)	12(14)	0.243(20)	12(14)
a12m310	LP	1.087(10)	1.082(10)	1.087(10)	1.082(10)	0.243(20)	13(14)	0.243(20)	13(14)
a12m220S	HP	1.086(26)	1.079(31)	1.067(46)	1.060(51)	0.264(55)	−1(11)	0.280(57)	0.3(3.3)
a12m220	HP	1.111(24)	1.107(28)	1.105(32)	1.102(36)	0.202(47)	−17(22)	0.209(49)	−6(14)
a12m220L	HP	1.058(19)	1.059(20)	1.043(29)	1.050(29)	0.168(33)		0.193(43)	
a12m220L	LP	1.063(12)	1.063(13)	1.056(19)	1.058(18)	0.200(17)	1.31(74)	0.213(25)	1.03(60)
a09m310	HP	1.025(24)	1.027(26)	1.021(31)	1.023(31)	0.157(24)	0.10(87)	0.164(30)	0.15(80)
a09m220	HP	1.030(20)	1.039(21)	1.029(22)	1.039(22)	0.124(25)	−0.3(1.1)	0.127(26)	−0.2(1.1)
a09m130	HP	0.993(33)	1.001(36)	0.980(45)	0.993(47)	0.136(36)	0.48(88)	0.147(40)	0.63(53)
a09m130	AMA	0.974(20)	0.981(20)	0.967(28)	0.975(26)	0.164(16)	0.79(14)	0.174(25)	0.75(12)
a09m130	LP	0.973(19)	0.979(19)	0.966(28)	0.974(26)	0.167(16)	0.77(14)	0.177(25)	0.72(12)
a06m310	HP	0.961(20)	0.958(22)	0.951(24)	0.950(26)	0.124(15)	0.68(40)	0.131(16)	0.75(27)
a06m310	AMA	0.976(10)	0.981(10)	0.972(12)	0.978(12)	0.122(9)	0.46(26)	0.128(10)	0.50(22)
a06m310	LP	0.976(10)	0.981(10)	0.972(12)	0.978(12)	0.122(9)	0.45(26)	0.128(10)	0.49(22)
a06m220	HP	0.995(43)	1.002(47)	0.990(48)	1.000(51)	0.109(38)	−0.5(2.5)	0.110(39)	0.0(1.9)
a06m220	AMA	0.984(10)	0.986(10)	0.984(10)	0.986(10)	0.103(8)	−0.50(52)	0.103(8)	−0.53(59)
a06m220	LP	0.984(9)	0.985(10)	0.984(9)	0.986(10)	0.105(8)	−0.59(54)	0.105(8)	−0.63(62)

TABLE VIII. Estimates of the matrix elements for the isovector tensor operator. The rest is the same as in Table VI.

- Method A: We fit the data with $q^2 > 0.8$ GeV^2 using the Ansatz $c/q^2 + Z + dq$, where the first term c/q^2 is used to account for nonperturbative artifacts and the third, dq, for the discretization errors. The errors in the Z's are obtained by using 100 bootstrap samples.

- Method B: The estimate for Z is taken to be an average over the data points in an interval about $q^2 = \Lambda/a$, where the scale $\Lambda = 3$ GeV is chosen to be large enough to avoid non-perturbative effects and above which perturbation theory is expected to be reasonably well-behaved. This choice satisfies both $qa \to 0$ and $\Lambda/q \to 0$ in the continuum limit as desired, and $q_\mu a - \sin(q_\mu a) < 0.05$ to bound discretization effects. In our simulations, this choice corresponds to $q^2 = 5$, 6.8 and 10.2 GeV^2 for the $a = 0.12$, 0.09 and 0.06 fm ensembles, respectively. To estimate the value and the error, we, further choose an interval of 2 GeV^2 about these q^2, i.e., we take the mean and the standard deviation of the data over the ranges 4–6, 5.8–7.8 and 9.2–11.2 GeV^2.

The interval of q^2 that contributes to both methods is consistent with the general requirement that $\eta\Lambda_{\rm QCD} \ll q \ll \xi\pi/a$, with η and ξ of $O(1)$, to avoid both nonperturbative and discretization artifacts.

The estimates using method B for all four Z's and at all three values of the lattice spacing are found to overlap for the two values of M_π. As a result, in Ref. [11] we had neglected possible mass dependence in implementing Method A and made a fit using the Ansatz $c/q^2 + Z + dq$ to the combined data. In this work, we analyze the 6 ensembles separately and present the estimates from both methods in Table IX.

The estimates from Method A show significant dependence on M_π in some cases even though the data at the two values of M_π overlap. We do not find a uniform trend with M_π at the three different values of a, and given the size of the errors in the data at the two values of M_π at fixed a we are not able to make a reliable extrapolation in M_π. So we ignore possible dependence on M_π in the data and average the estimates from the two methods at the two values of M_π given in Table IX to obtain a "mass-independent" estimate. For the error estimate we take the larger of the two: half the spread or the largest statistical error.

The data for the ratios Z_Γ/Z_V are shown in Fig. 12. As highlighted above, we find that the systematic effects due to $O(4)$ breaking are smaller in the ratios. The data again show a rough plateau in Z_A/Z_V and Z_T/Z_V but not in Z_S/Z_V. We also find a significant variation with M_π and between the two methods in some cases, which we include in our error estimates as explained above. The final mass-independent renormalization constants Z_Γ and Z_Γ/Z_V at the three lattice spacings are given in Table X. The errors in these renormalization constants are added in quadrature to those in the extraction of the bare nucleon charges $g^{\rm bare}_{A,S,T}$ and $g^{\rm bare}_{A,S,T}/g^{\rm bare}_V$ given in Table XI to obtain the renormalized charges in two ways:

- Using the product of the ratios, $(Z_\Gamma/Z_V) \times (g_\Gamma/g_V^{u-d})$, along with the identity $Z_V g_V^{u-d} = 1$. These are given in Table XII.

- Using the product $Z_\Gamma g_\Gamma$. These estimates are given in Table XIII for the isovector charges.

The two estimates differ by 1–3%. Most of this difference correlates with the deviation of $Z_V g_V^{u-d}$ from unity as shown in Table XIII. The deviation is about 1σ: approximately 3%, 3% and 2% at the three lattice spacings,

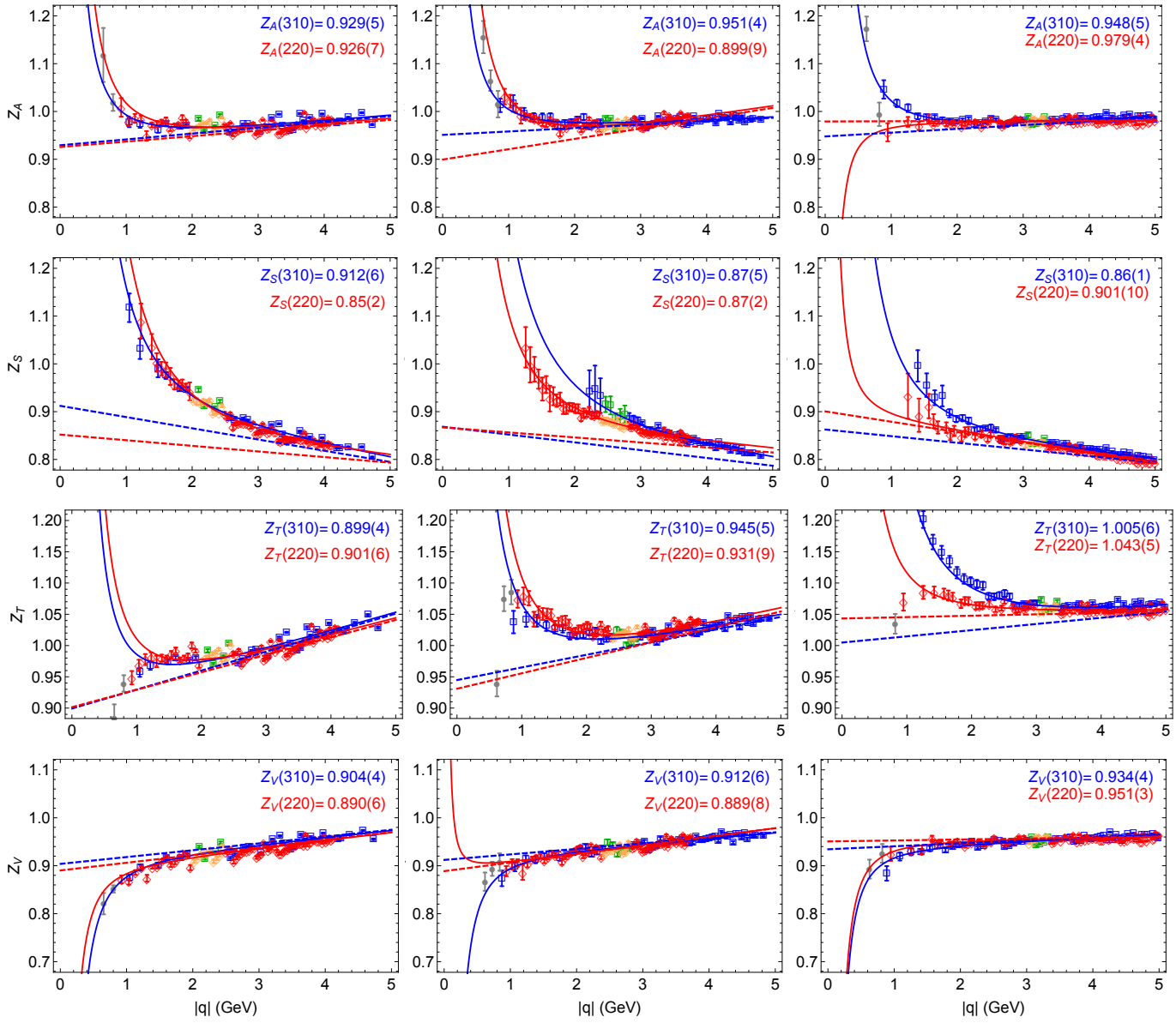

FIG. 11. Data for the four renormalization constants Z_A, Z_S, Z_T and Z_V in the $\overline{\rm MS}$ scheme at $\mu = 2\,$GeV as a function of the lattice momenta $|q|$ used in the RI-sMOM scheme. The data are organized as follows: (left column) $a = 0.12$ fm, (middle column) $a = 0.09$ fm and (right column) $a = 0.06$ fm ensembles. In each panel, we show the data at the two values of M_π analyzed and use blue squares to label the $M_\pi \approx 310$ MeV and red diamonds for the $M_\pi \approx 220$ MeV ensembles. The dashed line is the linear part of the fit $c/q^2 + Z + dq$ used in method A to extract the Z's. Data in the region of q^2 used to extract the Z's using Method B are shown using green ($M_\pi \approx 310$ MeV) and orange ($M_\pi \approx 220$ MeV) symbols.

$a = 0.12$, 0.09 and 0.06 fm, respectively. The magnitude of these deviations is consistent with our estimates of errors in the renormalization constants given in Table X, which are now larger than the statistical errors. A more detailed discussion of the error budget and the final error estimates are given in Sec. VII.

The discretization errors in the two estimates of the renormalized charges are different, so one should only compare the results after extrapolation. In Sec. V, we show that even though the estimates on individual ensembles differ by 1–3%, the value of the charges after extrapolation to the continuum limit and the physical pion mass are consistent. The errors in the data $Z_\Gamma g_\Gamma$ and in the extrapolated value obtained from them are larger. This is because the data for both, Z_Γ/Z_V and g_Γ/g_V^{u-d}, have smaller errors, presumably because some of the systematics cancel in the ratios. Our final estimates are, therefore, obtained using $(Z_\Gamma/Z_V) \times (g_\Gamma/g_V^{u-d})$ with the relation $Z_V g_V^{u-d} = 1$.

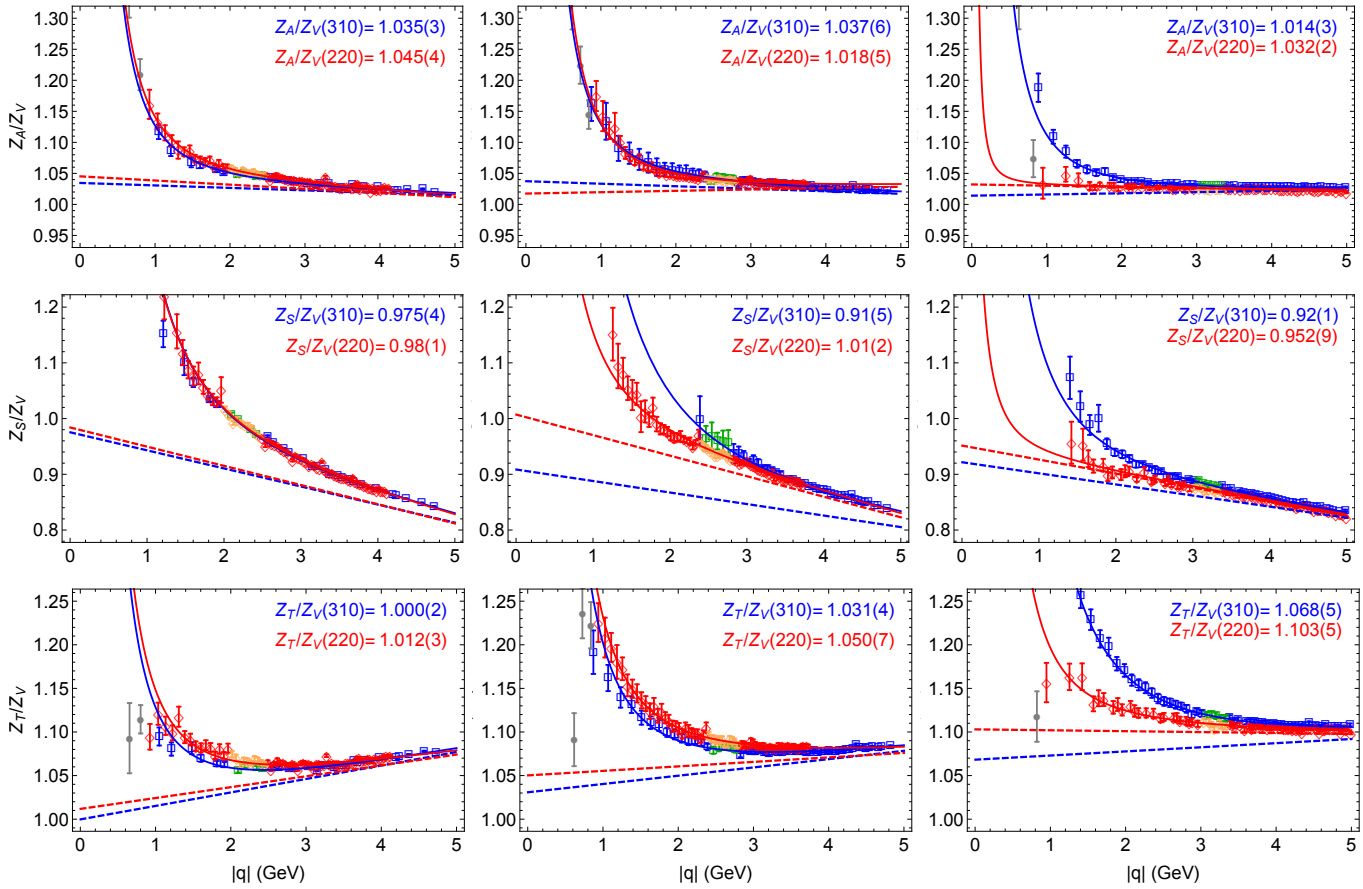

FIG. 12. Data for the ratios of renormalization constants Z_A/Z_V, Z_S/Z_V, Z_T/Z_V in the $\overline{\text{MS}}$ scheme at $\mu = 2\,\text{GeV}$ as a function of the lattice momenta $|q|$ used in the RI-sMOM scheme. The rest is the same as in Fig. 11.

ID	Z_A	Z_S	Z_T	Z_V	Z_A/Z_V	Z_S/Z_V	Z_T/Z_V
a12m310	0.929(5)	0.912(06)	0.899(4)	0.904(4)	1.035(3)	0.975(04)	1.000(2)
a12m220	0.926(7)	0.852(20)	0.901(6)	0.890(6)	1.045(4)	0.984(13)	1.012(3)
a09m310	0.951(4)	0.868(45)	0.945(5)	0.912(7)	1.037(6)	0.909(54)	1.031(4)
a09m220	0.899(9)	0.867(22)	0.931(9)	0.889(8)	1.018(5)	1.007(20)	1.050(7)
a06m310	0.948(5)	0.863(11)	1.005(6)	0.934(4)	1.014(3)	0.922(10)	1.068(5)
a06m220	0.979(4)	0.901(10)	1.043(5)	0.951(3)	1.032(2)	0.952(09)	1.103(5)
a12m310	0.979(1)	0.925(17)	0.989(14)	0.933(14)	1.0472(21)	0.991(17)	1.058(2)
a12m220	0.970(9)	0.914(11)	0.984(9)	0.921(10)	1.0526(35)	0.994(14)	1.068(4)
a09m310	0.975(10)	0.901(13)	1.013(11)	0.937(11)	1.0411(22)	0.962(5)	1.081(2)
a09m220	0.972(7)	0.878(6)	1.018(6)	0.934(7)	1.0407(14)	0.941(8)	1.090(3)
a06m310	0.980(8)	0.840(9)	1.064(8)	0.951(8)	1.0300(6)	0.883(4)	1.118(2)
a06m220	0.981(7)	0.835(3)	1.060(5)	0.957(6)	1.0255(8)	0.873(4)	1.109(3)

TABLE IX. The renormalization constants Z_A, Z_S, Z_T, Z_V and the ratios Z_A/Z_V, Z_S/Z_V and Z_T/Z_V in the $\overline{\text{MS}}$ scheme at 2 GeV obtained on six ensembles at the three values of the lattice spacings. (Top) Estimates are from method A using the fit $1/q^2 + Z + dq$. (Bottom) Estimates from method B obtained by averaging the data over an interval in q^2 as described in the text.

V. RESULTS FOR THE CHARGES g_A, g_S, g_T

To extrapolate the estimates of the renormalized charges given in Table XII to the continuum limit ($a \to 0$), the physical pion mass ($M_{\pi^0} = 135$ MeV) and the infinite volume limit ($L \to \infty$), we need to use an appropriate fit Ansatz, motivated by chiral perturbation theory, for the nine data points. For discussions on predictions of chiral perturbation we direct the reader to Refs. [36–41]. To test these predictions, one ideally requires data at many lattice spacings and small pion masses. Also,

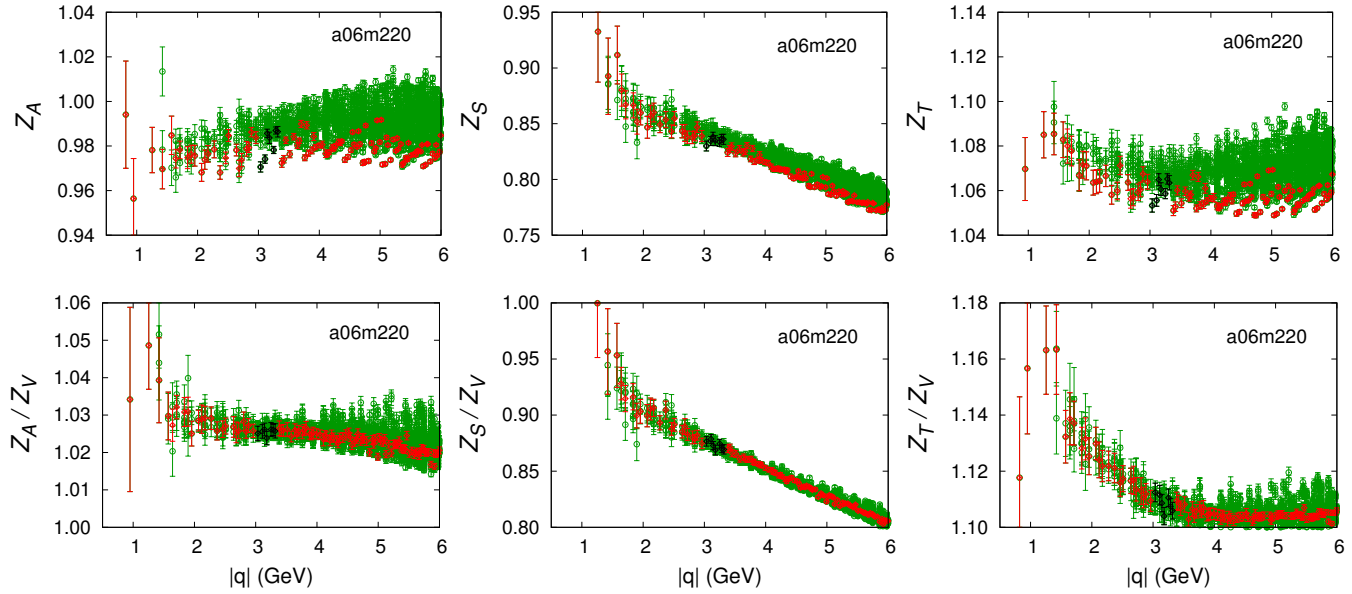

FIG. 13. Data for the renormalization constants in the $\overline{\text{MS}}$ scheme at $\mu = 2\,\text{GeV}$ as a function of the lattice momenta $|q|$ used in the RI-sMOM scheme. (Top) The data for Z_A, Z_S and Z_T for all combinations of $(p_1)_\mu$ and $(p_2)_\mu$ calculated are plotted using green circles. The subset of points that minimize $\sum_\mu (p_1)_\mu^4/((p_1)^2)^2 + \sum_\mu (p_2)_\mu^4/((p_2)^2)^2$ for each q^2 are shown using red diamonds. The value and error using method B discussed in the text is given by the average and variance of the points shown in black over the range 9.2–11.2 GeV^2. (Bottom) The data for the ratios Z_A/Z_V, Z_S/Z_V and Z_T/Z_V using the same symbols.

ID	Z_A	Z_S	Z_T	Z_V	Z_A/Z_V	Z_S/Z_V	Z_T/Z_V
a12	0.95(3)	0.90(4)	0.94(4)	0.91(2)	1.045(09)	0.986(09)	1.034(34)
a09	0.95(4)	0.88(2)	0.98(4)	0.92(2)	1.034(11)	0.955(49)	1.063(29)
a06	0.97(3)	0.86(3)	1.04(3)	0.95(1)	1.025(09)	0.908(40)	1.100(25)

TABLE X. The final mass-independent renormalization constants Z_A, Z_S, Z_T, Z_V and the ratios Z_A/Z_V, Z_S/Z_V and Z_T/Z_V in the $\overline{\text{MS}}$ scheme at 2 GeV at the three values of the lattice spacings used in our analysis. The central value is the average of estimates from the two methods and at the two pion masses given in Table IX and the errors are taken to be half the spread.

the analysis is simplest if one can hold two of the three variables constant to study the variation with the third. Our nine data points do not allow such a study. For example, estimates at the three different volume points, $a12m220S$, $a12m220$ and $a12m220L$, at fixed M_π and a are consistent within errors for all the three charges. In fact, the spread in the data in most cases is small enough that they can be fit with a linear Ansatz in each variable. Our goal, given the limited number of data points and the small variations in each of the three variables, is to make a simultaneous fit keeping the minimum number of parameters corresponding to the leading terms in the chiral expansion.

Keeping only the leading corrections in a and $M_\pi L$, we have studied the following Ansatz motivated by chiral perturbation theory [36–42]:

$$g_{A,T}(a, M_\pi, L) = c_1 + c_2 a + c_3 M_\pi^2 + c_3^{\log} M_\pi^2 \ln(\frac{M_\pi}{M_\rho})^2 + c_4 M_\pi^2 \frac{e^{-M_\pi L}}{X(M_\pi L)}\,. \quad (11)$$

$$g_S(a, M_\pi, L) = c_1 + c_2 a + c_3' M_\pi + c_3 M_\pi^2 + c_3^{\log} M_\pi^2 \ln(\frac{M_\pi}{M_\rho})^2 + c_4' M_\pi \frac{e^{-M_\pi L}}{Y(M_\pi L)}\,, \quad (12)$$

where M_ρ is the chiral renormalization scale. Note that the leading discretization errors are linear in a for our clover-on-HISQ formalism with unimproved operators, and the leading chiral correction to g_S^{u-d} starts at $O(M_\pi)$ [36]. The finite-volume correction, in general, consists of a number of terms, each with different powers of $M_\pi L$ in the denominator and depend on several low-energy constants (LEC) [39]. These powers of $M_\pi L$ are symbolically represented by $X(M_\pi L)$ and $Y(M_\pi L)$. Since the variation of these factors is small compared to the exponential over the range of $M_\pi L$ investigated, we

ID	g_A^u	g_A^d	g_A^{u-d}	g_S^u	g_S^d	g_S^{u-d}	g_T^u	g_T^d	g_T^{u-d}
a12m310	0.923(25)	-0.326(14)	1.248(26)	3.43(20)	2.61(15)	0.82(10)	0.867(25)	−0.218(12)	1.084(31)
a12m310*	0.932(9)	-0.320(5)	1.252(9)	3.31(6)	2.40(4)	0.91(4)	0.873(9)	−0.215(4)	1.087(10)
a12m220S	0.969(37)	-0.313(21)	1.283(39)	4.49(52)	3.45(37)	1.03(32)	0.858(41)	−0.208(21)	1.067(46)
a12m220	0.942(29)	-0.332(15)	1.273(30)	3.87(27)	3.21(21)	0.67(18)	0.885(26)	−0.218(16)	1.105(32)
a12m220L	1.015(75)	-0.322(22)	1.337(83)	4.74(72)	3.67(63)	1.10(17)	0.855(24)	−0.189(18)	1.043(29)
a12m220L*	0.949(11)	-0.332(6)	1.279(12)	4.10(18)	3.27(14)	0.83(6)	0.847(16)	−0.209(7)	1.056(19)
a09m310	0.949(24)	-0.312(15)	1.262(30)	3.78(30)	2.84(24)	0.94(10)	0.821(25)	−0.200(11)	1.021(31)
a09m220	0.928(23)	-0.343(16)	1.272(30)	4.16(25)	3.29(19)	0.88(13)	0.815(21)	−0.213(9)	1.029(22)
a09m130	0.864(42)	-0.314(25)	1.177(44)	5.01(58)	4.28(37)	0.73(37)	0.764(46)	−0.215(21)	0.980(45)
a09m130*	0.909(17)	-0.345(15)	1.255(24)	5.49(35)	4.51(31)	0.99(11)	0.778(23)	−0.189(10)	0.967(28)
a06m310	0.873(23)	-0.299(13)	1.172(24)	4.31(18)	3.03(11)	1.28(11)	0.764(22)	−0.187(10)	0.951(24)
a06m310*	0.895(14)	-0.317(8)	1.212(14)	4.12(11)	2.94(7)	1.18(5)	0.782(10)	−0.188(4)	0.972(12)
a06m220	0.904(48)	-0.328(25)	1.234(51)	3.63(40)	2.99(20)	0.64(29)	0.749(47)	−0.240(18)	0.990(48)
a06m220*	0.907(16)	-0.326(9)	1.234(17)	4.24(9)	3.20(5)	1.04(6)	0.792(9)	−0.192(4)	0.984(10)

TABLE XI. Estimates of the bare connected charges using the fit ranges defined under Case 3 in Table V. The isovector charges $g_\Gamma^{u-d} = \langle 0|\mathcal{O}_\Gamma|0\rangle$ are the same as Case 3 in Tables VI, VII and VIII. Ensembles marked with an asterisk denote results obtained with the AMA method.

ID	g_A^u	g_A^d	g_A^{u-d}	g_S^u	g_S^d	g_S^{u-d}	g_T^u	g_T^d	g_T^{u-d}	g_T^{u+d}
a12m310	0.903(26)	−0.319(14)	1.221(28)	3.16(18)	2.41(14)	0.757(92)	0.839(37)	−0.211(13)	1.050(45)	0.628(32)
a12m310*	0.914(11)	−0.3145(55)	1.229(14)	3.066(62)	2.226(39)	0.840(36)	0.848(29)	−0.2088(80)	1.055(36)	0.640(23)
a12m220S	0.960(38)	−0.310(22)	1.270(42)	4.19(48)	3.23(34)	0.96(30)	0.840(49)	−0.204(22)	1.046(56)	0.637(50)
a12m220	0.917(30)	−0.323(16)	1.240(32)	3.56(25)	2.95(20)	0.62(16)	0.853(38)	−0.210(17)	1.064(47)	0.641(35)
a12m220L	0.975(48)	−0.309(19)	1.284(46)	4.29(52)	3.32(47)	1.00(13)	0.812(47)	−0.180(22)	0.992(63)	0.636(38)
a12m220L*	0.931(13)	−0.3254(69)	1.255(16)	3.79(16)	3.03(14)	0.770(54)	0.822(31)	−0.2032(95)	1.025(39)	0.618(25)
a09m310	0.926(26)	−0.304(15)	1.231(33)	3.40(32)	2.56(25)	0.844(98)	0.823(33)	−0.200(13)	1.024(42)	0.623(29)
a09m220	0.911(26)	−0.337(16)	1.249(35)	3.78(30)	2.98(23)	0.80(12)	0.823(31)	−0.215(11)	1.039(36)	0.608(29)
a09m130	0.868(44)	−0.316(26)	1.182(48)	4.65(59)	3.97(41)	0.67(34)	0.789(50)	−0.222(23)	1.012(52)	0.567(58)
a09m130*	0.891(20)	−0.338(15)	1.230(29)	4.97(41)	4.08(35)	0.90(11)	0.784(31)	−0.191(11)	0.975(38)	0.592(26)
a06m310	0.867(24)	−0.297(13)	1.165(26)	3.79(23)	2.67(15)	1.13(11)	0.814(29)	−0.199(11)	1.014(33)	0.615(28)
a06m310*	0.888(16)	−0.3144(84)	1.202(18)	3.62(19)	2.58(13)	1.038(64)	0.832(22)	−0.2005(65)	1.034(26)	0.631(18)
a06m220	0.913(50)	−0.332(27)	1.246(56)	3.25(38)	2.67(22)	0.57(26)	0.812(50)	−0.260(21)	1.073(53)	0.553(54)
a06m220*	0.888(18)	−0.3190(90)	1.208(20)	3.68(18)	2.78(13)	0.901(67)	0.832(21)	−0.2016(65)	1.034(26)	0.630(18)

TABLE XII. Results for the renormalized charges using the fit ranges defined under Case 3 in Table V. Estimates of the flavor diagonal charges include only the connected contribution. The final errors are obtained by adding in quadrature the errors in estimates of the ratios $g_\Gamma^{\rm bare}/g_V^{\rm bare}$ to the errors in the ratios of the renormalization constants, Z_Γ/Z_V given in Table X. Estimates for g_T^{u+d} neglect the disconnected contributions that were shown to be tiny in Ref. [11]. Rest is the same as in Table XI.

set $X(M_\pi L) = Y(M_\pi L) =$ constant and retain only the appropriate overall factor $M_\pi^n e^{-M_\pi L}$, common to all the terms in the finite-volume expansion, in our fit Ansatz.

The dependence of the data on the lattice spacing, pion mass and the lattice volume is small. We, therefore, investigated fits with the Ansatz given in Eqs. (11) and (12) and, in addition, a number of Ansätze with various subsets of terms. In each case, the parameters $c_3^{\rm log}$ and c_4 (or c_4') are poorly determined and consistent with zero, reflective of the small range and small variation in the data with the pion mass and the lattice volume. Also, $\chi^2_{\rm d.o.f.} < 1$ in all cases, so it does not provide a good criterion for deciding the best fit Ansatz. We, therefore, considered the Ansatz with just the leading term in each of the three variables:

$$g_{A,T}(a, M_\pi, L) = \quad c_1 + c_2 a + c_3 M_\pi^2 + c_4 M_\pi^2 e^{-M_\pi L}\,, \tag{13}$$

$$g_S(a, M_\pi, L) = \quad c_1 + c_2 a + c_3' M_\pi + c_4' M_\pi e^{-M_\pi L}\,. \tag{14}$$

Using these Ansätze, the 9-point fits (9-pt) to the data for the isovector charges, renormalized using $g_\Gamma^{\rm bare}/g_V^{\rm bare} \times Z_\Gamma/Z_V$, are shown in fig. 14. The fits to g_A^{u-d} and g_S^{u-d} show a sizeable variation with a. We show the same 9-point fit in Fig. 15 using the renormalised charges obtained using $Z_\Gamma \times g_\Gamma$ and find that the variation of g_A^{u-d} with a is smaller. The systematics in the two ways of obtaining the renormalized charges are different but removed by the extrapolation to the continuum limit as suggested by the agreement between the results

ID	g_A^{u-d}	g_S^{u-d}	g_T^{u-d}	$g_V^{\mathrm{bare},u-d}$	$Z_V g_V^{u-d}$
a12m310	1.185(45)	0.738(97)	1.019(52)	1.068(10)	0.972(23)
a12m310*	1.189(39)	0.817(50)	1.022(44)	1.065(4)	0.969(22)
a12m220S	1.219(53)	0.93(29)	1.003(61)	1.055(14)	0.960(25)
a12m220	1.209(48)	0.61(16)	1.038(54)	1.073(12)	0.977(24)
a12m220L	1.270(88)	0.99(16)	0.981(50)	1.088(36)	0.990(39)
a12m220L*	1.215(40)	0.749(62)	0.993(46)	1.065(3)	0.969(21)
a09m310	1.199(58)	0.824(90)	1.000(51)	1.060(8)	0.975(33)
a09m220	1.208(58)	0.78(11)	1.008(47)	1.053(8)	0.969(32)
a09m130	1.118(63)	0.64(33)	0.960(59)	1.029(18)	0.947(35)
a09m130*	1.192(55)	0.87(10)	0.948(47)	1.055(5)	0.971(32)
a06m310	1.137(42)	1.10(10)	0.989(38)	1.032(10)	0.980(23)
a06m310*	1.176(39)	1.017(56)	1.011(32)	1.034(4)	0.982(21)
a06m220	1.197(62)	0.55(25)	1.030(58)	1.015(21)	0.964(29)
a06m220*	1.197(41)	0.894(63)	1.024(31)	1.047(6)	0.995(22)

TABLE XIII. Estimates of the renormalized isovector charges obtained using $Z_\Gamma \times g_\Gamma^{\mathrm{bare}}$ with Z_Γ given in Table X and g_Γ^{bare} in Table XI. All estimates are obtained using the fit ranges defined under Case 3 in Table V. We also give results for the bare and renormalized g_V^{u-d} in columns five and six. Estimates in the sixth column differ from $Z_V g_V^{u-d} = 1$, predicted by the conservation of the vector charge, by 2–3%. Ensembles marked with an asterisk denote results obtained with the AMA method.

Method	g_A^{u-d}	g_S^{u-d}	g_T^{u-d}
$g_\Gamma^{\mathrm{bare}}/g_V^{\mathrm{bare}} \times Z_\Gamma/Z_V$	1.195(33)	0.97(12)	0.987(51)
χ^2/d.o.f.	0.28	0.67	0.44
$g_\Gamma^{\mathrm{bare}} \times Z_\Gamma$	1.187(69)	0.97(13)	0.990(62)
χ^2/d.o.f.	0.05	0.65	0.39

TABLE XIV. Results of the 9-point fit to the data for the isovector charges renormalized in two ways: using $g_\Gamma^{\mathrm{bare}}/g_V^{\mathrm{bare}} \times Z_\Gamma/Z_V$ with $g_V^{\mathrm{bare}} Z_V = 1$ given in Table XII and $g_\Gamma^{\mathrm{bare}} \times Z_\Gamma$ given in Table XIII.

shown in Table XIV. The errors in the ratio method, $g_\Gamma^{\mathrm{bare}}/g_V \times Z_\Gamma/Z_V$, are smaller because, as discussed in Sec. IV, some of the systematics cancel in each of the two ratios. We, therefore, use the estimates from the ratio method in all subsequent analysis.

We also show two additional fits to illustrate the dependence of the estimates of the charges on the fit Ansatz: (i) we add the chiral logarithm term to the 9-point fit and call it the 9-point log fit (9-ptL) and (ii) we remove the smallest volume point $a12m220S$ and perform an 8-point fit (8-pt) using Eqs. (13) and (14). These two fits are shown in Figs. 16 and 17, respectively. The resulting values of the fit parameters and estimates for the three isovector charges are given in Table XV. To choose between the 9-point and the 9-point with chiral logarithm fit, we used the Akaike Information Criteria (AIC) [43]. As can be seen from Table XV, the χ^2 does not decrease by 2 to justify adding an extra parameter, the chiral logarithm term. Our final estimates, given in Sec. VII are, therefore, obtained with the 9-point fit without the chiral logarithm.

We find that the smallest volume point, $a12m220S$, provides a large lever arm in the determination of the shape of the finite-volume correction, as can be seen by comparing the 9-pt (Fig. 14) versus the 8-pt (Fig. 17) fits. Nevertheless, the fits do not show a significant difference for $M_\pi L \gtrsim 4$.

To further explore the sensitivity of the data for the isovector charges $g_{A,S,T}^{u-d}$ to chiral logarithms, we make 8-point fits (neglecting the $a12m220S$ point and assuming that the finite-volume corrections can be ignored for $M_\pi L \gtrsim 4$) with and without a chiral logarithm term:

$$g_{A,T}(a, M_\pi) = c_1 + c_2 a + c_3 M_\pi^2 + c_3^{\log} M_\pi^2 \ln \frac{M_\pi^2}{M_\rho^2} \,.$$
$$g_S(a, M_\pi) = c_1 + c_2 a + c_3' M_\pi + c_3^{\log} M_\pi^2 \ln \frac{M_\pi^2}{M_\rho^2} \,. \quad (15)$$

The chiral renormalization scale is taken to be $M_\rho = 0.775$ GeV. Results for the parameters c_i are summarized in Table XVI with and without the $c_3^{\log}$ term. The parameter c_3 (or c_3') is again poorly constrained by the data since the variation in the estimates between $M_\pi = 135$ and 320 MeV is comparable to the errors in the individual points for all three charges as can be seen in Figs. 14, 16 and 17. The main effect of adding the $c_3^{\log}$ term is an adjustment with c_3: there is a large cancellation between the contributions of these two terms. Also, the errors in both c_3 and $c_3^{\log}$ are $O(1)$ in all three charges. To test whether the chiral logarithm term improves the predictive power of the fit, we again use the Akaike Information Criterion [43]. The χ^2 changes by much less than two units, indicating that adding the chiral logarithm is not justified. Also, for the scalar charge, we find little difference in the fits between using $c_3 M_\pi^2$ versus $c_3' M_\pi$ as the leading chiral term.

The bottom line is that changing the fit Ansatz from Eqs. (11) and (12) to Eqs. (13) and (14) to that given in Eq. (15) does not significantly change the estimates for the charges as can be seen by comparing the last column of Tables XV and XVI.

Our final results for the isovector charges using the 9-point fit are presented in Table XXII in Sec. VII after we revisit our error analysis and assign an additional systematic error to account for the uncertainty due to the various fit Ansatz discussed above.

To obtain the flavor-diagonal charges g_Γ^u and g_Γ^d and the isoscalar combination g_Γ^{u+d} requires calculation of the disconnected contributions. We have not carried out any new simulations to update estimates of the disconnected contributions to the tensor charges that were shown to be $O(1\%)$ of the connected contribution and consistent with zero in Ref. [11]. We, therefore, consider the connected part to be a good approximation to the full result and present updated results for g_T^u, g_T^d and g_T^{u+d} in Table XVII. The disconnected contributions to the axial and scalar charges are larger, about 0.1 and $O(1)$, re-

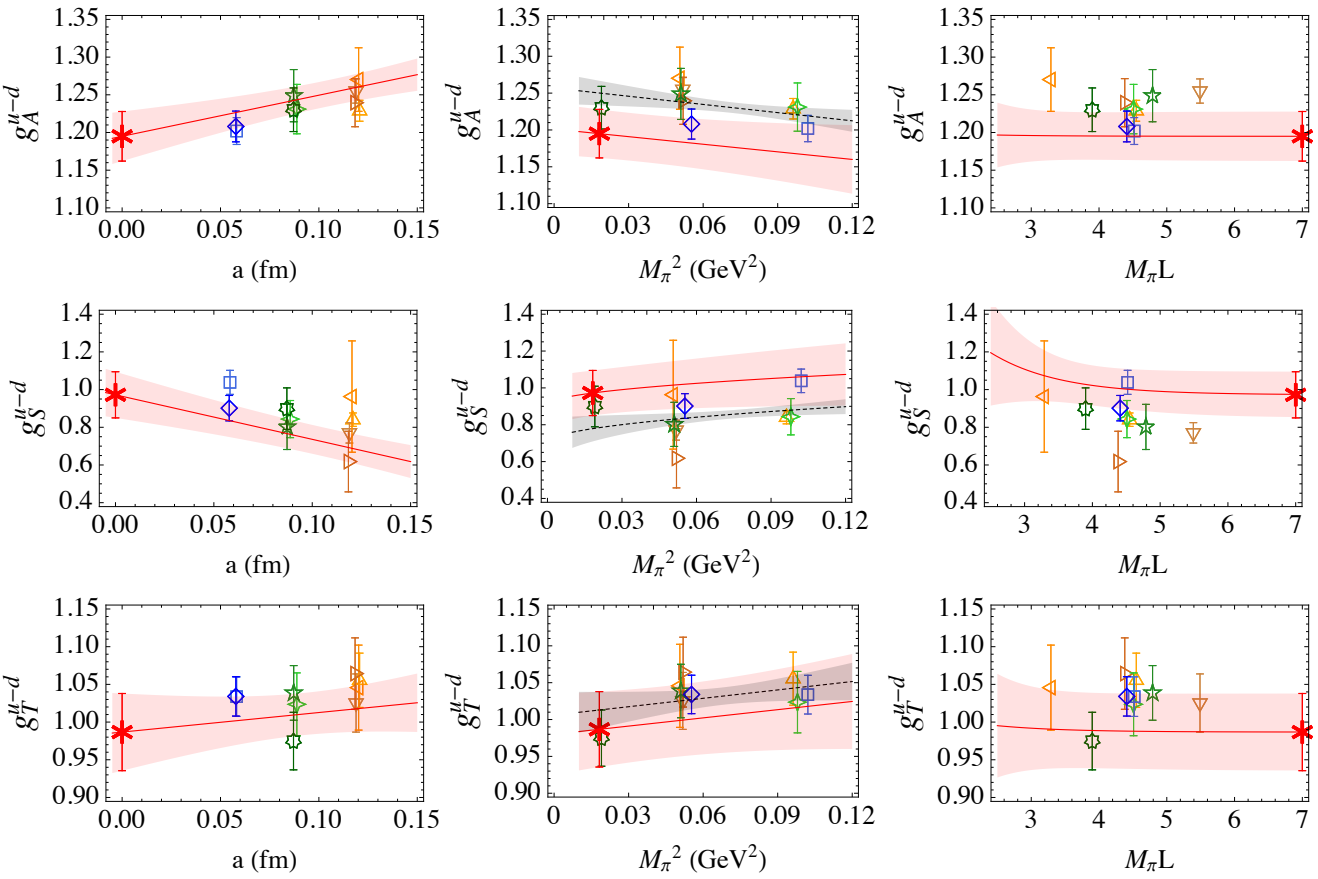

FIG. 14. The 9-point fit using Eqs. (13) and (14) to the data for the renormalized isovector charges, g_A^{u-d}, g_S^{u-d} and g_T^{u-d}, in the $\overline{\rm MS}$ scheme at 2 GeV. The result of the simultaneous extrapolation to the physical point defined by $a \to 0$, $M_\pi \to M_{\pi^0}^{\rm phys} = 135$ MeV and $L \to \infty$ are marked by a red star. The error bands in each panel show the simultaneous fit as a function of a given variable holding the other two at their physical value. The data are shown projected on to each of the three planes. The overlay in the middle figures with the dashed line within the grey band, is the fit to the data versus M_π^2 neglecting dependence on the other two variables. The symbols used for data points from the various ensembles are defined in Table I.

spectively, and we are working on a more detailed analysis of these. We, therefore, do not present results for the isoscalar combinations g_A^{u+d} and g_S^{u+d} but give only the connected contributions to the flavor-diagonal charges $g_{A,S}^{u,d}$ using the same three fits, 9-point, 9-point with log and the 8-point, in Table XVII.

We show the behavior of the connected parts of the flavor-diagonal charges $g_{A,S,T}^{u,d}$ versus the lattice spacing and the pion mass in Figs. 18, 19 and 20 using 9-point fits with $c_3^{\rm log} = 0$ in the Ansatz given in Eq. 15. The plots show that estimates of g_T^u are about four times larger than of g_T^d, and both are essentially flat with respect to the pion mass, the lattice spacing and the lattice volume. The behavior of $g_A^{u,d}$, shown in Fig. 19, is similar in magnitude and sign to that in $g_T^{u,d}$. Again, data show little dependence on the pion mass, however, there is a notable increase of g_A^u with a that carries over to g_A^{u-d} plotted in Fig. 14. The 9-point fits with the c_3' term for g_S^u and g_S^d are shown in Fig. 20. These data are much larger in magnitude and show a significant dependence on the quark mass.

The final results for the connected parts of the flavor-diagonal charges g_Γ^u and g_Γ^d from the 9-point fit are presented in Table XXIII in Sec. VII. The new estimates of $g_T^{u,d}$, needed to analyze the contribution of the EDM of the quarks to the neutron EDM, supercede the values presented in Refs. [11, 20].

VI. CONFIRMATION OF THE 2-STATE ANALYSIS

The analysis in the previous sections was predicated on the assumption that the 2-state Ansatz given in Eqs. (9) and (10) resolves the excited-state contamination in the 2- and 3-point functions. In this section, we provide further confirmation of this assumption using additional high-statistics AMA simulations on the $a06m310$ and $a06m220$ ensembles with different smearing parameters. These are listed in Table XVIII under the label AMA2.

A comparison of the excited-state contamination and

	c_1	c_2 fm^{-1}	c_3 GeV^{-2}	c_3' GeV^{-1}	$c_3^{\log}$ GeV^{-2}	c_4 GeV^{-2}	c_4' GeV^{-1}	χ^2/d.o.f.	g_Γ
g_A(9-pt)	1.201(35)	0.55(27)	−0.34(38)			1(26)		0.28	1.195(33)
g_A(9-ptL)	1.166(87)	0.53(27)	−1.1(1.8)		−0.62(1.4)	−3(26)		0.30	1.185(40)
g_A(8-pt)	1.208(35)	0.40(31)	0.19(68)			−43(53)		0.12	1.211(37)
g_S(9-pt)	0.91(15)	−2.4(0.9)		0.48(59)			20(29)	0.67	0.97(12)
g_S(9-ptL)	0.62(30)	−2.4(0.9)		13(12)	21(19)		4(32)	0.53	1.10(17)
g_S(8-pt)	0.91(15)	−2.5(1.0)		0.57(68)			14(38)	0.82	0.99(13)
g_T(9-pt)	0.980(55)	0.26(46)	0.37(57)			6(39)		0.44	0.987(51)
g_T(9-ptL)	0.85(12)	0.20(47)	−2.7(2.5)		−2.4(1.9)	−9(39)		0.15	0.951(58)
g_T(8-pt)	0.986(61)	0.19(54)	0.6(1.1)			−20(10)		0.54	0.997(67)

TABLE XV. Values of the fit parameters defined in Eqs. (11) and (12). The 9-point fit to the isovector charges includes terms with c_1, c_2, c_3 (or c_3' for g_S^{u-d}) and c_4 (or c_4' for g_S^{u-d}). The 9-ptL fit includes the chiral logarithm term $c_3^{\log}$. The 8-pt fit uses the same Ansatz as the 9-pt fit but neglects the $a12m220S$ data point. The last column gives the value of the charge at the physical point.

	c_1	c_2 fm^{-1}	c_3 GeV^{-2}	c_3' GeV^{-1}	$c_3^{\log}$ GeV^{-2}	χ^2/d.o.f.	g_Γ
g_A^{u-d}	1.171(85)	0.51(27)	−1.0(1.7)		−0.5(1.4)	0.24	1.188(38)
g_A^{u-d}	1.201(35)	0.52(27)	−0.31(28)			0.23	1.195(32)
g_S^{u-d}	0.60(28)	−2.46(88)		14(10)	22(17)	0.41	1.12(13)
g_S^{u-d}	0.91(15)	−2.61(87)		0.75(47)		0.68	1.01(11)
g_T^{u-d}	0.85(12)	0.20(48)	−2.5(2.4)		−2.4(1.9)	0.16	0.955(58)
g_T^{u-d}	0.982(55)	0.23(48)	0.43(44)			0.43	0.990(50)

TABLE XVI. Values of the fit parameters for the 8-point fit defined in Eq. (15) are given in the top row for each charge. The bottom row uses the same fit Ansatz but with $c_3^{\log}$ set to 0. The last column gives the value of the charge at the physical point.

ID	g_A^u	g_A^d	g_A^{u-d}	g_S^u	g_S^d	g_S^{u-d}	g_T^u	g_T^d	g_T^{u-d}	g_T^{u+d}
9-pt	0.856(27)	−0.335(15)	1.195(33)	4.94(30)	4.00(22)	0.97(12)	0.792(42)	−0.194(14)	0.987(51)	0.598(36)
9-ptL	0.841(31)	−0.342(20)	1.185(40)	5.59(48)	4.59(39)	1.10(17)	0.766(48)	−0.183(17)	0.951(58)	0.579(41)
8-pt	0.877(31)	−0.333(16)	1.211(37)	5.09(33)	4.13(25)	0.99(13)	0.796(55)	−0.197(17)	0.997(67)	0.599(46)

TABLE XVII. Estimates of the connected parts of the flavor diagonal charges and g_T^{u+d} with the three different fits described in Table (XV). The estimates for the isovector charges $g_{A,S,T}^{u-d}$ are reproduced from Table (XV) to make comparison easier.

Ensemble ID	Type	σ	$N_{\rm GS}$	$t_{\rm sep}/a$	$N_{\rm conf}$	$N_{\rm meas}^{\rm HP}$	$N_{\rm meas}^{\rm AMA}$
a06m310	AMA	6.5	70	$\{16, 20, 22, 24\}$	1000	4000	64,000
a06m310	AMA2	12	250	$\{18, 20, 22, 24\}$	500	2000	64,000
a06m220	AMA	5.5	70	$\{16, 20, 22, 24\}$	650	2600	41,600
a06m220	AMA2	11	230	$\{18, 20, 22, 24\}$	650	2600	41,600

TABLE XVIII. The smearing parameters, the values of $t_{\rm sep}$ and the statistics used in the two AMA simulations on the $a06m310$ and $a06m220$ ensembles to test the efficacy of the 2-state fit in controlling excited-state contamination. The second set of AMA measurements with the larger smearing size are labeled AMA2. The number of HP measurements used to correct the bias in the AMA method are listed under $N_{\rm meas}^{\rm HP}$.

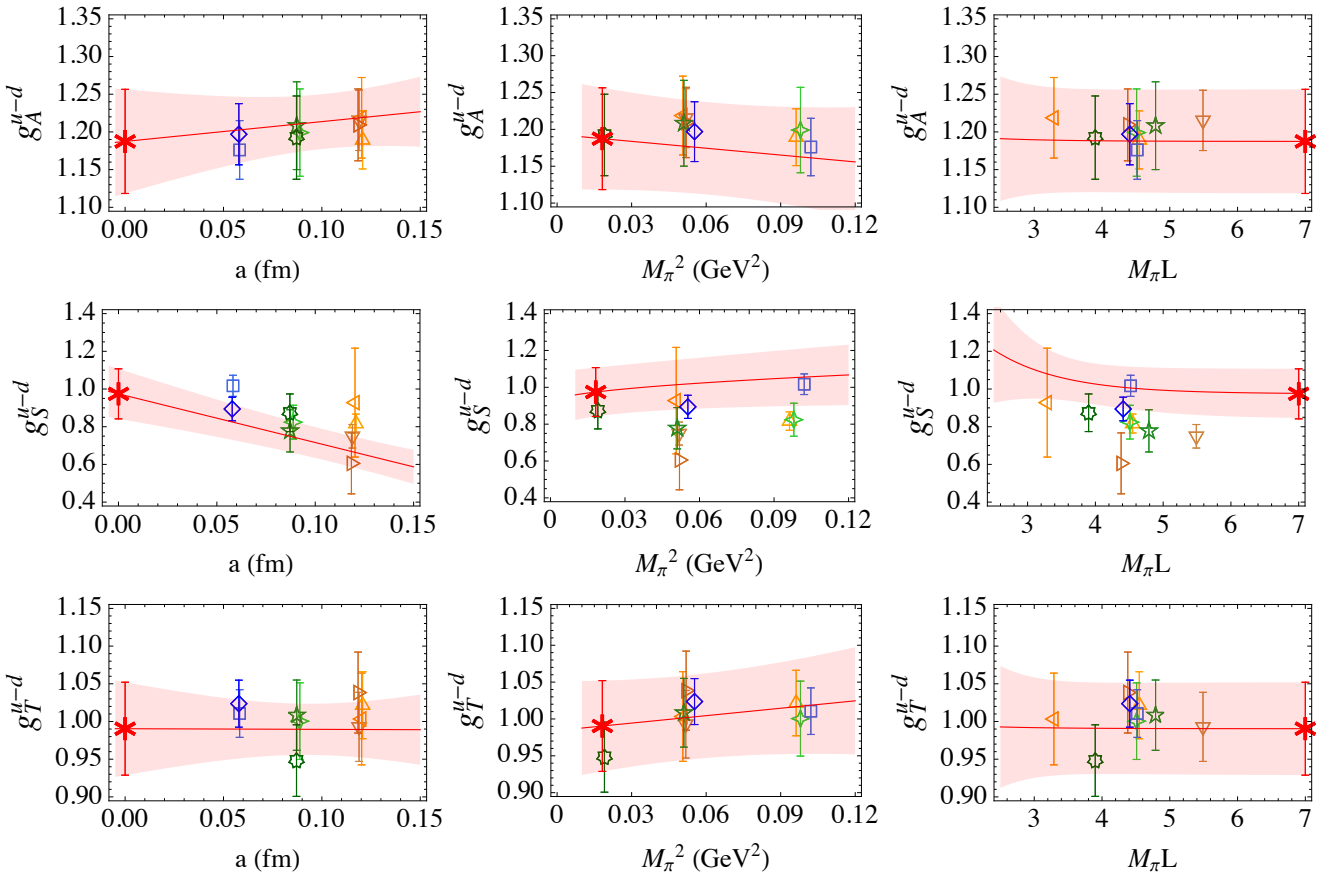

FIG. 15. The 9-point fit using Eqs. (13) and (14) to the data for the renormalized isovector charges obtained using $Z_A g_A^{\text{bare},u-d}$, $Z_S g_S^{\text{bare},u-d}$ and $Z_T g_T^{\text{bare},u-d}$. The rest is the same as in Fig. 14.

ID	Type	Fit Range	aM_0	aM_1	$\mathcal{A}_0^2 \times 10^{11}$	$\mathcal{A}_1^2 \times 10^{11}$	$\mathcal{A}_1^2/\mathcal{A}_0^2$
a06m310	AMA	8—30	0.3268(23)	0.56(3)	0.58(3)	0.95(10)	1.66(11)
a06m310	AMA2	5—25	0.3282(17)	0.68(5)	$1.32(4)\times10^{-11}$	$1.5(2)\times10^{-11}$	1.16(14)
a06m220	AMA	8—30	0.3069(18)	0.63(3)	11.3(4)	39.2(5.0)	3.47(35)
a06m220	AMA2	4—30	0.3037(13)	0.64(2)	$2.66(6)\times10^{-9}$	$3.8(2)\times10^{-9}$	1.41(4)

TABLE XIX. Comparison of the masses aM_0 and, aM_1 and the amplitudes $\mathcal{A}_0$ and $\mathcal{A}_1$ obtained using the AMA method with different smearing parameters on the $a06m310$ and $a06m220$ ensembles. The AMA estimates are the same as in Table III. The smearing parameters and the statistics for the two runs are given in Table XVIII.

		Axial			Scalar			Tensor		
ID	Type	$\langle 0\|\mathcal{O}_\Gamma\|0\rangle$	$\langle 0\|\mathcal{O}_\Gamma\|1\rangle$	$\langle 1\|\mathcal{O}_\Gamma\|1\rangle$	$\langle 0\|\mathcal{O}_\Gamma\|0\rangle$	$\langle 0\|\mathcal{O}_\Gamma\|1\rangle$	$\langle 1\|\mathcal{O}_\Gamma\|1\rangle$	$\langle 0\|\mathcal{O}_\Gamma\|0\rangle$	$\langle 0\|\mathcal{O}_\Gamma\|1\rangle$	$\langle 1\|\mathcal{O}_\Gamma\|1\rangle$
a06m310	AMA	1.212(14)	−0.060(17)	−1.2(1.4)	1.18(5)	−0.40(4)	−0.5(1.0)	0.972(12)	0.128(10)	0.50(22)
a06m310	AMA2	1.210(13)	−0.042(26)	−2.6(6.2)	1.17(7)	−0.43(8)	−9(25)	0.987(12)	0.219(18)	0.6(4.0)
a06m220	AMA	1.234(17)	−0.121(18)	−6.3(3.9)	1.04(6)	−0.30(4)	−0.7(2.6)	0.984(10)	0.103(8)	−0.53(59)
a06m220	AMA2	1.222(13)	−0.063(21)	−4.2(3.9)	0.79(8)	−0.17(7)	38(25)	0.969(11)	0.203(16)	1.6(2.4)

TABLE XX. Comparison of results with the two different smearing parameters defined in Table XVIII for the three unrenormalized matrix elements $\langle 0|\mathcal{O}_\Gamma|0\rangle$, $\langle 1|\mathcal{O}_\Gamma|0\rangle$ and $\langle 1|\mathcal{O}_\Gamma|1\rangle$ for the isovector axial, scalar and tensor operators using the 2-state Ansatz given in Eqs (9) and (10). The fit ranges for the 3-point functions are defined under Case 3 in Table V. The AMA estimates are the same as given in Tables VI, VII and VIII.

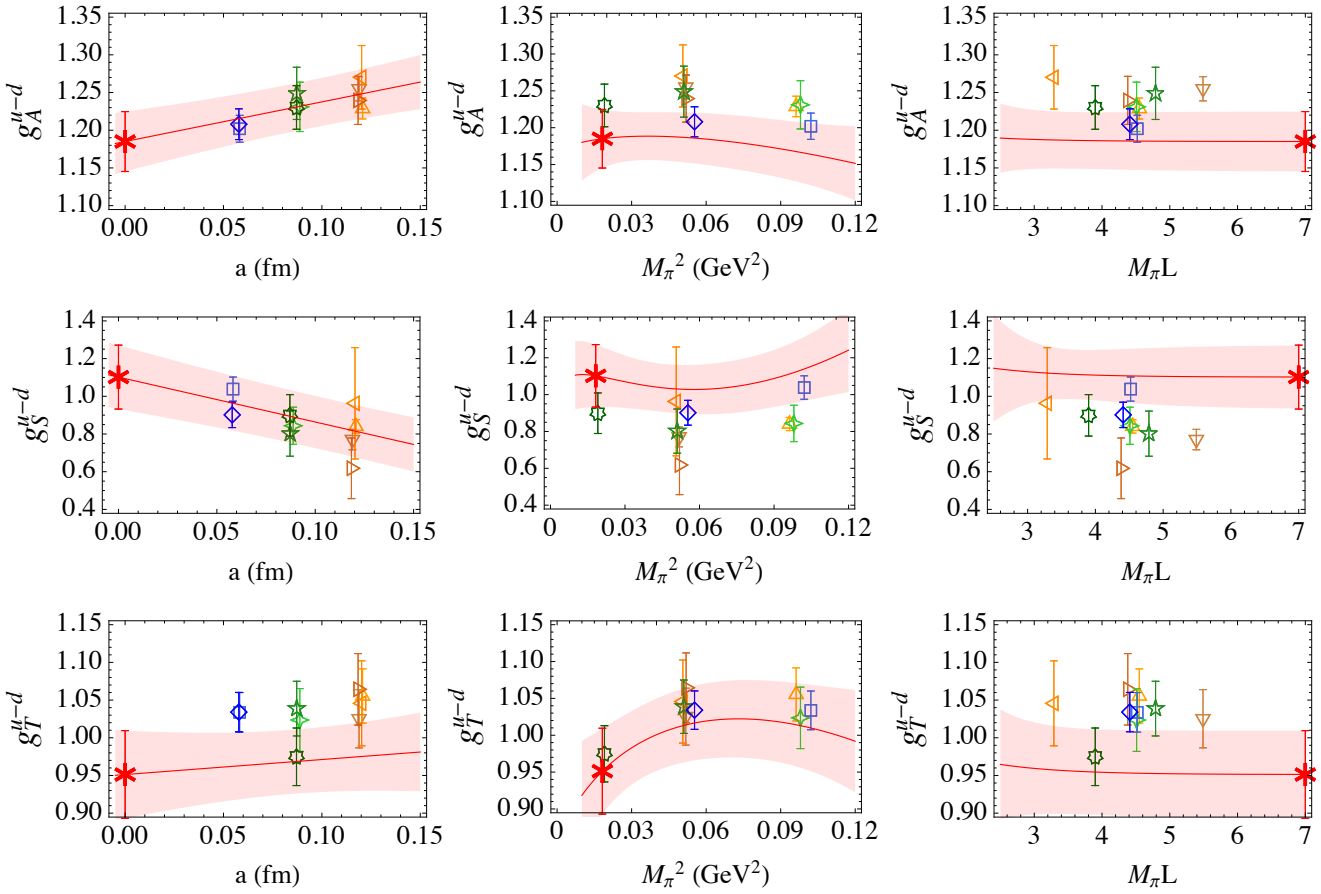

FIG. 16. The 9-point extrapolation of the isovector charges including the the chiral logarithm term, defined in Eqs. (11) and (12), in the fit Ansatz. The rest is the same as in Fig. 14.

fits using Eqs. (9) and (10) to the 3-point functions data is shown in Figs. 22 and 23, and the results for the three matrix elements $\langle 0|\mathcal{O}_\Gamma|0\rangle$, $\langle 1|\mathcal{O}_\Gamma|0\rangle$ and $\langle 1|\mathcal{O}_\Gamma|1\rangle$ are given in Table XX. A summary of the notable features is:

- Increasing the smearing size σ reduces the ratio $\mathcal{A}_1/\mathcal{A}_0$ and the relative contribution of the excited-states. Estimates of M_0 and the isovector charges g_A^{u-d}, g_T^{u-d} and g_V^{u-d} (given by $\langle 0|\mathcal{O}_\Gamma|0\rangle$) with the two different smearing sizes agree within 1σ. The one exception is g_S^{u-d} from the $a06m220$ ensemble.

- The excited-state contamination in g_A^{u-d} is significantly reduced with the larger smearing size from 15% to 5%. This can be seen by comparing the data at the central values of τ. The 2-state fit to both sets of data gives consistent estimates of the $t_{\rm sep} \to \infty$ value.

- The excited-state effect in g_T^{u-d} at the central values of τ is less than 5% in all cases as shown in Figs. 10, 22 and 23. Comparing the data with the two smearing sizes, we find that the 2-state fit gives consistent and stable estimates of the $t_{\rm sep} \to \infty$ value for both $a06m310$ and $a06m220$ ensembles.

- The data for g_S^{u-d} at different $t_{\rm sep}$ with the larger smearing size overlap and are not well resolved as shown in Figs. 22 and 23. The pattern of variation of the $a06m220$ AMA2 data versus $t_{\rm sep}$ is opposite to that seen in the other three ensembles listed in Table XVIII. The 2-state fit takes this into account with an unreasonably large value of $\langle 1|\mathcal{O}_\Gamma|1\rangle$ and with the opposite sign. As a result, the two estimates of g_S^{u-d} from the $a06m220$ ensemble differ by roughly 3σ. We consider this inverted pattern of the $\langle 1|\mathcal{O}_\Gamma|1\rangle$ contribution in the AMA2 data to be a statistical fluctuation and regard the AMA estimate to be more reliable.

- Estimates of $\langle 0|\mathcal{O}_\Gamma|1\rangle$ agree in sign and roughly in magnitude for all the charges.

- Estimates of $\langle 1|\mathcal{O}_\Gamma|1\rangle$ for the three charges are poorly determined with either smearing size.

- The differences in M_1, $\langle 0|\mathcal{O}_\Gamma|1\rangle$ and $\langle 1|\mathcal{O}_\Gamma|1\rangle$ are large in some cases. These differences reflect the fact that the 2-state fit lumps the contribution of all the excited states into one "effective" excited state, and their contributions vary with the smearing size

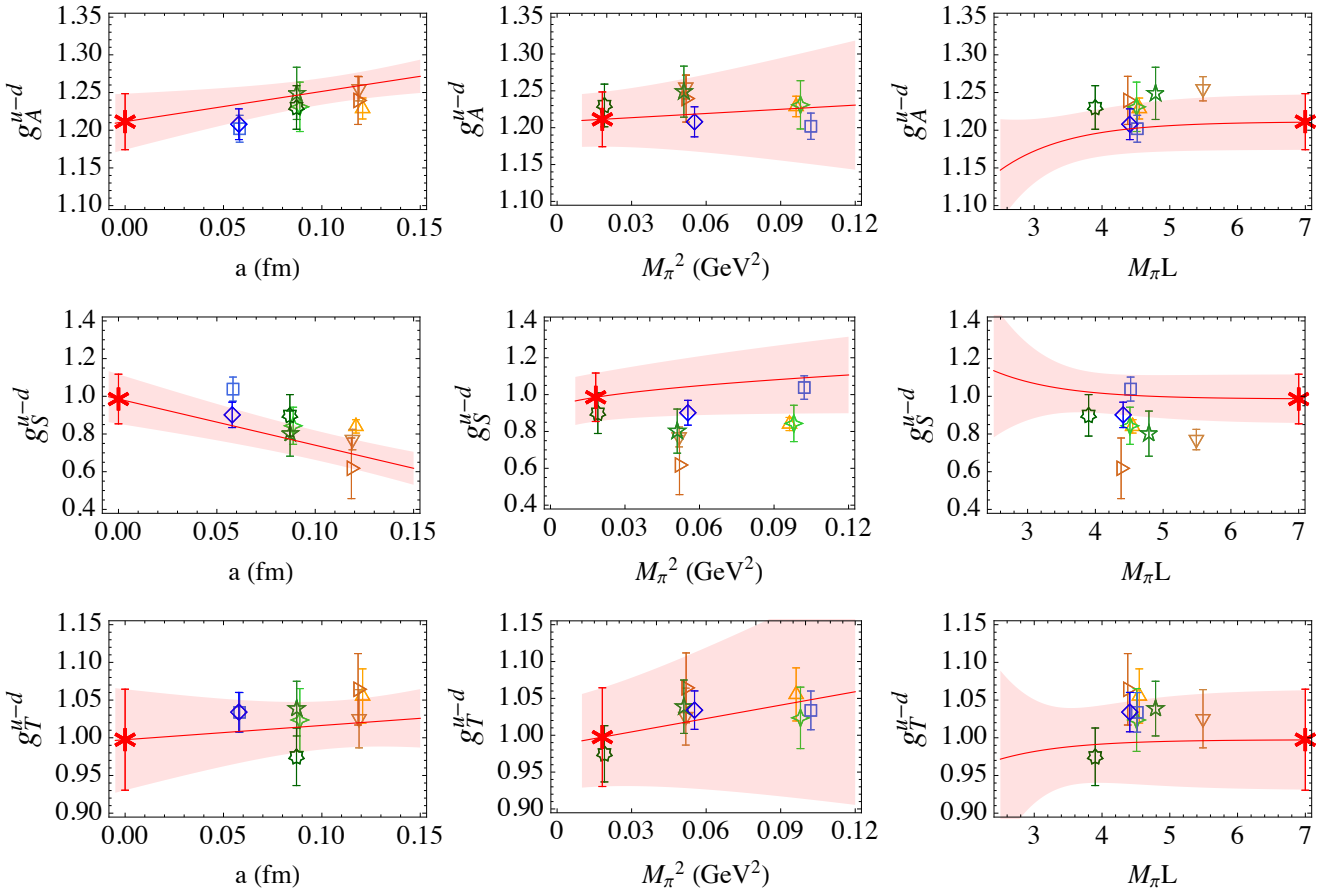

FIG. 17. The 8-point fit to the isovector charges neglecting the $a12m220S$ point. The rest is the same as in Fig. 14.

and the fit ranges. Much higher-statistics data with better interpolating operators that enable a three-state fit will be needed to obtain reliable estimates of these first excited-state parameters.

- The errors in the two matrix elements $\langle 0|\mathcal{O}_\Gamma|1\rangle$ and $\langle 1|\mathcal{O}_\Gamma|1\rangle$ given by the 2-state fit are larger in the AMA2 analysis even though the total number of measurements in the two cases are the same. With reduced excited-state contamination, the data at different $t_{\rm sep}$ overlap and the 2-state fit becomes less stable with respect to values of $t_{\rm sep}$ used in the fit. Consequently, higher statistics are needed to provide reliable $t_{\rm sep} \to \infty$ estimates.

The bottom line is that these two additional simulations validate the results based on 2-state fits to data at multiple values of $t_{\rm sep}$ presented in Sec. V. They also show that the large excited-state contamination in g_A^{u-d} and g_S^{u-d} on the $a = 0.06$ fm lattices with smearing parameter $\sigma \approx 6$ is significantly reduced with $\sigma \approx 11$. On the other hand, estimates at different $t_{\rm sep}$ start to overlap with reduced excited-state contamination, and the 2-state fit becomes less stable. This is most obvious in the g_S^{u-d} data on the $a06m220$ ensemble. In retrospect, a more effective compromise balancing the two effects would have been achieved with an intermediate value for the smearing parameter, $\sigma = 9$ (≈ 0.55 fm in physical units), on the $a = 0.06$ fm ensembles.

VII. ASSESSING THE ESTIMATION OF ERRORS

The estimation of errors in our analysis has four main components:

- Statistical and excited-state contamination (SESC): Errors from these two sources are estimated together in the combined 2-state fit.

- Uncertainty in the determination of the renormalization constants Z_Γ: The Z's are estimated as a function of q^2 using the RI-sMOM scheme on the lattice and then converted to $\overline{\rm MS}$ scheme at 2 GeV using perturbation theory. As discussed in Sec. IV, there is significant spread in the data due to breaking of rotational symmetry on the lattice. Second, the 2-loop series for the matching factor for g_T^{u-d} does not show a convergent behavior. Third, the data for the four charges do not uniformly show a large enough interval, $\eta\Lambda_{\rm QCD} \ll q \ll \xi\pi/a$, over

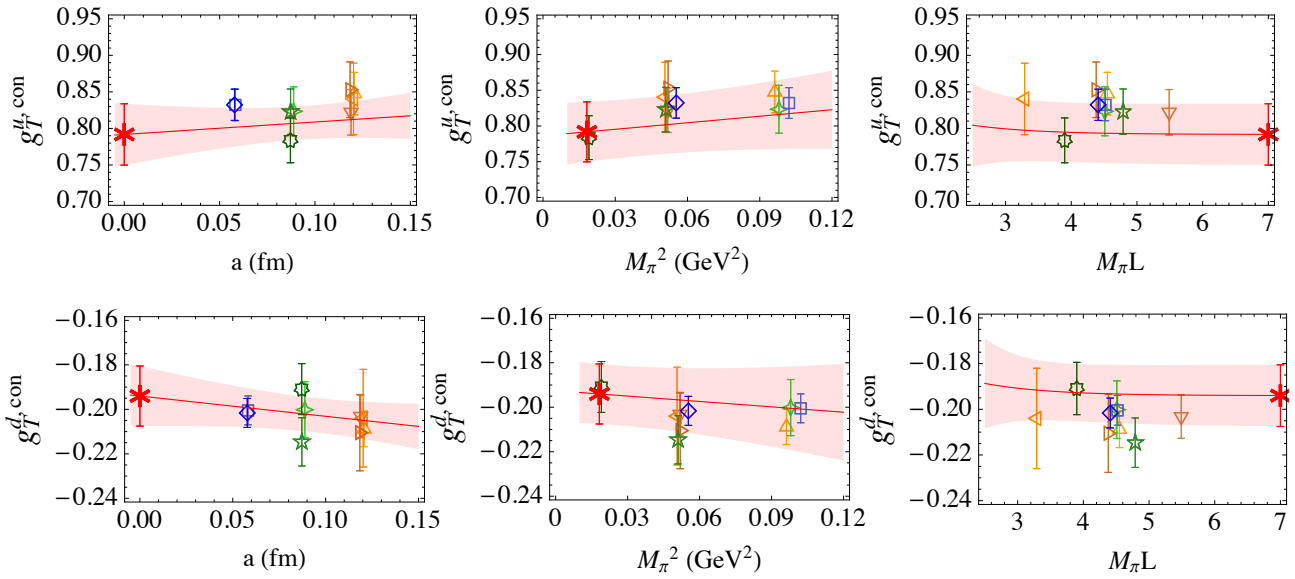

FIG. 18. 9-point simultaneous fits to the connected contributions to g_T^u and g_T^d versus a, M_π^2 and $M_\pi L$ using Eq. (13). The dependence on the three variables M_π^2, a or $M_\pi L$ is small. The data symbols are defined in Table I.

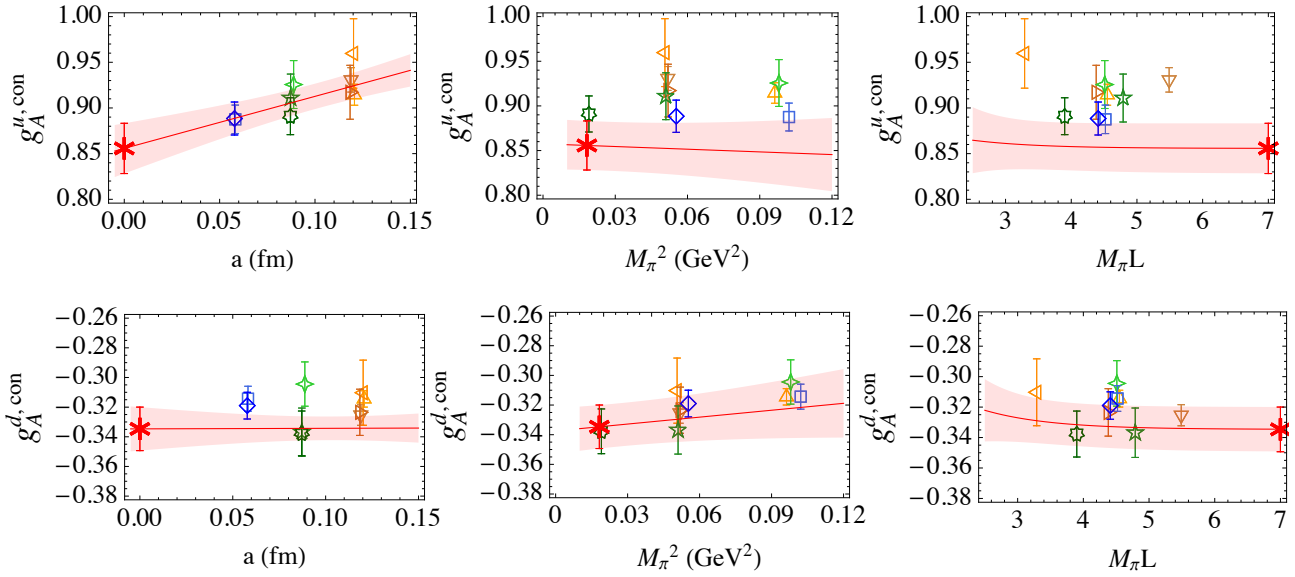

FIG. 19. 9-point simultaneous fits to the connected contributions to g_A^u and g_A^d versus a, M_π^2 and $M_\pi L$ using Eq. (13). The data for g_A^u show a notable dependence on the lattice spacing a. The rest of the panels show little dependence on either M_π^2 or $M_\pi L$. The data symbols are defined in Table I.

which they are independent of q^2, so we are not able to extract a unique estimate of Z_Γ. The two methods we use give significantly different estimates. We use this difference, which is larger than the individual statistical uncertainty, to assign the error. These error estimates are added in quadrature to those in the bare charges obtained from the 2-state fit to get the total error in the renormalized charges on each ensemble.

- Discretization errors due to nonzero lattice spacing a, finite-volume effects characterized by $M_\pi L$ and uncertainty in the chiral behavior: The errors due to these three systematics are obtained using a simultaneous fit. The Ansatz used for the final results, keeping the lowest-order corrections in each variable, is given in Eqs. 13 and 14.

- Uncertainty due to the number of terms retained in the combined fit Ansatz as discussed in Sec. V.

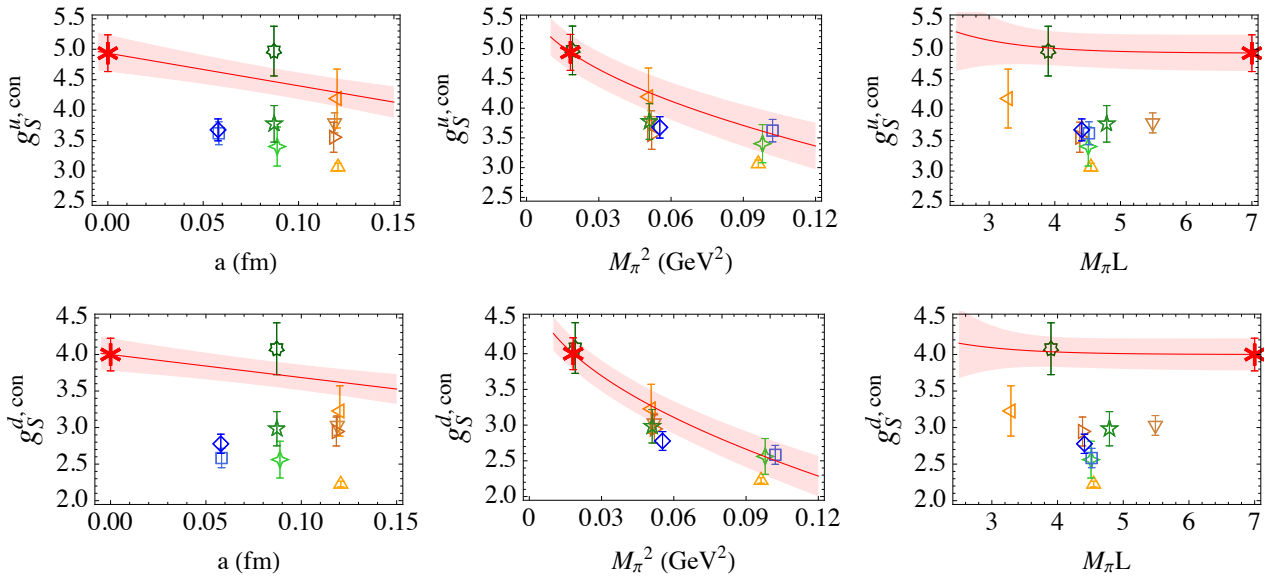

FIG. 20. 9-point simultaneous fits to the connected contributions to g_S^u and g_S^d versus a, M_π^2 and $M_\pi L$ using Eq. (14) plus a $c_3 M_\pi^2$ term. The data show significant dependence on M_π^2 and are much larger in magnitude compared to $g_{A,T}^u$ and $g_{A,T}^d$. The data symbols are defined in Table I.

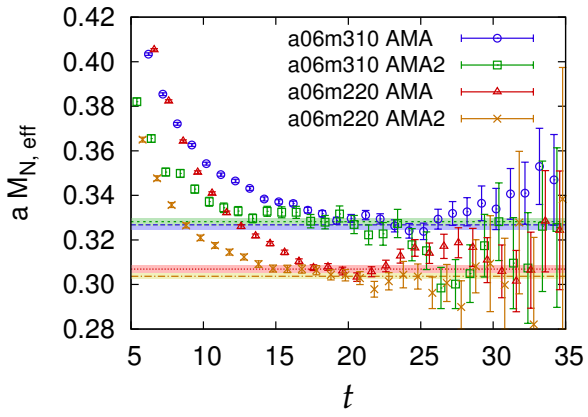

FIG. 21. Comparison of the nucleon effective-mass obtained on the $a06m310$ and $a06m220$ ensembles with different smearing sizes. The lattice parameters are summarized in Table XVIII.

A recapitulation of the important features observed in the data for the isovector charges is:

- Estimates of the isovector axial charge, g_A^{u-d}, converge from below with respect to excited-state contamination on all the ensembles. The data plotted in Fig. 14 show no significant dependence on the pion mass or the lattice volume. The largest variation is the increase with the lattice spacing and the size of the slope is dictated by the smaller estimates on the $a = 0.06$ fm ensembles. Also, as discussed in Sec. V, even though this slope is different in the fits to renormalized charges calculated in the two ways, the extrapolated results are consistent. Overall, the spread in the estimates under changes in the fit Ansatz is small, about 0.03.

- The isovector scalar charge, g_S^{u-d}, also converges from below with respect to excited-state contamination. The data show a decrease with the lattice spacing but no significant variation with the pion mass. Our error estimate accounts for (i) the large excited-state contamination on the two finest ensembles, $a06m310$ and $a06m220$; (ii) the uncertainty in the determination of the renormalization constant Z_S; and (iii) the larger, by a factor of 3–5, statistical errors compared to those in g_A^{u-d} and g_T^{u-d} on the various ensembles as summarized in Table XI. The fits capture the variation of $g_S^{u-d}(a, M_\pi, M_\pi L)$ with respect to both the lattice spacing a and the pion mass M_π as shown in Figs. 14 and 17. The largest sensitivity to the fit Ansatz comes from adding a chiral logarithm term, which tends to increase the estimate by about 0.12 as shown in Table XV. However, as shown in Fig. 20, keeping just the leading polynomial correction, $O(M_\pi)$ gives very good fits to the data, and the AIC indicates that adding the chiral logarithm term does not improve the fits significantly. Nevertheless, we will take half the change, 0.06, as an estimate of the systematic error due to the choice of the fit Ansatz.

- Our analysis of the isovector tensor charge, g_T^{u-d}, shows that (i) estimates converge from above for each ensemble and the fit using the 2-state Ansatz given in Eqs. (9) and (10) accounts for the excited-

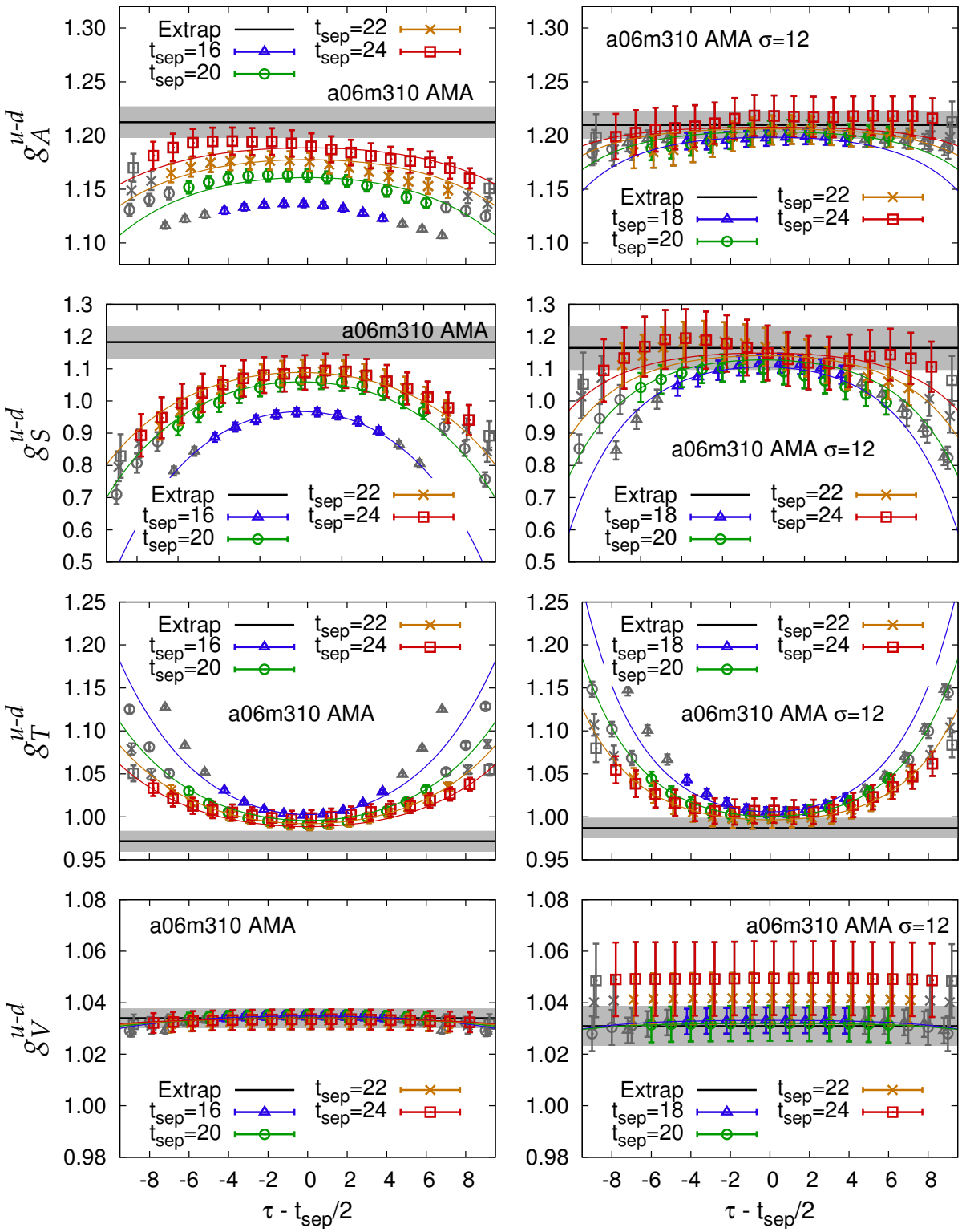

FIG. 22. Comparison of the excited-state contamination in the extraction of unrenormalized isovector charges $g^{u-d}_{A,S,T,V}$ from the $a06m310$ ensemble. The plots on the left are with smearing parameters $\{\sigma = 6.5, N_{\rm GS} = 70\}$ and on the right with $\{\sigma = 12, N_{\rm GS} = 250\}$. Both calculations were done using the AMA method with parameters summarized in Table XVIII.

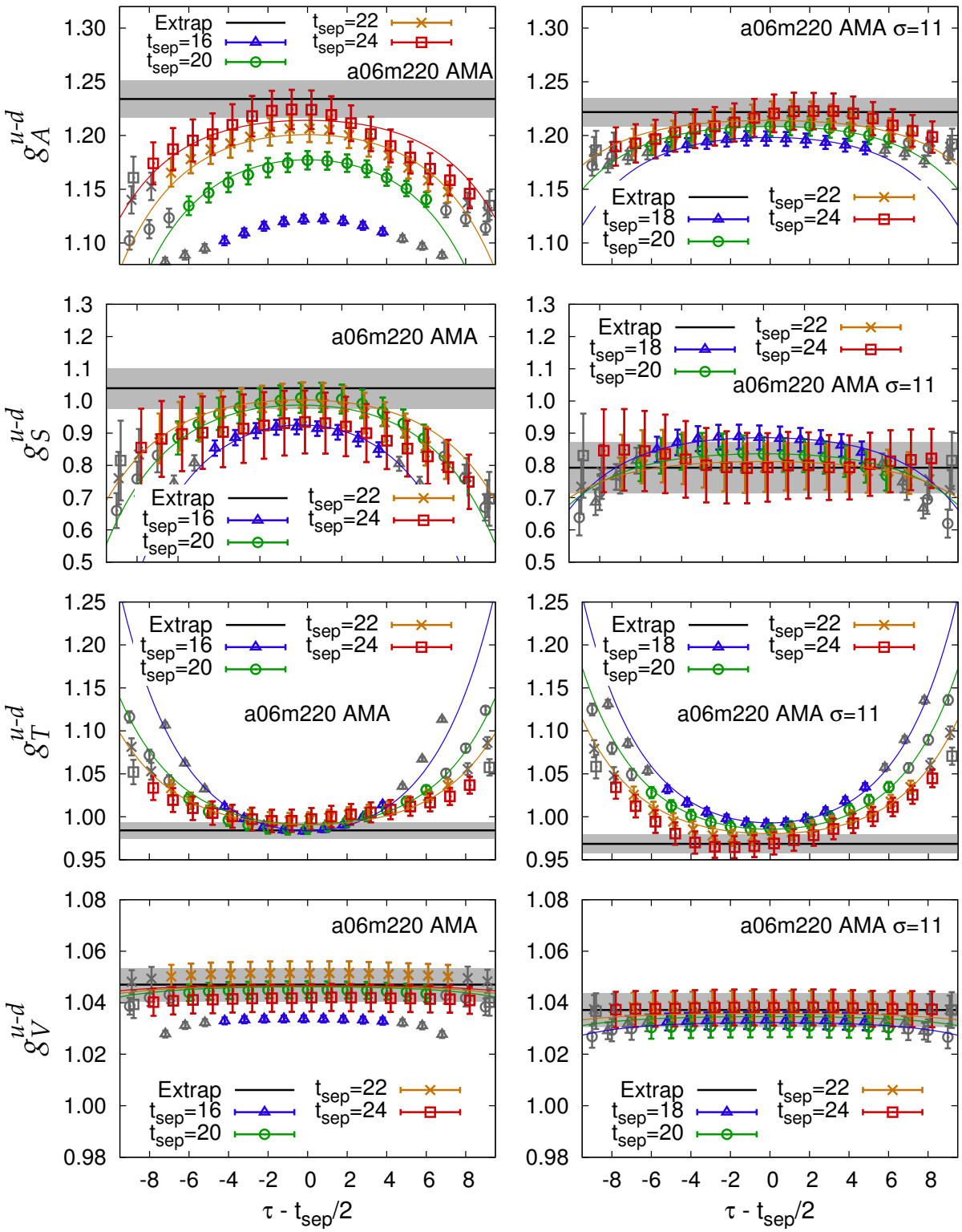

FIG. 23. Comparison of the excited-state contamination in the extraction of unrenormalized isovector charges $g^{u-d}_{A,S,T,V}$ from the $a06m220$ ensemble. The plots on the left are with smearing parameters $\{\sigma = 5.5, N_{\rm GS} = 70\}$ and on the right with $\{\sigma = 11, N_{\rm GS} = 230\}$. Both calculations were done using the AMA method with parameters summarized in Table XVIII.

state contamination within the quoted errors. (ii) The data for the renormalization constant in the RI-sMOM scheme show a window in q^2 over which the estimates in the $\overline{\rm MS}$ scheme at 2 GeV are constant within errors as discussed in Sec. IV and Ref. [11]. On the other hand, the poorly behaved 2-loop series for the matching factor suggests that this systematic uncertainty could be as large as 0.02. We have taken this systematic into account when estimating the error in Z_T given in Table X. (iii) The estimates from the nine ensembles display little dependence on the lattice spacing, pion mass or the lattice volume, as shown in Fig. 14. (iv) The largest change in estimates, about 0.04, is again due to adding a chiral logarithm term to the fit Ansatz.

Based on the data, fits and trends observed, we propose at an error budget from each of the sources that is summarized in Table XXI. The entries are constructed as follows: For the statistical uncertainty and excited-state contamination, we consider the data shown in Figs. 8, 9, 10, 22 and 23 and the errors in the 3-point function data, the efficacy of the 2-state fit and the difference between the two AMA estimates on the $a06m310$ and $a06m220$ ensembles. For estimating the uncertainty in the renormalization constants, we use the errors given in Table X, which are consistent with the size of the deviations of $Z_V g_V^{u-d}$ from unity given in Table XIII. For assessing the error associated with the extrapolation in the lattice spacing, we take half of the total spread in the central values at the three lattice spacings $a = 0.12$, 0.09 and 0.06 fm. Similarly, for the dependence on the quark mass, we take half of the spread in the central values at the three masses, $M_\pi \approx 135$, 220 and 310 MeV. The finite-volume correction is observed to be small in all cases and the error budget is assigned to be half the change on going from the 9-point to the 8-point fit estimates shown in Table XV, i.e., the direction is given by the change on removing the smallest $M_\pi L$ point $a12m220S$. Our combined fits include these systematics and the error estimates given in Tables XV are consistent with the error budget summarized in Table XXI.

An error estimate due to the choice of the fit Ansatz is the least straightforward to assess as discussed next. With nine data points, we can explore only a limited space of lowest order corrections given in Eqs. 11 and 12. Within this subspace, the largest variation with respect to the fit Ansatz is in g_S^{u-d} and g_T^{u-d} obtained with and without the chiral logarithm term as shown in Figs. 14 and 16 and quantified in Table XV. As pointed out in Sec. V, in fits with chiral logarithms, the two terms proportional to c_3 (or c_3') and $c_3^{\rm log}$ compete and the errors in them are large. The Akaike Information Criterion indicates that including the chiral logarithm term does not improve the fit sufficiently to warrent it. Nevertheless, we take half the spread (0.06 for g_S^{u-d} and 0.02 for g_T^{u-d}) between the two 9-point estimates given in Table XV as a conservative estimate of the uncertainty due to the fit Ansatz. Estimates of g_A^{u-d} are much more stable under changes in the fit Ansatz, with the central value varying between 1.18 and 1.21. Again, we take a conservative value, 0.02, as an estimate of this systematic uncertainty.

Error From	g_A^{u-d}	g_S^{u-d}	g_T^{u-d}
SESC	0.02 $\Uparrow$	0.05 $\Uparrow$	0.02 $\Downarrow$
Z	0.01 $\Downarrow$	0.04 $\Uparrow$	0.04 $\Downarrow$
a	0.02 $\Downarrow$	0.04 $\Uparrow$	0.01 $\Downarrow$
Chiral	0.02 $\Uparrow$	0.03 $\Downarrow$	0.02 $\Downarrow$
Finite volume	0.01 $\Uparrow$	0.01 $\Uparrow$	0.01 $\Uparrow$
Error quoted	0.033	0.12	0.046
Fit Ansatz	0.02	0.06	0.02

TABLE XXI. Estimates of the error budget for the three isovector charges due to each of the five systematic effects described in the text. The symbols $\Uparrow$ and $\Downarrow$ indicate the direction in which a given systematic is observed to drive the central value obtained from the 9-point fit. The second last row gives the errors in our best estimate given in Table XV using the 9-point fit. The last row gives the additional systematic uncertainty that accounts for the variations due to the choice of the fit Ansatz.

In Table XXI, we also indicate the direction in which our analysis changes the estimate as a result of taking into account a given systematic. For example, the slope of the fit to g_A^{u-d} versus a shown in Fig. 14 is positive. As a result, the central value after extrapolation to $a = 0$ is lower than the data points. We indicate this by attaching a $\Downarrow$ to the estimate shown in Table XXI. For the ratios of renormalization constants, we compare the estimates from method A and B given in Table IX. Taking estimates using method B as the baseline, we assign a $\Downarrow$ if taking the average with method A lowers the final estimate as shown in Table X. The direction of the SESC estimate is taken to be the direction of convergence with $t_{\rm sep}$.

Our final estimates for the isovector charges, including a second error to account for the variation in the estimates with the fit Ansatz, are given in Table XXII. Estimates of the flavor-diagonal charges given in Table XXIII and of g_T^{u+d} given in Table XXII are based on only the connected diagrams. We, therefore, consider it premature to assign an additional systematic uncertainty due to the fit Ansatz.

	g_A^{u-d}	g_S^{u-d}	g_T^{u-d}	$g_T^{u+d,{\rm con}}$
g_Γ	1.195(33)(20)	0.97(12)(6)	0.987(51)(20)	0.598(33)
χ^2/d.o.f.	0.28	0.67	0.44	0.30

TABLE XXII. Final estimates of the renormalized isovector charges for the proton from the 9-point fit described in Sec. V. The first error includes statistical and all systematic uncertainties except that due to the extrapolation Ansatz, which is given by the second error estimate. As explained in the text, in the connected estimate of g_T^{u+d} we only give the first error. Estimates for the neutron are obtained by $u \leftrightarrow d$ interchange.

To summarize, the first error quoted in g_T^{u-d} is dominated by that in Z_T and, as shown in Table XXI, all five systematic effects are in the same direction. Since the other four systematics are small, we are confident that our error estimate, 0.046, covers these five systematics. Our new result, $g_T^{u-d} = 0.987(51)(20)$, confirms the conclusion reached in Ref. [11] that all the systematics are under control at a few percent level in this calculation.

The extraction of the scalar charge $g_S^{u-d} = 0.97(12)(6)$ is less precise since the statistical errors in g_S^{u-d} on each ensemble are still 10–15%, that is, a factor of 3–5 larger than those in g_T^{u-d}. Also, all sources of systematic uncertainty are at the 5% level. The dominant systematic is from including a chiral logarithm in the fit Ansatz—the shift in the estimate is much larger than in g_A^{u-d} or g_T^{u-d}. Considering the size and sign of the first five systematic uncertainties, we again conclude that the first error, 0.12, and the additional 0.06 due to the fit Ansatz are conservative.

Our estimate $g_A^{u-d} = 1.195(33)(20)$ is smaller than the experimental result 1.276(3) by about 7%. This difference could be due to a combination of the observed few percent effect in the various systematics. Thus, a higher-statistics study on ensembles at smaller a and closer to the physical M_π is needed to improve the estimate.

VIII. COMPARISON WITH PREVIOUS WORKS

In this section we compare our results with previous determinations of the isovector charges g_A^{u-d}, g_S^{u-d} and g_T^{u-d}. In this comparison, it is important to note that we have, for the first time, taken all the systematics into account by uniformly using the 2-state fit with multiple values of $t_{\rm sep}$ to address excited-state contamination and by making a combined fit in the three variables a, M_π^2 and $M_\pi L$ using Eqs. 13 and 14. Our error estimates from this combined fit are larger (for example, the fits versus only M_π^2, shown in Fig. 14 as grey overlays, have a much narrower error band and give $g_A^{u-d} = 1.25(2)$); however, we claim they are realistic as discussed in Sec. VII. Also, our final results include a second error estimate: the first error includes statistical and all systematic uncertainties except that due to the extrapolation Ansatz, which is given by the second error estimate.

A. g_A^{u-d}

Calculations of g_A^{u-d} are considered a test of the lattice-QCD method to provide accurate estimates of the properties of the nucleon. A summary of experimental and lattice-QCD determination of g_A^{u-d} is given in Fig. 24. We note that over time the experimental estimate has increased steadily to its present value 1.276(3). On the other hand, most previous lattice-QCD estimates have been in the range 1.1–1.2 [19]. A significant reason for the lattice-QCD estimates being low has been excited-state contamination, since it can make a large negative contribution depending on the nucleon interpolating operator (the smearing parameter σ in our study) as shown in Figs. 8, 22 and 23. In this work, we have shown that analyses using a combination of well-tuned smeared sources for generating quark propagators, performing simulations at multiple values of $t_{\rm sep}$, and a simultaneous 2-state fit to the data at a number of values of $t_{\rm sep}$ reduces this contamination to the size of the statistical errors which are about 2%. With $O(50,000)$ measurements on ensembles with $M_\pi L \gtrsim 4$ and spanning 0.12–0.06 fm in lattice spacing and 135–320 MeV in the pion mass, the uncertainty from the chiral fit and continuum extrapolation is also reduced to about 2% from each of these systematics. Our analysis of the full error budget is presented in Sec. VII.

All but one previous lattice-QCD results underestimate g_A^{u-d} as shown in Fig. 24. The exceptional result is from the RQCD Collaboration [44] that finds a large slope with M_π^2 in the renormalization factor independent ratio g_A/F_π. Extrapolating this ratio to the physical pion mass gave the estimate $g_A = 1.280(44)(46)$ even though the majority of their data for g_A^{u-d} are $\lesssim 1.2$. Our data for F_π and g_A/F_π, given in Table XXIV, show little dependence on the lattice spacing and lattice volume. We, therefore, analyze them in Fig. 25 versus just M_π^2 and plot the result of a fit linear in M_π^2. The fit shows that our clover-on-HISQ estimate, $g_A/F_\pi = 12.88(15)$, at the physical pion mass remains low by about 7% compared to the experimental value 13.80. This is because our $F_\pi r_1$ data, where r_1 is used to set the scale of the HISQ lattices [22], extrapolate to the physical value. On the other hand, the error in the ratio g_A/F_π is much smaller than in g_A, therefore the deviation is more significant. The difference between the two calculations suggests that further analysis is needed to quantify the various systematics in g_A^{u-d}.

To reconcile the roughly 2σ difference between our result $g_A^{u-d} = 1.195(33)(20)$ and the experimental value $g_A^{u-d} = 1.276(3)$ would require all five $O(2\%)$ systematics given in Table XXI to eventually move the result in the same direction or one or more of the systematic effects have been grossly underestimated. To gain a better understanding of how the various sources of errors contribute and to reduce the overall uncertainty to $O(2\%)$ will require at least $O(200,000)$ measurements on the seven ensembles at different a and M_π used in this study and the analysis of one additional ensemble at $a = 0.06$ fm and $M_\pi = 135$ MeV. Increasing the statistics by a factor of four will reduce the errors in the data with the largest $t_{\rm sep}$ we have analyzed and thus improve the $t_{\rm sep} \to \infty$ estimates. Adding the point at the physical quark mass and the smallest lattice spacing $a = 0.06$ fm, will further constrain the chiral fit. This level of precision is achievable with the next generation of leadership-class computing resources.

	g_A^u	g_A^d	g_S^u	g_S^d	g_T^u	g_T^d
g_Γ	0.856(27)	−0.335(15)	4.94(30)	4.00(22)	0.792(42)	−0.194(14)
χ^2/d.o.f.	0.59	0.28	1.6	2.1	0.38	0.48

TABLE XXIII. Final estimates of the connected part of the renormalized flavor-diagonal charges of the proton. The χ^2/d.o.f. for the 9-point fit are given in the second row. Estimates for the neutron are obtained by the $u \leftrightarrow d$ interchange.

ID	$g_{A,\text{bare}}^{u-d}$	F_π^{bare} (MeV)	F_π (MeV)	g_A^{u-d}/F_π (GeV^{-1})
a12m310*	1.252(9)	107.7(1.0)	102.3(3.4)	11.62(14)
a12m220S	1.283(39)	102.4(1.0)	97.3(3.2)	12.53(40)
a12m220	1.273(30)	104.5(1.0)	99.2(3.2)	12.19(31)
a12m220L*	1.279(12)	104.2(0.9)	99.0(3.2)	12.27(15)
a09m310	1.262(30)	106.9(1.0)	101.6(3.3)	11.80(30)
a09m220	1.272(30)	102.8(0.9)	97.6(3.2)	12.38(31)
a09m130*	1.255(24)	97.2(0.8)	92.4(3.0)	12.91(26)
a06m310*	1.212(14)	107.7(0.7)	104.5(3.3)	11.25(15)
a06m220*	1.234(17)	101.3(0.7)	98.2(3.1)	12.19(19)

TABLE XXIV. Estimates of the unrenormalized g_A^{u-d} (reproduced from Table XI) and the bare and renormalized F_π obtained from the HP measurements. The dominant source of error in the renormalized F_π is the uncertainty in the Z_A given in Table X. We also give the renormalization factor independent ratio g_A^{u-d}/F_π, calculated as a ratio of the bare quantities, and which is plotted in Fig. 25.

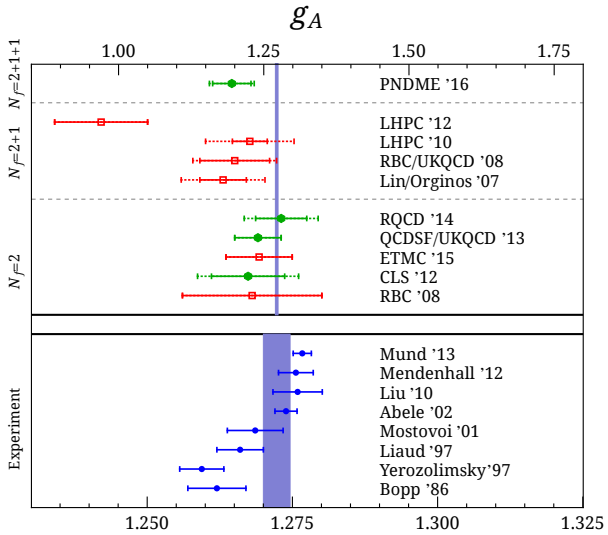

FIG. 24. (Top) A summary plot showing the current estimates of g_A^{u-d} from lattice-QCD calculations with 2+1+1, 2+1 and 2 flavors. The data are taken from: PNDME'16 (this work); LHPC'12 [45]; LHPC'10 [30]; RBC/UKQCD'08 [46]; RQCD'14 [44]; QCDSF/UKQCD'13 [47]; ETMC'15 [48]; CLS'12 [49]; RBC'08 [50]. (Bottom) The experimental result have been taken from: Mund'13 [2]; Mendenhall'12 [1]; Liu'10 [51]; Abele'02 [52]; Mostovoi'01 [53]; Liaud'97 [54]; Yerozolimsky'97 [55]; Bopp'86 [56]. The blue band highlights the 2014 PDG average value 1.2723(23) [5]. Note the change in scale between the upper (lattice QCD) and the lower (experimental) panels. The lattice-QCD estimates in red indicate that estimates of excited-state contamination, or discretization errors, or chiral extrapolation were not presented. When available, systematic errors have been added to statistical ones as outer error bars marked with dashed lines.

B. g_S^{u-d}

There are few estimates of g_S^{u-d} using lattice QCD. The RQCD Collaboration reported 1.02(18)(30) [44], and the LHPC Collaboration obtained 1.08(28) [57].[3] While these estimates are consistent with our result $g_S^{u-d} = 0.97(12)(6)$, it is clear that the errors are still large in all lattice-QCD estimates. Our work suggests that increasing the measurements to $O(200,000)$ on all the ensembles (the same program needed to reduce the overall uncertainty in g_A^{u-d} to 2%) will also reduce the uncertainty in g_S^{u-d} to less than 10%.

Gonzalez-Alonso et al. [58] used the conserved vector current (CVC) relation $g_S/g_V = (M_N - M_P)^{\text{QCD}}/(m_d - m_u)^{\text{QCD}}$ to obtain g_S^{u-d}. In their analysis, the estimates of the two mass differences on the right-hand side were obtained using the global lattice-QCD data. Their result, $g_S^{u-d} = 1.02(8)(7)$, is consistent with our estimate discussed above and shown in Fig. 26. These two lattice-QCD estimates, using CVC versus our direct calculation of the charge, have very different systematic uncertainties, so their consistency is a non-trival check. We, therefore, consider our result, $g_S^{u-d} = 0.97(12)(6)$, from a direct calculation as having achieved the target accuracy of about 10–15% needed to put bounds on scalar and tensor interactions at the TeV scale when combined with experimental measurements of b and b_ν parameters in neutron decay experiments with 10^{-3} sensitivity [7]. The current and prospective status of these bounds is given in Sec. IX.

We can use CVC in reverse to combine our result $g_S = 0.97(12)(6)$ with the lattice QCD determination of $(m_d - m_u)^{\text{QCD}}$ given by the Flavor Lattice Average Group (FLAG) [60] to predict $(M_N - M_P)^{\text{QCD}}$. Using the

[3] The recent estimates from the European Twisted Mass Collaboration (ETMC) [48] are not included in our comparison since they have not been extrapolated to the continuum limit. Their results are $g_S^{u-d} = 1.23(10)$ from the $2+1+1$-flavor calculation at $M_\pi = 373$ MeV and $a = 0.083$ fm and 2.16(34) from their physical-mass 2-flavor calculation at $a = 0.093$ fm.

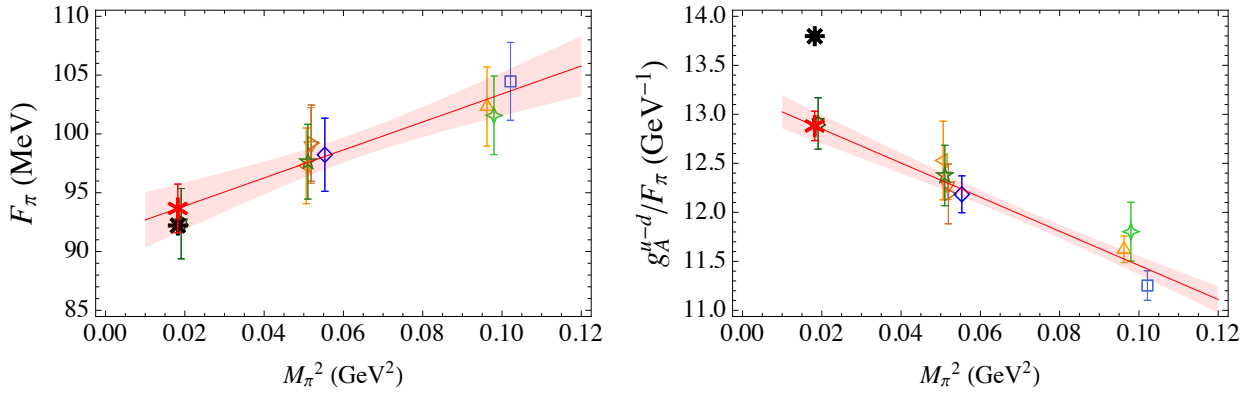

FIG. 25. Fits to F_π (left panel) and g_A/F_π (right panel) data given in Table XXIV assuming a linear dependence on M_π^2 for both. The lattice scale of these HISQ ensembles used to convert M_π and F_π to physical units was determined using r_1 [22]. Since the extrapolated F_π, red star, matches the experimental value at the physical point, the value of the renormalization factor independent ratio g_A/F_π remains about 7% below the experimental result shown as a black star.

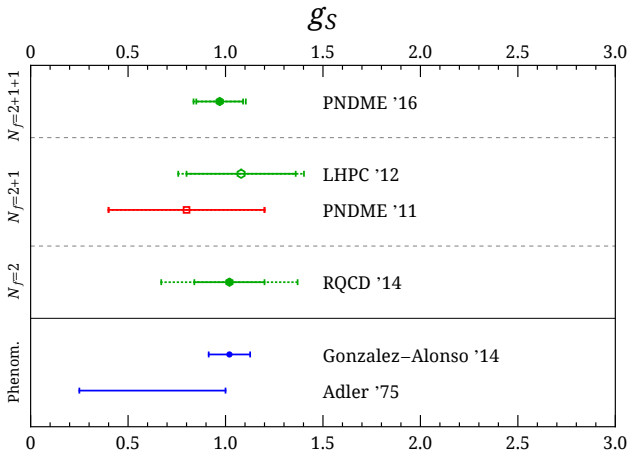

FIG. 26. A summary plot showing estimates for g_S^{u-d} from lattice QCD and phenomenology. The data are taken from: PNDME'16 (this work); LHPC'12 [57]; PNDME'11 [7]; RQCD'14 [44]. The estimates based on the conserved vector current and phenomenology are taken from: Gonzalez-Alonso [58] and Adler [59]. The rest is the same as in Fig. 24.

2+1-flavor estimates $m_d = 4.68(14)(7)$ MeV and $m_u = 2.16(9)(7)$ MeV from FLAG, we get $(M_N - M_P)^{\rm QCD} = 2.44(38)$ MeV, and using the 2+1+1-flavor FLAG estimates $m_d = 5.03(26)$ MeV and $m_u = 2.36(24)$ MeV gives $(M_N - M_P)^{\rm QCD} = 2.59(49)$ MeV. These two estimates update our old "PNDME" value quoted by Gonzalez-Alonso et al. [58] and are now competitive with other lattice QCD estimates given by them.

C. g_T^{u-d}

In Ref. [11], we presented a detailed discussion of all the errors in the determination of the isovector charge g_T^{u-d} and compared our results with those obtained by other collaborations. Our new estimate, $g_T^{u-d} = 0.987(51)(20)$, improves on the value 1.020(76) reported in Ref. [11].[4] It is also consistent with the estimate $g_T^{u-d} = 1.038(11)(12)$ from the LHPC Collaboration ($N_f = 2+1$ HEX-smeared clover action, domain-wall action, and domain-wall-on-asqtad actions) [57], and $g_T^{u-d} = 1.005(17)(29)$ by the RQCD Collaboration ($N_f = 2$ $O(a)$-improved clover fermions) [44]. The conclusion reached in Ref. [11], that the error estimates from the various sources are estimated reliably, is validated by this higher-statistics study. In Fig. 27, we update the lattice-QCD results and show that they are more accurate than the sum-rule, Dyson-Schwinger, and phenomenological estimates (integral over the longitudinal momentum fraction of the experimentally measured quark transversity distributions). Given the consistency of the lattice-QCD estimates and our better understanding of the excited-state contamination and other systematic effects, we consider our error estimate to be conservative and $g_T^{u-d} = 0.987(51)(20)$ a reliable value to use in phenomenology.

IX. CONSTRAINING NEW PHYSICS USING PRECISION BETA DECAY MEASUREMENTS

Our improved results for the isovector tensor charges $g_S^{\rm u-d}$ and $g_T^{\rm u-d}$ enable more stringent tests of non-standard scalar and tensor charged-current interactions, parameterized by the dimensionless couplings $\epsilon_{S,T}$ [7, 69]:

$$\mathcal{L}_{\rm CC} = -\frac{G_F^{(0)} V_{ud}}{\sqrt{2}} \Big[\epsilon_S \; \bar{e}(1-\gamma_5)\nu_\ell \cdot \bar{u}d + \epsilon_T \; \bar{e}\sigma_{\mu\nu}(1-\gamma_5)\nu_\ell \cdot \bar{u}\sigma^{\mu\nu}(1-\gamma_5)d \Big] \, . \quad (16)$$

[4] The small decrease can be traced back to the better control over excited-state contamination in this study with the AMA method and thus better determination of the $t_{\rm sep} \to \infty$ value that converges from above.

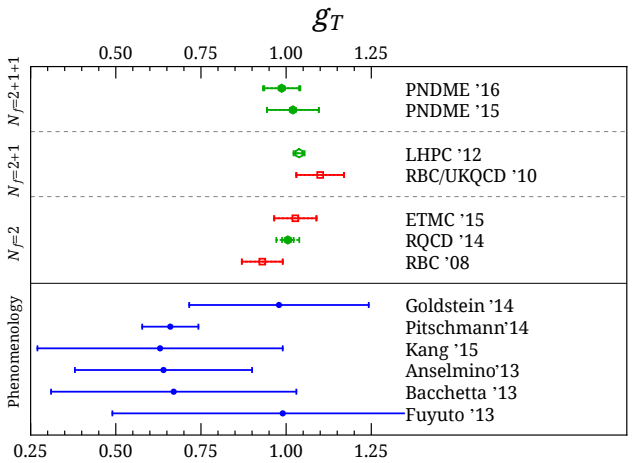

FIG. 27. A summary plot showing estimates for g_S^{u-d} from lattice QCD and phenomenology. The data are taken from: PNDME'16 (this work); PNDME'15 [11] LHPC'12 [57]; RBC/UKQCD'10 [61] ETMC'15 [48]; RQCD'14 [44]; and RBC'08 [50]. The phenomenological estimates are taken from: Kang'15 [62]; Goldstein'14 [63]; Pitschmann'14 [64]; Anselmino [65]; Bacchetta'13 [66]; and Fuyuto [67]. The rest is the same as in Fig. 24.

These non-standard couplings, $\epsilon_{S,T}$ can be constrained at low-energy by precision beta-decay measurements (of the pion, neutron, and nuclei) as well at the Large Hadron Collider (LHC) through the reaction $pp \to e\nu + X$. The LHC constraint is valid provided the mediator of the new interaction is heavier than a few TeV.

In Fig. 28 (left panel), we update the analysis of constraints on ϵ_T and ϵ_S presented in Refs. [7, 69] by using our improved estimate of the tensor charge and the LHC data from the 2012 run at $\sqrt{s} = 8$ TeV, for an integrated luminosity of approximately 20 fb^{-1} [70, 71]. The current bound on ϵ_T is dominated by the radiative pion decay $\pi \to e\nu\gamma$ [72, 73], while the bound on ϵ_S is dominated by the Fierz interference term in $0^+ \to 0^+$ nuclear beta decays [74].

In the prospective bounds shown in Fig. 28 (right panel), the change in low-energy constraints is due to improvements in experiments: We assume future measurements of the Fierz interference term and the neutrino asymmetry parameter (b and b_ν) in neutron decay will be at the level of 10^{-3} [8–10, 75]. A similar constraining power on ϵ_T can be achieved with a 0.1%-level measurement of the Fierz term in the pure Gamow-Teller ^{6}He decay [76].

Between the current and prospective constraints, the improvement in the LHC bounds come from both, the increase in center-of-mass energy $\sqrt{s}$ and the integrated luminosity. In both panels, the impact of using our estimates of $g_{S,T}$ given in Table XXII over the quark model estimates $0.25 < gS < 1.0$ and $0.6 < gT < 2.3$ [68] is large. Furthermore, the lattice-QCD reduction of uncertainties in $g_{S,T}$ implies that the constraining power of beta decays can actually be stronger than of the LHC for this class of non-standard interactions.

The current upper bounds on the effective couplings $\epsilon_{S,T} = (v/\Lambda_{S,T})^2$ correspond to lower bounds for the effective scales $\Lambda_S > 7$ TeV and $\Lambda_T > 13$ TeV. If future low-energy experiments find a nonzero signal, then combined with precision calculations of $g_{S,T}$, we will be able to predict the scale of new particles to be probed at the LHC or future colliders. Even without a signal, with improved precision, we will be able to tighten the lower bounds on the scale of new physics in these channels, which will help rule out certain classes of BSM models.

X. CONCLUSIONS

We have presented a high-statistics study of the isovector and flavor-diagonal charges of the nucleon using clover-on-HISQ lattice QCD. By using the AMA error-reduction technique we show that the statistical precision of the data can be improved significantly. Also, keeping one excited state in the analysis of data at multiple values of $t_{\rm sep}$ allows us to isolate and mitigate excited-state contamination. Together, these two improvements allow us to demonstrate that the excited-state contamination in the axial and the tensor channels has been reduced to the 2% level. The high-statistics analysis of nine ensembles covering the range 0.12–0.06 fm in the lattice spacing, $M_\pi = 135$–320 MeV in the pion mass, and $M_\pi L = 3.3$–5.5 in the lattice size allowed us to analyze the systematic errors due to lattice discretization, dependence on the quark mass and finite volume. As a result, this is the first work that is able to include the effect of these three systematic uncertainties by making a simultaneous fit in all the three variables a, M_π^2 and $M_\pi L$. In the case of the isovector charges, we also assign a second error estimate to account for the variation in the results due to the choice of the extrapolation Ansatz as discussed in Sec. VII. Our final estimates are given in Tables XXII and XXIII.

One of the largest sources of uncertainty comes from the calculation of the renormalization constants for the quark bilinear operators. These are calculated nonperturbatively in the RI-sMOM scheme over a range of values of q^2. As discussed in Sec. IV, the breaking of the rotational symmetry gives rise to a large spread in the data. After conversion to $\overline{\rm MS}$ scheme at 2 GeV using perturbation theory, which shows poor convergence for Z_T, the data, especially for g_S^{u-d}, do not show a large scaling window in which they are independent of q^2. Our estimates of errors take into account these uncertainties, and are therefore larger than those obtained by other collaborations.

Our estimate $g_A^{u-d} = 1.195(33)(20)$ is about 2σ (about 7%) below the experimental value $g_A/g_V = 1.276(3)$. In Sec. VII we analyze five systematic effects and find that each contributes at the 1–2% level, with roughly equal distribution in sign. Improvement in our understanding of these five systematic factors: residual excited-state

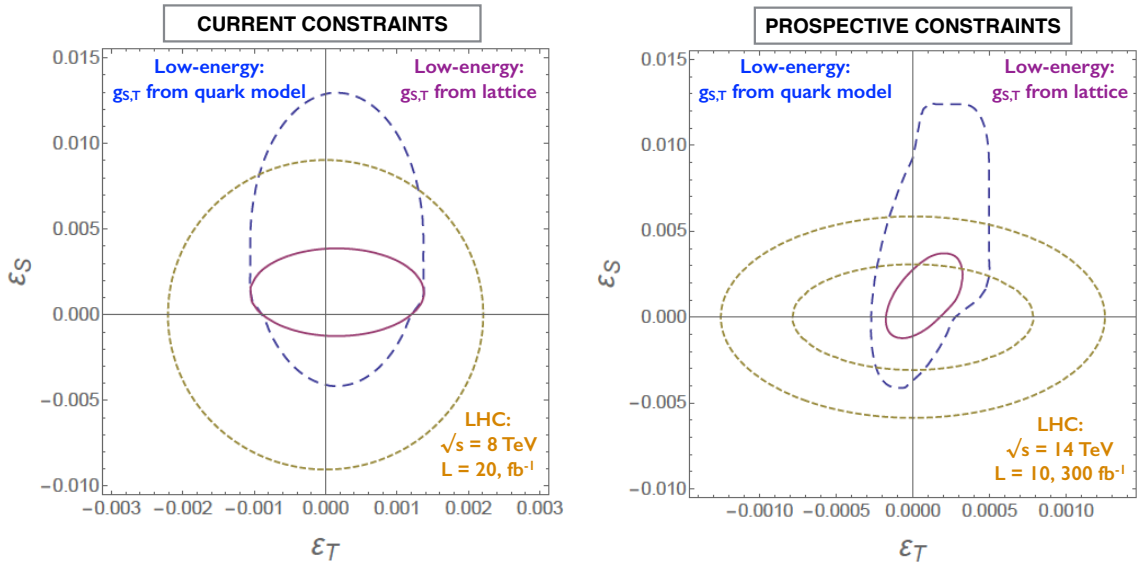

FIG. 28. Left panel: current 90% CL constraints on (ϵ_S) and (ϵ_T) from beta decays ($\pi \to e\nu\gamma$ and $0^+ \to 0^+$) and the LHC ($pp \to e\nu + X$) at $\sqrt{s} = 8$ TeV. Right panel: prospective 90% CL constraints on (ϵ_S) and (ϵ_T) from beta decays and the LHC ($pp \to e\nu + X$) at $\sqrt{s} = 14$ TeV. The low-energy constraints correspond to 0.1% measurements of B, b in neutron decay and b in ^{6}He decay. In both panels we present the low-energy constraints under two different scenarios for the scalar and tensor charges $g_{S,T}$: quark model [68] (large dashed contour) and lattice QCD results given in Table XXII (smaller solid contour).

contamination, uncertainty in the determination of the renormalization constants, the Ansatz used for the chiral fit, error in the chiral fit and the continuum extrapolation, requires a still higher-statistics calculation. Based on the various systematic errors discussed in Sec. VII, we claim in Sec. VIII A that the overall uncertainty can be reduced to 2% by increasing the statistics to $O(200,000)$ measurements on $O(2000)$ configurations on the seven ensembles shown in Fig. 8 and an additional physical mass HISQ ensemble at $a = 0.06$ fm. Lastly, to address possible systematic effects due to using the clover-on-HISQ formulation versus a unitary lattice formulation, we have started calculations with similar statistics and methodology using the clover-on-clover formulation [31].

For the tensor charges, we find that the dependence on the lattice volume, lattice spacing and the light-quark mass is small, and a simultaneous fit in these variables, keeping just the lowest-order corrections, gives reliable estimates of the physical value. Our final estimate for the isovector tensor charge, $g_T^{u-d} = 0.987(51)(20)$, is in good agreement with the previously reported estimate [11] and is more accurate than phenomenological estimates as shown in Fig. 27.

We have also updated our estimates for the connected parts of the flavor-diagonal charges. New estimates of the tensor charges of the proton, needed for the analysis of the contribution of the quark EDM to the neutron EDM [11, 20], are $g_T^u = 0.792(42)$ and $g_T^d = -0.194(14)$.

The extraction of the scalar charge of the proton has larger uncertainty. The statistical errors in the lattice data for $g_S^{u-d}(a, M_\pi, M_\pi L)$ are 3–5 times those in $g_T^{u-d}(a, M_\pi, M_\pi L)$, and the data show significant dependence on the lattice spacing a and a weaker dependence on the pion mass M_π. Our estimate, $g_S^{u-d} = 0.97(12)(6)$, is in very good agreement with the estimate $g_S^{u-d} = 1.02(8)(7)$ obtained using the conserved vector current relation in Ref. [58]. Previous lattice-QCD estimates summarized in Fig. 26 have larger errors but are consistent with these two estimates as discussed in Sec. VIII. Combining our estimate $g_S^{u-d} = 0.97(12)(6)$ with the 2+1+1-flavor estimate of the difference of light quarks masses $(m_d - m_u)^{\rm QCD} = 2.67(35)$ MeV given by the FLAG [60], we obtain $(M_N - M_P)^{\rm QCD} = 2.59(49)$ MeV

Finally, our results, $g_S^{u-d} = 0.97(12)(6)$ and $g_T^{u-d} = 0.987(51)(20)$, meet the target uncertainty of 15% required to maximize the impact of future measurements of the helicity-flip parts of the neutron decay distribution with 10^{-3} accuracy [7]. The status of current and prospective constraints on novel scalar and tensor interactions, $\epsilon_{S,T}$, using our improved estimates of $g_{S,T}$ are given in Sec. IX. Our goal for the near future is to further understand and reduce all the systematic uncertainties in the estimate of g_A^{u-d}, a benchmark for evaluating the accuracy achievable in lattice-QCD calculations of the matrix elements of quark bilinear operators within

nucleon states.

ACKNOWLEDGMENTS

We thank the MILC Collaboration for providing the 2+1+1-flavor HISQ lattices used in our calculations. We also thank Gunnar Bali, Jeremy Green and Martin Gonzalez-Alonso for discussions. Simulations were carried out on computer facilities of (i) the USQCD Collaboration, which are funded by the Office of Science of the U.S. Department of Energy, (ii) the Extreme Science and Engineering Discovery Environment (XSEDE), which is supported by National Science Foundation grant number ACI-1053575, (iii) the National Energy Research Scientific Computing Center, a DOE Office of Science User Facility supported by the Office of Science of the U.S. Department of Energy under Contract No. DE-AC02-05CH11231; and (iv) Institutional Computing at Los Alamos National Laboratory. The calculations used the Chroma software suite [26]. This material is based upon work supported by the U.S. Department of Energy, Office of Science of High Energy Physics under contract number DE-KA-1401020 and the LANL LDRD program. The work of HWL and SDC was supported by DOE grant No. DE-FG02-97ER4014. HWL is supported in part by the M. Hildred Blewett Fellowship of the American Physical Society. TB, VC, HWL and BY thank the Institute for Nuclear Theory at the University of Washington for its hospitality during the completion of this work.

[1] M. Mendenhall *et al.* (UCNA Collaboration), Phys.Rev. **C87**, 032501 (2013), arXiv:1210.7048 [nucl-ex].

[2] D. Mund, B. Maerkisch, M. Deissenroth, J. Krempel, M. Schumann, H. Abele, A. Petoukhov, and T. Soldner, Phys. Rev. Lett. **110**, 172502 (2013), arXiv:1204.0013 [hep-ex].

[3] M. Ademollo and R. Gatto, Phys.Rev.Lett. **13**, 264 (1964).

[4] J. F. Donoghue and D. Wyler, Phys.Lett. **B241**, 243 (1990).

[5] K. A. Olive *et al.* (Particle Data Group), Chin. Phys. **C38**, 090001 (2014).

[6] University of Guelph, Nuclear Physics Group, "Superallowed Beta Decay,".

[7] T. Bhattacharya, V. Cirigliano, S. D. Cohen, A. Filipuzzi, M. Gonzalez-Alonso, *et al.*, Phys.Rev. **D85**, 054512 (2012), arXiv:1110.6448 [hep-ph].

[8] R. Alarcon *et al.*, "Precise Measurement of Neutron Decay Parameters," (2007).

[9] W. Wilburn *et al.*, Rev. Mex. Fis. **Suppl. 55**, 119 (2009).

[10] D. Pocanic *et al.* (Nab Collaboration), Nucl.Instrum.Meth. **A611**, 211 (2009), arXiv:0810.0251 [nucl-ex].

[11] T. Bhattacharya, V. Cirigliano, S. Cohen, R. Gupta, A. Joseph, H.-W. Lin, and B. Yoon (PNDME), Phys. Rev. **D92**, 094511 (2015), arXiv:1506.06411 [hep-lat].

[12] G. S. Bali, S. Collins, and A. Schafer, Comput.Phys.Commun. **181**, 1570 (2010), arXiv:0910.3970 [hep-lat].

[13] T. Blum, T. Izubuchi, and E. Shintani, Phys.Rev. **D88**, 094503 (2013), arXiv:1208.4349 [hep-lat].

[14] M. Pospelov and A. Ritz, Annals Phys. **318**, 119 (2005), arXiv:hep-ph/0504231 [hep-ph].

[15] C. Baker, D. Doyle, P. Geltenbort, K. Green, M. van der Grinten, *et al.*, Phys.Rev.Lett. **97**, 131801 (2006), arXiv:hep-ex/0602020 [hep-ex].

[16] J. Dudek *et al.*, Eur. Phys. J. **A48**, 187 (2012), arXiv:1208.1244 [hep-ex].

[17] H.-W. Lin, PoS **LATTICE2012**, 013 (2012), arXiv:1212.6849 [hep-lat].

[18] S. Syritsyn, PoS **LATTICE2013**, 009 (2014), arXiv:1403.4686 [hep-lat].

[19] M. Constantinou, PoS **LATTICE2014**, 001 (2014), arXiv:1411.0078 [hep-lat].

[20] T. Bhattacharya, V. Cirigliano, R. Gupta, H.-W. Lin, and B. Yoon, Phys. Rev. Lett. **115**, 212002 (2015), arXiv:1506.04196 [hep-lat].

[21] E. Follana *et al.* (HPQCD Collaboration, UKQCD Collaboration), Phys.Rev. **D75**, 054502 (2007), arXiv:hep-lat/0610092 [hep-lat].

[22] A. Bazavov *et al.* (MILC Collaboration), Phys.Rev. **D87**, 054505 (2013), arXiv:1212.4768 [hep-lat].

[23] R. Gupta, T. Bhattacharya, V. Cirigliano, H.-W. Lin, and B. Yoon, *Proceedings, 33rd International Symposium on Lattice Field Theory (Lattice 2015)*, PoS **Lattice2015**, 130 (2015), arXiv:1601.01730 [hep-lat].

[24] B. Sheikholeslami and R. Wohlert, Nucl. Phys. **B259**, 572 (1985).

[25] A. Hasenfratz and F. Knechtli, Phys.Rev. **D64**, 034504 (2001), arXiv:hep-lat/0103029 [hep-lat].

[26] R. G. Edwards and B. Joo (SciDAC Collaboration, LHPC Collaboration, UKQCD Collaboration), Nucl.Phys.Proc.Suppl. **140**, 832 (2005), arXiv:hep-lat/0409003 [hep-lat].

[27] M. Gockeler, R. Horsley, E.-M. Ilgenfritz, H. Perlt, P. E. L. Rakow, G. Schierholz, and A. Schiller, Phys. Rev. **D53**, 2317 (1996), arXiv:hep-lat/9508004 [hep-lat].

[28] R. Babich, J. Brannick, R. Brower, M. Clark, T. Manteuffel, *et al.*, Phys.Rev.Lett. **105**, 201602 (2010), arXiv:1005.3043 [hep-lat].

[29] J. Osborn, R. Babich, J. Brannick, R. Brower, M. Clark, *et al.*, PoS **LATTICE2010**, 037 (2010), arXiv:1011.2775 [hep-lat].

[30] J. Bratt *et al.* (LHPC Collaboration), Phys.Rev. **D82**, 094502 (2010), arXiv:1001.3620 [hep-lat].

[31] B. Yoon *et al.*, Phys. Rev. **D93**, 114506 (2016), arXiv:1602.07737 [hep-lat].

[32] G. Martinelli, C. Pittori, C. T. Sachrajda, M. Testa, and A. Vladikas, Nucl.Phys. **B445**, 81 (1995), arXiv:hep-lat/9411010 [hep-lat].

[33] C. Sturm, Y. Aoki, N. Christ, T. Izubuchi, C. Sachrajda, *et al.*, Phys.Rev. **D80**, 014501 (2009), arXiv:0901.2599 [hep-ph].

[34] J. A. Gracey, Eur. Phys. J. **C71**, 1567 (2011), arXiv:1101.5266 [hep-ph].

[35] J. Gracey, Phys.Lett. **B488**, 175 (2000), arXiv:hep-ph/0007171 [hep-ph].

[36] V. Bernard, N. Kaiser, J. Kambor, and U. G. Meissner, Nucl. Phys. **B388**, 315 (1992).

[37] V. Bernard and U.-G. Meissner, Ann. Rev. Nucl. Part. Sci. **57**, 33 (2007), arXiv:hep-ph/0611231 [hep-ph].

[38] V. Bernard and U.-G. Meissner, Phys. Lett. **B639**, 278 (2006), arXiv:hep-lat/0605010 [hep-lat].

[39] A. A. Khan, M. Gockeler, P. Hagler, T. Hemmert, R. Horsley, *et al.*, Phys.Rev. **D74**, 094508 (2006), arXiv:hep-lat/0603028 [hep-lat].

[40] G. Colangelo, A. Fuhrer, and S. Lanz, Phys. Rev. **D82**, 034506 (2010), arXiv:1005.1485 [hep-lat].

[41] J. de Vries, R. Timmermans, E. Mereghetti, and U. van Kolck, Phys.Lett. **B695**, 268 (2011), arXiv:1006.2304 [hep-ph].

[42] V. Bernard, N. Kaiser, and U.-G. Meissner, Int. J. Mod. Phys. **E4**, 193 (1995), arXiv:hep-ph/9501384 [hep-ph].

[43] H. Akaike, IEEE Transactions on Automatic Control **19**, 716 (1974).

[44] G. S. Bali, S. Collins, B. Glssle, M. Gckeler, J. Najjar, *et al.*, Phys.Rev. **D91**, 054501 (2015), arXiv:1412.7336 [hep-lat].

[45] J. R. Green, M. Engelhardt, S. Krieg, J. W. Negele, A. V. Pochinsky, and S. N. Syritsyn, Phys. Lett. **B734**, 290 (2014), arXiv:1209.1687 [hep-lat].

[46] H.-W. Lin and K. Orginos, Phys.Rev. **D79**, 034507 (2009), arXiv:0712.1214 [hep-lat].

[47] R. Horsley, Y. Nakamura, A. Nobile, P. Rakow, G. Schierholz, *et al.*, Phys.Lett. **B732**, 41 (2014), arXiv:1302.2233 [hep-lat].

[48] A. Abdel-Rehim *et al.*, Phys. Rev. **D92**, 114513 (2015), [Erratum: Phys. Rev.D93,no.3,039904(2016)], arXiv:1507.04936 [hep-lat].

[49] S. Capitani, M. Della Morte, G. von Hippel, B. Jager, A. Juttner, *et al.*, Phys.Rev. **D86**, 074502 (2012), arXiv:1205.0180 [hep-lat].

[50] T. Yamazaki *et al.* (RBC+UKQCD Collaboration), Phys.Rev.Lett. **100**, 171602 (2008), arXiv:0801.4016 [hep-lat].

[51] J. Liu *et al.* (UCNA), Phys. Rev. Lett. **105**, 181803 (2010), arXiv:1007.3790 [nucl-ex].

[52] H. Abele, M. Astruc Hoffmann, S. Baessler, D. Dubbers, F. Gluck, U. Muller, V. Nesvizhevsky, J. Reich, and O. Zimmer, Phys. Rev. Lett. **88**, 211801 (2002), arXiv:hep-ex/0206058 [hep-ex].

[53] Yu. A. Mostovoi *et al.*, Phys. Atom. Nucl. **64**, 1955 (2001), [Yad. Fiz.64,2040(2001)].

[54] P. Liaud, K. Schreckenbach, R. Kossakowski, H. Nastoll, A. Bussiere, J. P. Guillaud, and L. Beck, Nucl. Phys. **A612**, 53 (1997).

[55] B. Erozolimsky, I. Kuznetsov, I. Stepanenko, and Yu. A. Mostovoi, Phys. Lett. **B412**, 240 (1997).

[56] P. Bopp, D. Dubbers, L. Hornig, E. Klemt, J. Last, H. Schutze, S. J. Freedman, and O. Scharpf, Phys. Rev. Lett. **56**, 919 (1986), [Erratum: Phys. Rev. Lett.57,1192(1986)].

[57] J. Green, J. Negele, A. Pochinsky, S. Syritsyn, M. Engelhardt, *et al.*, Phys.Rev. **D86**, 114509 (2012), arXiv:1206.4527 [hep-lat].

[58] M. Gonzlez-Alonso and J. Martin Camalich, Phys. Rev. Lett. **112**, 042501 (2014), arXiv:1309.4434 [hep-ph].

[59] S. L. Adler, E. W. Colglazier, Jr., J. B. Healy, I. Karliner, J. Lieberman, Y. J. Ng, and H.-S. Tsao, Phys. Rev. **D11**, 3309 (1975).

[60] The Flavor Lattice Averaging Group (FLAG), (2016).

[61] Y. Aoki, T. Blum, H.-W. Lin, S. Ohta, S. Sasaki, *et al.*, Phys.Rev. **D82**, 014501 (2010), arXiv:1003.3387 [hep-lat].

[62] Z.-B. Kang, A. Prokudin, P. Sun, and F. Yuan, (2015), arXiv:1505.05589 [hep-ph].

[63] G. R. Goldstein, J. O. G. Hernandez, and S. Liuti, (2014), arXiv:1401.0438 [hep-ph].

[64] M. Pitschmann, C.-Y. Seng, C. D. Roberts, and S. M. Schmidt, Phys.Rev. **D91**, 074004 (2015), arXiv:1411.2052 [nucl-th].

[65] M. Anselmino, M. Boglione, U. D'Alesio, S. Melis, F. Murgia, *et al.*, Phys.Rev. **D87**, 094019 (2013), arXiv:1303.3822 [hep-ph].

[66] A. Bacchetta, A. Courtoy, and M. Radici, JHEP **1303**, 119 (2013), arXiv:1212.3568.

[67] K. Fuyuto, J. Hisano, N. Nagata, and K. Tsumura, JHEP **1312**, 010 (2013), arXiv:1308.6493 [hep-ph].

[68] P. Herczeg, Prog. Part. Nucl. Phys. **46**, 413 (2001).

[69] V. Cirigliano, M. Gonzalez-Alonso, and M. L. Graesser, JHEP **02**, 046 (2013), arXiv:1210.4553 [hep-ph].

[70] V. Khachatryan *et al.* (CMS), Phys. Rev. **D91**, 092005 (2015), arXiv:1408.2745 [hep-ex].

[71] G. Aad *et al.* (ATLAS), JHEP **09**, 037 (2014), arXiv:1407.7494 [hep-ex].

[72] M. Bychkov, D. Pocanic, B. VanDevender, V. Baranov, W. H. Bertl, *et al.*, Phys.Rev.Lett. **103**, 051802 (2009), arXiv:0804.1815 [hep-ex].

[73] V. Mateu and J. Portoles, Eur.Phys.J. **C52**, 325 (2007), arXiv:0706.1039 [hep-ph].

[74] J. Hardy and I. Towner, Phys.Rev. **C79**, 055502 (2009), arXiv:0812.1202 [nucl-ex].

[75] D. Dubbers, H. Abele, S. Baessler, B. Maerkisch, M. Schumann, *et al.*, Nucl.Instrum.Meth. **A596**, 238 (2008), arXiv:0709.4440 [nucl-ex].

[76] A. Knecht *et al.*, *Proceedings, 11th Conference on the Intersections of Particle and Nuclear Physics (CIPANP 2012)*, AIP Conf. Proc. **1560**, 636 (2013), arXiv:1208.6433 [nucl-ex].